The Optimization of Data Acquisition, Fuel Flow, and Spark Timing Control for a Synthesis Gas-Engine-Generator System

By

Khalaf Saad AlZeeby

Submitted to the graduate degree program in the Department of Mechanical Engineering and the Graduate Faculty of the University of Kansas in partial fulfillment of the requirements for the degree of Master of Science.

_____

Chair: Dr. Christopher Depcik

_____

Dr. Ronald Dougherty

_____

Dr. Susan Williams

Defended: February 12th, 2018

The Thesis Committee for Khalaf AlZeeby certifies that this is the approved version of the following thesis:

The Optimization of Data Acquisition, Fuel Flow, and Spark Timing Control for a Synthesis Gas-Engine-Generator System

_____

Chair: Dr. Christopher Depcik

Date Approved: April 9th, 2018

Abstract

As climate change drives the exploration into new and alternative fuels, biodiesel has emerged as a promising alternative to traditional diesel fuel. To further increase the viability of biodiesel, a unique system at the University of Kansas utilizes glycerin, the primary byproduct of biodiesel production, for power generation. This system converts glycerin into a hydrogen-rich gas (syngas) that is sent to an engine-generator system in one continuous flow process. This thesis details the implementation and troubleshooting of recent upgrades to the system, the experimental optimization of propane fuel and spark control for the engine, and directions for future research involving this setup.

Chapter Two describes recent changes in the Syngas Rig including the renovation and replacement of various components to enhance the efficiency of the system and to resolve encountered issues. For instance, a recently installed water pump (Berkeley Model S39533) in the cooling system replaced the stock mechanical pump to eliminate an engine overheating issue. Moreover, additional safety measures were implemented in the fuel system in order to prevent any unintentional activation of fuel flow. All of the rig's operating paths now require the activation of both mechanical and electric switches by wiring in a series instead of through parallel circuits. This chapter also includes troubleshooting guidelines to aid future students in utilizing the system.

The third chapter discusses upgrades in pure propane operation that help by preheating the engine prior to syngas operation and establishing the baseline energy requirement for fueling the system. In addition, an upgrade to the fuel system incorporates an electric fuel valve (EFV) as a replacement for a gaseous propane carburetor, providing the ability for air-to-fuel ratio (AFR) adjustment of the engine at different generator loads. Moreover, spark timing optimization accompanies the new fuel control in order to enhance engine performance and maximize fuel economy. Additionally, in-cylinder pressure traces and associated performance parameters are reviewed and discussed in order to analyze the operation of the new EFV-based system. Finally, the fourth chapter provides a thorough discussion of the thesis efforts along with suggested directions for future research.

Acknowledgements

The successful completion of this research, including this thesis, were attained primarily due to the support and inputs provided by Dr. Depcik. Moreover, the assistance and experience of previous and current graduate students were important factors in the advancement of this effort. Indeed, this research is an extension to a wide range of previous effort, support, and donations. For instance, the Hill Engineering Research and Development Center was designed and built by Studio 804, a graduate research program for architecture students at KU. Additionally, Dr. Geng Ku provided counseling regarding the technical analysis needed for the signals and DAQ systems. Moreover, the utilizations of the ECU in the Syngas-Rig made possible by the technical support provided by Mr. Bob R of DynamicEFI, the aftermarket ECU Company. Last but not least, to my family and friends: Thank you for your unconditional love and support throughout the lengthy years of research.

Table of Contents

Table of Figures

Table of Tables

Nomenclature

Abbreviation	Description
A/D	Analog-to-Digital
A/F	Air-Fuel
AA	Assured Automation
ACI	Analog Current Input
ADC	Analog-to-Digital Converter
AFR	Air-to-Fuel Ratio
AI	Analog Input Channels
AO	Analog Output Channels
°ATDC	After Top Dead Center
AVI	Analog Voltage Input
AVO	Analog Voltage Output
BPV	Back-Pressure Valve
BS2	Basic Stamp 2
°BTDC	Before Top Dead Center
CA	Crank Angle
CAM	Crank Angle Marks
CCW	Counterclockwise
CEA	Chemical and Equilibrium with Application
CI	Compression Ignition
CID	Cubic Inch Displacement
CNG	Compressed Natural Gas
CO	Carbon Monoxide
CTS	Coolant Temperature Sensor
CW	Clockwise
DAQ	Data Acquisition
DC	Direct Current
DIO	Digital Input-Output
DIP	Dual In-Line Package
DMA	Direct Memory Access
EBL	Embedded Lockers
ECM	Engine Control Module
ECU	Engine Control Unit
EFV	Electric Fuel Valve

EGR	Exhaust Gas Recirculation
EPA	Environmental Protection Agency
ESC	Electronic Spark Control
EVO	Exhaust Valve Open
FCV	Fuel Control Valve
FIFO	First-In-First-Out
FPGA	Field-Programmable Gate Array
FSS	Flat Sequence Structure
GM	General Motors
GUI	Graphical User Interface
HC	Hydrocarbons
HEI	High Energy Ignition
HERDC	Hill Engineering Research and Development Center
HEX	Heat Exchanger
I/O	Input/Output
IC	Internal Combustion
ICP	In-Cylinder Pressure
ICP-DAQ	In-Cylinder Pressure Data Acquisition
IMEP	Indicated Mean Effective Pressure
IVC	Inlet Valve Close
KU	University of Kansas
lb.	Pound (mass)
LED	Light-Emitting Diode
LFE	Laminar Flow Element
LPG	Liquefied Petroleum Gas
LPP	Location of Peak Pressure
MAP	Manifold Absolute Pressure
MBT	Maximum Brake Torque
NASA	National Aeronautics and Space Administration
NI	National Instruments
NO_x	Nitrogen Oxides
PC	Personal Computer
PCIe	Peripheral Component Interconnect Express
PFI	Port-Fuel-Injection
PM	Particulate Matter
PP	Pure Propane

PT	Pressure Transducer
PWM	Pulse-Width Modulation
RFS	Renewable Fuel Standards
RG	Reformed Glycerin
RIO	Reconfigurable Input/Output
RP	Reformed Glycerin
RPM	Revolutions Per Minute
SA	Spark Advance
SAE	Society of Automotive Engineers
SBC	Small Block Chevy
SI	Spark Ignition
SPDT	Single-Pole-Double-Throw
TC	Thermocouple
TDC	Top Dead Center
TDC-1	Top Dead Center of the First Cylinder
TDC-3	Top Dead Center of the Third Cylinder
TRG	Top Dead Center Trigger
TTL	Transistor–Transistor Logic
TV	Throttle Valve
US	United States
USB	Universal Serial Bus
VCS	Vacuum Control Solenoid
VFF	Vacuum Fuelock Filter
VI	Virtual Instruments
XOR	Exclusive “Or” – Boolean logic gate that outputs a true value when the two inputs are opposite (i.e. True-False or False-True)

Variable	Description	Units
a	Crank Radius	(m^3)
ADC Resolution	The total number of bits used to represent the analog voltage signal.	16-bit per V_{DC}
$(A/F)_{actual}$	Measured Air-Fuel Ratio	(-)
$(A/F)_{stoich}$	Stoichiometric Air-Fuel Ratio	(-)
Amplifier Scale	The hardware (Kistler Amplifier) configurable gain value	bar per V_{DC}
b	Cylinder Bore	(m^3)
CA° Array	An array of Crank Angles at which the pressure are measured.	°
CA Window	The range of sampled Crank Angle in a single engine cycle	(720 °CA/cycle)
CAM Resolution	The pressure sampling frequency, dictated by the CAM resolution	0.5° per elements
Code Width	The smallest analog voltage change that can be detected	V_{DC} per bit
DMA Acquire	The total number of raw elements acquired from the DMA buffer	elements
DMA Buffer	The size of an allocated memory block, used as a data buffer	elements
EVO	Exhaust Valve Opening time	(°ATDC)
$IMEP_g$	Gross Indicated Mean Effective Pressure	(bar)
$IMEP_n$	Net Indicated Mean Effective Pressure	(bar)
IVC	Intake Valve Closing time	(°BTDC)
l	Connecting Rod Length	(m^3)
$\dot{m}_f$	Fuel Flow Rate	(g/s)
N	Engine Rotational Speed	(RPM)
N_{Array}	The Array length, is the number of pressure data elements in a single cycle	1440 elements per cycle
N_{FPGA}	The total number of consecutive engine revolutions measured in a single FPGA VI execution.	122 revolutions
N_{Gross}	The number of pressure elements used for calculating the gross indicated parameters	elements per cycle
N_{Host}	The total number of engine cycles collected and processed in by the Host VI	21 or 61 cycles
n_R	Number of revolutions in a thermodynamic cycle, (2 for a four-stroke engine)	2 rev. per cycle
Pressure Conv. Factor	A unique cumulative value for converting the raw data to pressure values in units of bar	bar per bit

$SA_{Centrifugal}$	Centrifugal Spark Advance	(°BTDC)
$SA_{Distributor}$	Physical Base Initial *SA* Set by Physically Rotating the Distributor	(°BTDC)
SA_{ECM}	Spark Advance Bias Used by the ECM to Counterbalance the Physical *SA*	(°BTDC)
SA_{ECT}	Spark Timing Adjustments Based on Engine Coolant Temperature	(°BTDC)
SA_{IAT}	Spark Timing Adjustments Based on Intake Air Temperature	(°BTDC)
$SA_{Initial}$	Initial Spark Advance	(°BTDC)
SA_{Lookup}	Spark Timing Calculated by the ECM Using Lookup Tables as a Function of Engine Conditions	(°BTDC)
SA_{Main}	Main *SA* Based on the Engine Speed (rpm) and Load (MAP)	(°BTDC)
$SA_{Mechanical}$	Mechanical Spark Advance	(°BTDC)
SA_{Total}	Total Spark Advance	(°BTDC)
SA_{Vacuum}	Vacuum Spark Advance	(°BTDC)
Sampling Window	The Crank Angle range where pressure is measured	720 °CA per cycle
Sorting Index	The number of elements at which the data sorting begins.	(-)
Trimming Factor	The fraction of the raw data that is trimmed from the first engine cycle (i.e., the buffer cycle)	(-)
$V(\theta)$	Instantaneous Cylinder Volume	(m^3)
V_C	Clearance Volume	(m^3)
V_d	Displacement Volume of the Engine	(m^3)
V_{DC}	Direct Current Voltage	(Volt)
V_{EVO}	Cylinder Volume at Exhaust Valve Opening	(m^3)
V_{IVC}	Cylinder Volume at Intake Valve Closing	(m^3)
Voltage Input Range	Configurable peak-to-peak voltage span that sink device can measure	V_{DC}
W_{ig}	Gross Indicated Work	(kJ/cycle)
W_{in}	Net Indicated Work	(kJ/cycle)
W_p	Pumping Work	(kJ/cycle)
$x(\theta)$	Distance between Crank Axis and Piston Pin Axis	(m^3)

$\eta_{t,in}$	Net Indicated Thermal Efficiency	(%)
θ	Crank Angle	(°)
λ	Engine Lambda	(-)

1.1 Introduction

Fluctuations in oil prices along with the dwindling of petroleum reserves have increased the attention on biodiesel as a feasible alternative fuel. Biodiesel, which can be made domestically using vegetable oils or other natural sources, provides many advantages over traditional fossil fuels [1]. Most notably, it reduces dependency on foreign oil while reducing harmful effects to the environment and can be used in existing compression ignition (CI) engines without alteration [2]. For these reasons, the demand for, and subsequent production of, biodiesel has increased dramatically in recent years. In specific, biodiesel production in the United States (US) jumped from 8.58 million gallons in 2001 to more than 1.3 billion gallons in 2013 with further increases projected largely in response to the Renewable Fuel Standards set by the Environmental Protection Agency (EPA) [3].

Along with the numerous benefits resulting from this growth in the biodiesel market, there are a few complications associated with recent trends. Namely, the accumulation of crude glycerin as a necessary byproduct of the biodiesel manufacturing process yielded at roughly 10% weight/weight biodiesel [4]. Glycerin is a relatively simple chemical compound commonly used for commercial purposes, but the increase in supply driven by the production of biodiesel has flooded the market for this commodity. In 1999, only 9% of glycerin came from biodiesel production; whereas by 2009, the biodiesel industry was responsible for 64% of the total glycerin produced [5]. In only one year, due to the increase in biofuel production in the US, from 75 to 250 million gallons for 2005 and 2006, glycerin production nearly tripled from 62 million to 213 million lbs. If current trends persist, it seems likely that the glycerin supply will soon exceed worldwide demand.

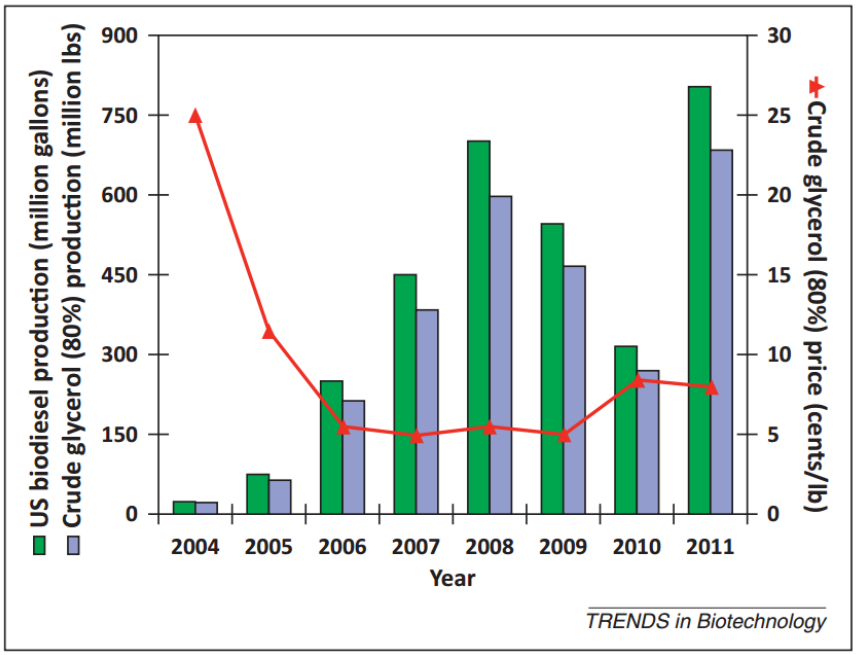

Figure 1: United States Biodiesel Production and Crude Glycerol Price [6].

As a result, crude glycerin's economic viability is a major concern to the biodiesel industry as an overabundance of glycerin can become a financial liability and logistics burden to producers [7]. Biodiesel suppliers must decide whether to sell, store, or dispose of this byproduct, with each option presenting its own complications. If sold, the value of glycerin can be used to help offset the costs of manufacturing biodiesel; hence, its price directly impacts the profitability of biodiesel production with a $0.01/lbs. drop in the value of glycerin correlating to a $0.08/lbs. rise in the cost of biodiesel production [8]. However, an increase in biodiesel production and its inevitable crude glycerol production by extension has already led to a decrease in the crude glycerol price from $0.25/lbs. in 2004 to less than $0.10/lbs. in 2011 as shown Figure 1.

The price of crude glycerin has dropped so low that biodiesel producers often store glycerin, waiting for a better market [9]. Moreover, some analysts assign a negative value to this commodity, as many producers must pay to have it transported [10]. Others simply dispose of the excess glycerin by dumping it in nearby water sources or through dispersing it over the land. All of these methods may be hazardous to the environment and accompanied by costly fines or damage [11]. Clearly, it is in the best interest of biodiesel producers to find a way to use this byproduct or to increase its demand in the market

to promote its profitable sale. The need for an acceptable solution to this dilemma, in consideration with the popularity of biodiesel fuels, has led to significant research in this area.

1.2 Background and Experimental Setup

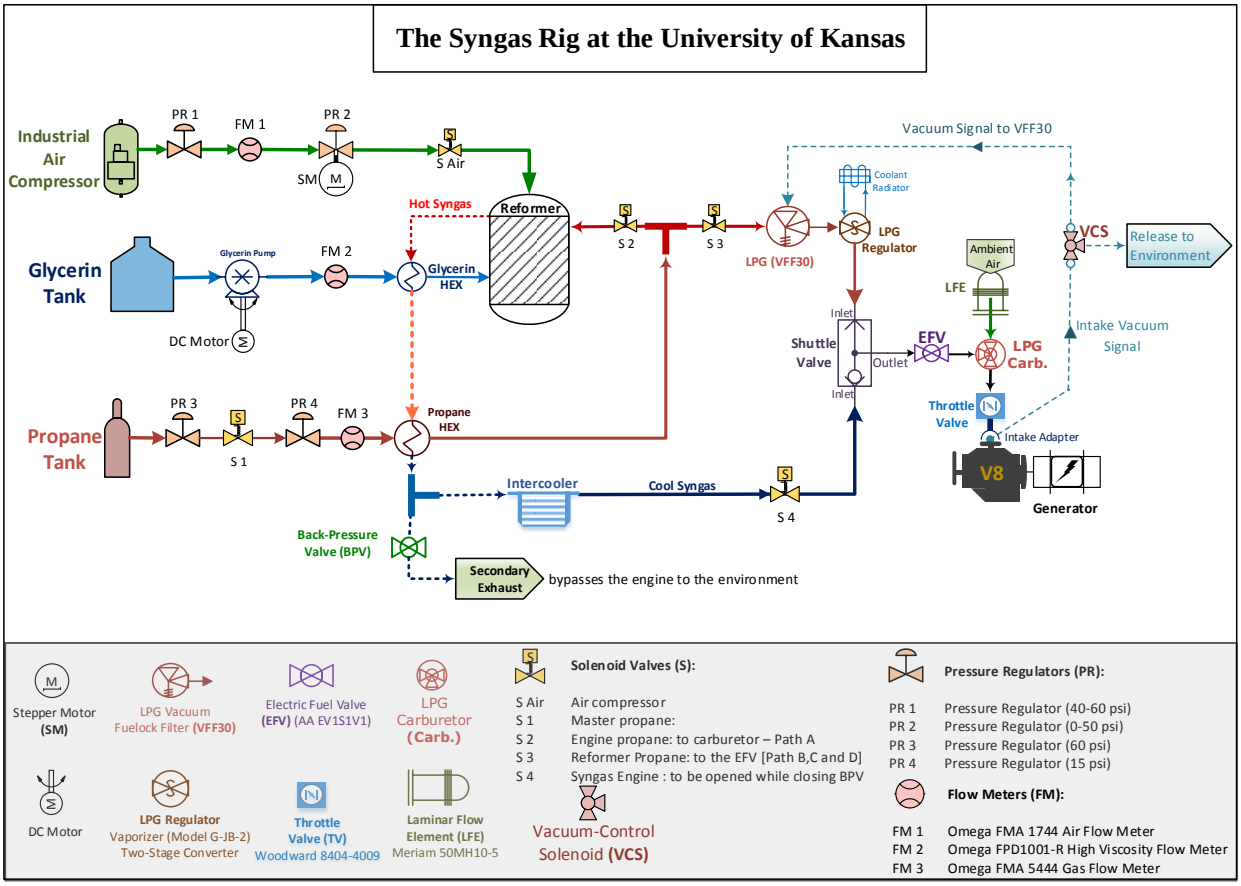

Figure 2: Flow Structure of Syngas Rig Components

In order to take advantage of biodiesel as an alternative fuel source while minimizing the challenges posed by the inevitable excess glycerin production, a unique system at the University of Kansas (KU) has been developed that converts glycerin into syngas (i.e., a synthesis hydrogen rich gas) that is utilized in an engine-generator setup to produce electric power. The main components of this system, hereafter referred to as the Syngas Rig, are a full-scale reformer, a small block Chevy (SBC) 350 cubic inch (CID) engine, and an electric generator as indicated in Figure 2. In addition to these components, data acquisition (DAQ) sensors and controllers are implemented to monitor and control the different equipment making up the Syngas Rig [12].

Typically, the direct usage of glycerin as a fuel in internal combustion (IC) engines is hindered by the negative behavior of glycerin in fuel lines, such as caking, settling, and solidifying [13]. Moreover, the difficulty of atomizing glycerin, due to its high density and viscosity, requires the preheating of glycerin prior to its combustion [14]. Therefore, partial oxidation is used as a catalytic method to convert the glycerin into a hydrogen rich fuel before combusting it in the engine. This process occurs in the first major component of the Syngas Rig through a reformer that consists of a stainless steel cylinder filled with nickel coated aluminum oxide catalytic spheres [15]. An 8-inch diameter outer shell packed with insulation surrounds the reformer. Additionally, the reformer is equipped with thermocouples to measure the flame temperature (next to the igniter), the catalyst temperature (buried in the catalyst spheres), and the heat loss from the surface using surface thermocouples along the length of the reformer's outer surface. Moreover, the reformer's input and output temperatures are monitored by thermocouples. Of note, the system can employ various different gaseous and liquid fuels, but for the purposes of this effort, propane was used to determine the energy balance of the engine and to preheat the reformer prior to the utilization of glycerin.

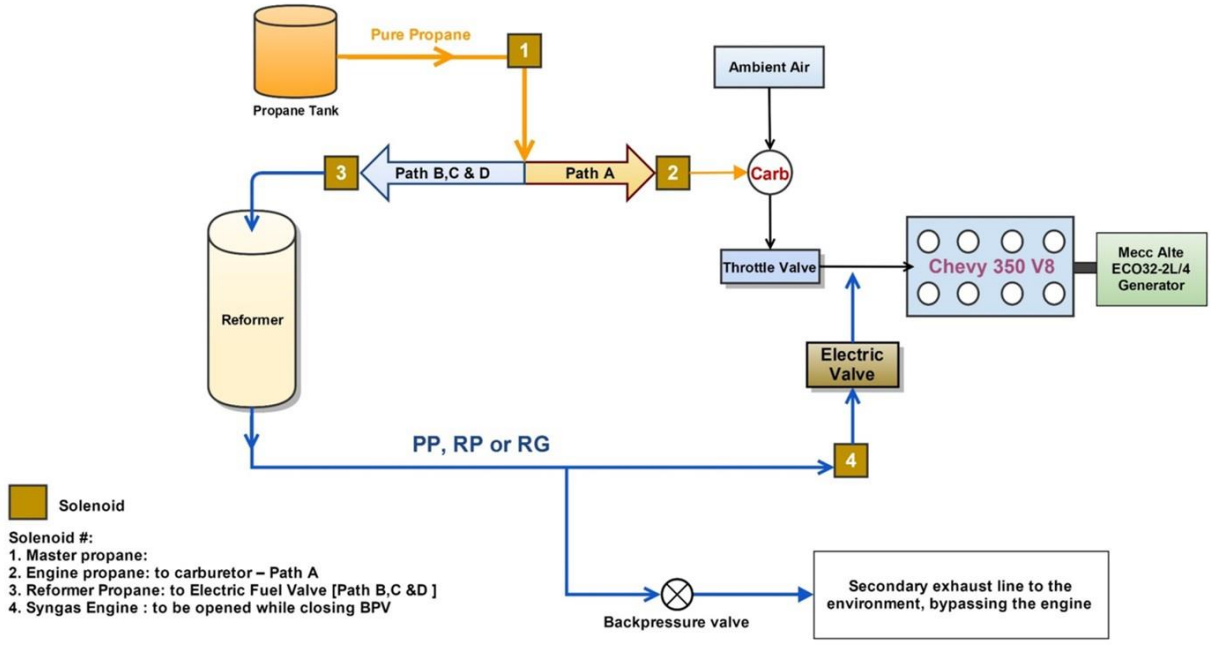

Figure 3: Possible Operation Pathways of the Syngas Rig

Partial combustion in the reformer is initiated by a Bosch spark plug, powered by a 9000-VDC neon transformer. Following the reformer, two heat exchangers are placed in-line to preheat the fuel entering the reformer (either glycerin or propane) and to cool the leaving syngas, which helps in reducing the potential of engine knock. The first heat exchanger has a gas-liquid spiral design that pre-heats the glycerin before entering the reformer during the glycerin reforming operation. The second heat exchanger is a SEC PL-500 shell-and-tube heat exchanger, which preheats the propane entering the reformer when employing propane reforming. Following the propane reformer, the activation of certain solenoids in a T-junction pipe system determines the fuel path depending on the operation to be conducted. For example, if one wishes to run the engine on pure propane, the activation of solenoid 1 and solenoid 2 directs the pure propane flow to a custom propane carburetor. Similarly, the activation of solenoid 1 and 3 directs the propane path to the reformer.

The next main component in the Syngas Rig is a naturally aspirated spark ignition (SI) SBC engine. Using a Woodward throttle valve (TV), the engine is currently set to operate at a speed of 1800 revolutions per minute (RPM) in order to match the required frequency of the generator. At the flywheel, the engine is coupled to a Mecc Alte ECO32-2L/4 generator. As an analogue to a dynamometer in an engine test cell, the generator can provide a load on the engine using two 240 VAC, 50 Amp power outlets. During experimental tests, two industrial space heaters were plugged into these power outlets in order to provide a load on the engine [16]. Figure 3 displays the overall setup of the Syngas Rig along with the various flow patterns made possible by its design structure.

In order to better optimize the glycerin reformation process, the system incorporates four different operating pathways. The first operating path is Path A, where pure propane (PP) runs the engine via a gaseous carburetor. This path is the most stable path; therefore, it is used for preheating the engine before running on syngas. Moreover, Path A is used as a reference for the engine's fuel requirement (i.e., the energy required to run the engine). The next path is a new conduit developed for this effort: Path B. Through this avenue, the engine also runs on PP but instead utilizes an electric fuel valve (EFV). This path serves the same purpose as Path A, but the EFV allows for finer control of the fuel flow rate (either

manually or automatically) in comparison to the carburetor when operating the engine at different loads as discussed in Chapter 2.

The syngas pathways also include either Path C and Path D. Path C involves reforming propane and running the engine on the produced syngas. Previous experiments determined the appropriate flow rates for this path by matching the engine's energy requirement from Path A with the simulation results of a reformer combustion model based on the NASA Chemical and Equilibrium with Application (CEA) program. Furthermore, while Path C results in the loss of available energy, it is a necessity because it preheats the catalyst in the reformer prior to segueing to the exothermic glycerin reformation process [15]. Lastly, via Path D, the reformation of glycerin occurs after stopping the flow of propane. In Figure 3, the four possible operation pathways are shown while also highlighting the necessary solenoids that need to be activated.

1.3 Thesis Effort

The second chapter of this thesis includes a description of the experimental setup and upgrades to the Syngas Rig at the University of Kansas. This includes the hardware and software upgrades to the controlling and monitoring devices, as well as Data Acquisition (DAQ) systems. The Primary DAQ system is equipped with sensors, flowmeters, controllers, and thermocouples that are used for controlling and monitoring the operation states. The Secondary DAQ system employs a high-speed in-cylinder pressure (ICP) system for monitoring and recording indicated performance parameters. Moving the Syngas Rig to a new building (i.e., the Hill Engineering) posed challenges regarding the configuration of the system. For instance, the previous setup in a barn placed the DAQ close by the Syngas Rig, which enabled running the wires between the sensors and the DAQ in close proximity, directly, and without inference caused by high frequencies coming from adjacent power cables or other high frequency sensors. Hence, some issues arose from the remote distance of the DAQ system in its new location and the computer that operated the in-cylinder pressure (ICP) system. Therefore, several troubleshooting steps were taken to identify the problems, and the second chapter includes a manual for troubleshooting the ICP system in terms of hardware, software, and signal waveform to be used in future operation of the rig.

The third chapter discusses upgrades in the pure propane (PP) operation of the Syngas Rig and the experimental optimization of engine performance (i.e., air-to-fuel ratio and spark timing). This operation pathway serves to preheat the engine prior to syngas operation and establish the baseline energy requirements for fueling the system. The current upgrade to the fuel system incorporates an electric fuel valve (EFV) as a replacement for a gaseous propane carburetor, providing the ability for air-to-fuel ratio (AFR) adjustment of the engine at different generator loads. The use of EFV in a continuous fuel additive manner provides a solution to the carburetor's inherent disadvantage: maintaining a constant AFR. Hence, this upgrade allows the system to adjust more accurately to different engine operating conditions and other unique fuels to be potentially tested (e.g., natural gas and biogas). Moreover, spark timing optimization accompanies the new fuel control in order to enhance engine performance and maximize fuel economy. Finally, in-cylinder pressure traces and associated performance parameters are reviewed and discussed in order to analyze the operation of the new EFV-based system.

Lastly, the fourth chapter summarizes the outcomes of this effort along with recommendations for future work involving the system. The developments and conclusions reached through all upgrades and experimental procedures are addressed with an emphasis on the progress achieved as a result of the efforts previously discussed. Furthermore, directions for future research are suggested in order to continue making improvements to the effective use of syngas in engine operation.

Chapter II: Syngas Rig Experimental Upgrades and Troubleshooting Guide

2.1 Introduction

Previous efforts at the University of Kansas resulted in a unique system that utilizes glycerin for power generation in an engine-generator setup employing partial oxidation as the catalysis method in the reformer [16]. The opening of the Hill Engineering Research and Development Center (HERDC) as a new facility provided the opportunity for upgrading the location and operation of the Syngas Rig [17]. Furthermore, recent changes in the Syngas Rig included the renovation and replacement of various components to enhance the efficiency of the system and resolve the encountered issues. For instance, a recently installed water pump (Berkeley Model S39533) in the cooling system replaced the stock mechanical pump to eliminate an engine overheating issue. For a stationary engine in a confined space, this new pump has proven to be sufficient in providing enough cooling for the engine to run within acceptable operating limits in the summer. The water pump is controlled manually via an electrical switch on the front panel. Moreover, during engine operation, the computer program employed regulates the water pump such that it activates automatically when the temperature of the engine coolant exceeds a threshold of 165°F.

Additionally, the Syngas Rig has been reconfigured such that the operation of the entire system can be controlled using mechanical switches inside the rig, in conjunction with electrical switches using digital and analog signals from the data acquisition (DAQ) system. Moreover, safety measures were implemented in the fuel system in order to prevent any unintentional activation of fuel flow. For instance, as a safety precaution, now the master propane solenoid (#1) activation requires both the mechanical switches on the control panel and an electric relay controlled digitally, by the DAQ system to be ON. Similarly, all the operation paths require the activation of both mechanical and electrical switches by wiring in series instead of through parallel circuits.

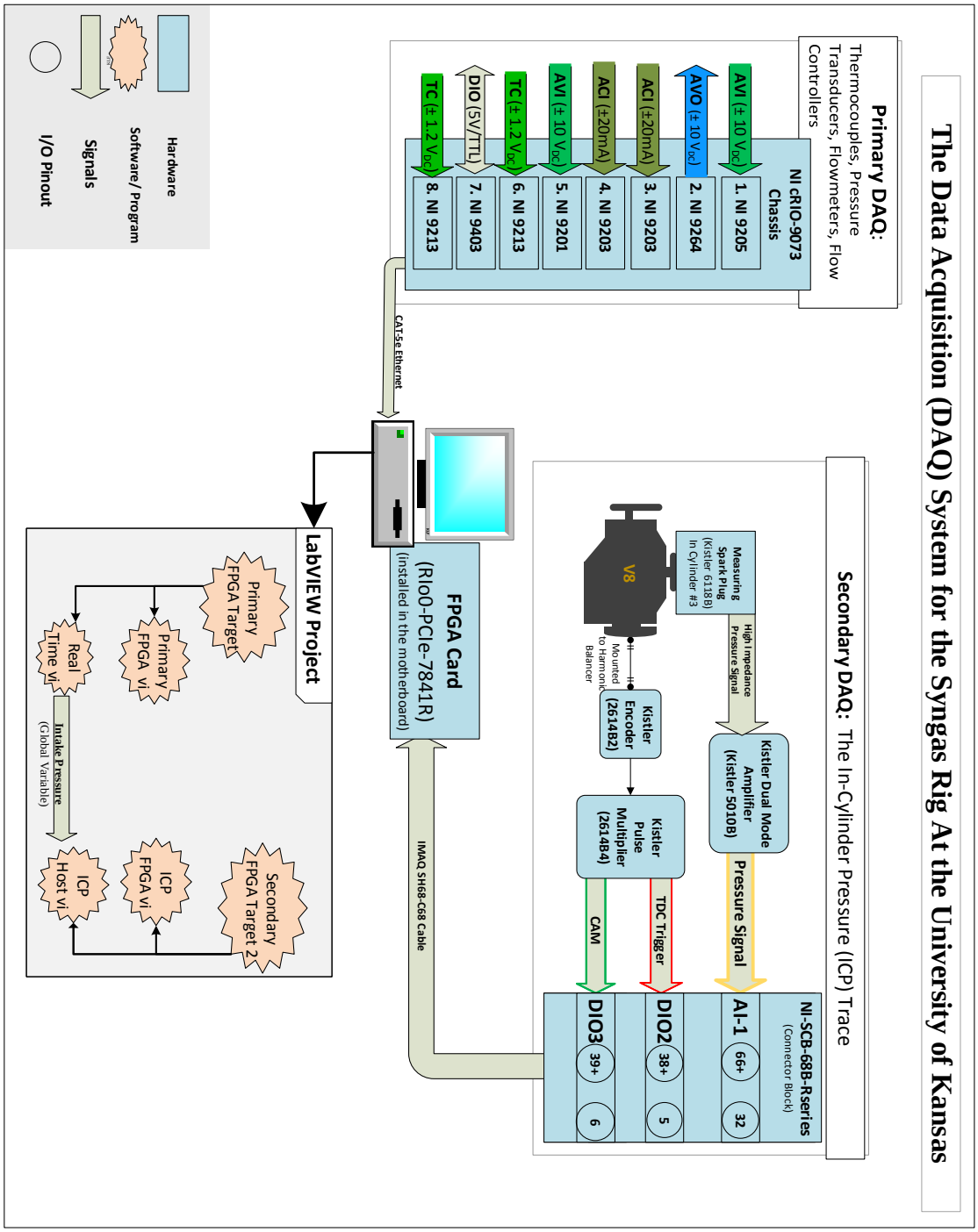

Figure 4: Flow Diagram of the Primary and Secondary Pathways for the Syngas Rig DAQ System

2.2 Primary DAQ

The data acquisition and control system consists of two systems working in parallel during full operation of the Syngas Rig. The first system, referred to hereinafter as the Primary DAQ, is responsible for reading and recording the input signals from the various sensors that measure temperatures, pressures, and flow rates of the Syngas Rig at different locations. Additionally, the Primary DAQ is responsible for controlling actuators and flow controllers that modulate the flow pathways of the system. The Primary DAQ is composed of a National Instruments (NI) CompactRIO controller (cRIO-9073 chassis) which hosts eight NI modules that control and monitor analog voltage input (AVI), analog voltage output (AVO), analog current input (ACI), and digital input-output (DIO) signals [16]. Figure 4 illustrates a flow chart of the Syngas Rig DAQ system. Moreover, an updated description list of the Primary DAQ modules for the sensors and controllers installed in the Syngas Rig is included in (Table 3 and Table 4) in Appendix (A).

2.3 Secondary DAQ: ICP

The Secondary DAQ system utilizes high-speed in-cylinder pressure (ICP) measurements as the essence of the combustion analysis. This is because the acquired pressure data are instantaneous and a direct measure of the engine performance [18]. This indicator system can be operated in one of two measurement modes: monitoring (displaying) or recording. For instance, a cylinder pressure versus crank angle diagram illustrates an immediate depiction of engine combustion quality. Alternatively, for energy analysis, the indicated performance parameters can be used to calculate cycle work distribution, net heat release estimation, and cyclic variation [19]. As an indicator system, the acquisition of ICP is typically measured on a crank angle basis because the events of the engine are dependent on crankshaft rotation (e.g., motion of the piston, fuel injection, spark timing, etc.) [20]. Therefore, the Secondary DAQ includes an optical encoder to synchronize the pressure measurement to the crank angle position. This is accomplished by mounting the optical encoder on the crankshaft.

During engine testing, the ICP program can be used to save 60 engine cycles of pressure data; in essence, taking about 4.1 seconds of data at an engine speed of 1800 rpm. When data are not being saved,

the ICP program monitors the in-cylinder pressure (in bar) plotted as a function of crank angle (in degrees after top dead center or °ATDC). In this monitoring operation, averages of 20 engine cycles of data (1.4 seconds at 1800 rpm) are plotted, along with indicators for the peak pressure (bar) and peak pressure location (°ATDC). This monitoring mode is a valuable tool during engine testing in order to ensure that the engine calibration and mapping is performed within safe limits. Of importance, the in-cylinder pressure data acquisition (ICP-DAQ) system was initially based on routines developed by Michael Mangus for the Yanmar single-cylinder engine test cell [21].

The various components of the Secondary DAQ must be in synchronized in order to acquire a valid set of high-speed in-cylinder pressure data. With this in mind, multiple troubleshooting tools were implemented in the Secondary DAQ system during the re-installation of this system at HERDC in order to aid in pinpointing problems. More importantly, a complete understanding of this system is undoubtedly important during diagnostics or when modifying the system. Therefore, the working mechanism of the Secondary DAQ system is reviewed here. The components of this system can be categorized or sorted as a function of hardware device, program algorithm, or signal waveform. Afterward, the troubleshooting process of the previous version and/or adaptation is overviewed.

2.3.1 Signal Source (Kistler Encoder and Measuring Spark Plug)

The pressure signal (yellow color-coded in Figure 4) is an analog signal measured by a spark plug that incorporates a piezoelectric high-temperature cylinder pressure transducer (Kistler 6118B), while maintaining the functionality of the spark plug [22]. For conditioning the pressure signal, a dual mode amplifier (Kistler 5010B) is used to amplify the charge signal from the measuring spark plug into a proportional output voltage. The dual mode amplifier is configurable to the specifications of the sensor and the DAQ program. The current setting and specifications of the amplifier used in the Syngas Rig are listed in Table 1.

Table 1: Summary of Kistler (5010B) Dual Mode Amplifier Configuration Settings

Configurable Parameter	Value	Description
Amplifier Operation Mode Selection	Charge Mode	To measure Kistler 6118B, a high impedance piezoelectric transducer
Transducer Sensitivity (pC/MU)	-10 (pC/bar)	In Picocoulomb per Mechanical Unit or pC/MU, with bar being the mechanical unit measured
Scale (MU/V_{DC})	2 (bar/V_{DC})	This scale is used to calculate the in-cylinder pressure using this formula: pressure (bar) = Scale (2 bar/VDC) × Measured Voltage

In a combustion indicator measurement, the indicated quantities derived from the pressure data curve are related to the crank position or the cylinder volume. Hence, the acquisition of pressure data must be sampled in an angular domain; as opposed to time domain based DAQ systems (e.g., oscilloscope). In particular, the absolute position of the engine (measured in degrees) is established as the clock domain of the pressure data, with the top dead center (TDC) position used as the reference signal [23]. Therefore, an optical encoder (Kistler 2614B2) is mounted to the free end of the crankshaft (i.e., front of engine) in order to synchronize the pressure measurement with crank angle position by transmitting two digital signals. First, the TDC trigger signal operates as the reference clock by generating a single pulse per revolution. Specifically, the detection of this TDC signal triggers the recording session and the beginning of a new revolution. Simultaneously, the encoder provides the clock signal by streaming a train of symmetric pulses at evenly spaced crank angle marks (CAM). Then, the DAQ system gates the pressure measurement by the rising and falling edges of the CAM pulses. In other words, the encoder provides the CAM signal that is used to correlate the recorded pressure to the engine crank angle. Moreover, the encoder is connected to a pulse multiplier (Kistler 2614B4) that outputs the two signals as transistor–transistor logic (TTL)-type signals. A TTL signal is a digital signal characterized by a specific output voltage range and a maximum rise and fall time of 50 nanoseconds [24]. Furthermore, the pulse multiplier includes dual in-line package (DIP) switches that control the resolution of the CAM signal as defined by the number of pulses per crankshaft revolution.

2.3.2 Initial Encoder Phasing and Procedures of Marking TDC

The optical encoder includes a flange that is mounted concentrically on the harmonic balancer via an adapter. Prior to securing the encoder's flange, the TDC trigger signal must be calibrated to the geometrical TDC of the third cylinder. This is achieved by rotating the engine by hand until the TDC mark on the harmonic balancer is aligned with the reference (stationary) mark on the indicator tab mounted to the engine's cylinder block. This is needed because an accurate determination of the indicated mean effective pressure (IMEP) requires a correct phasing between piston position and crank angle [19]. However, a recent replacement of the harmonic balancer required the remaking of this TDC mark. Specifically, the new harmonic balancer has been marked twice for the TDC of cylinders one and three. The TDC mark for the first cylinder (TDC-1) is used as the base for spark timing control. Additionally, in-cylinder pressure (ICP) is measured from the third cylinder; therefore, the trigger signal from the encoder is aligned with top dead center of the third cylinder (TDC-3).

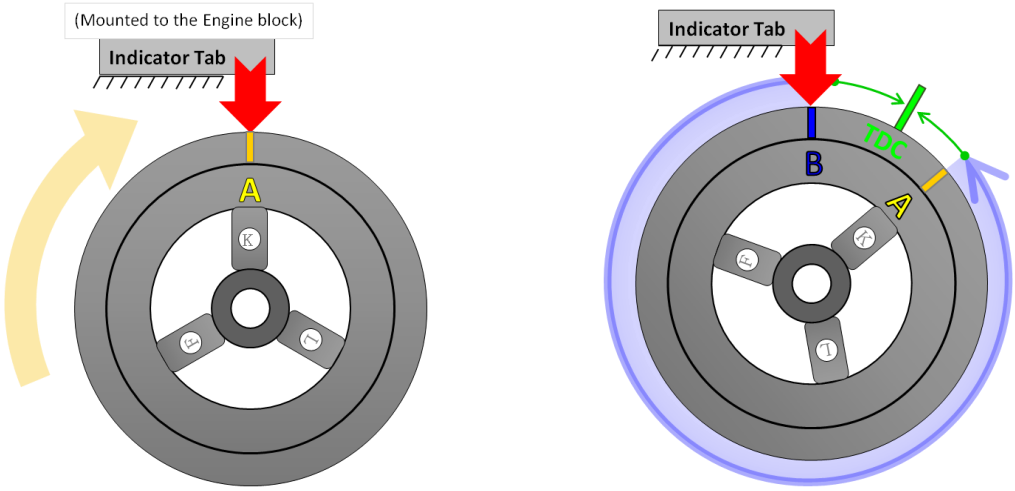

(a) Clockwise Rotation (Mark A) **(b) Counterclockwise Rotation (Mark B)**

Figure 5: The Process of Determining the Top Dead Center

To begin the marking procedure, with the engine turned off and at a standstill, a piston-stop tool was installed in the third cylinder spark plug port in order to prevent the full rotation of the crankshaft. Then, the crankshaft was rotated clockwise slowly by hand until the engine reached a firm stop when the rising piston was blocked from reaching TDC by the installed tool. At this point, a small mark was placed

on the harmonic balancer (Mark A) at the indicator tab. Next, the crankshaft was rotated counterclockwise until reaching a firm stop again and another mark was placed on the harmonic balancer (Mark B). Top dead center is then marked at the mid-point of the arcs of the minor sector that did not pass by the indicator tab with demonstration of this process shown in Figure 5.

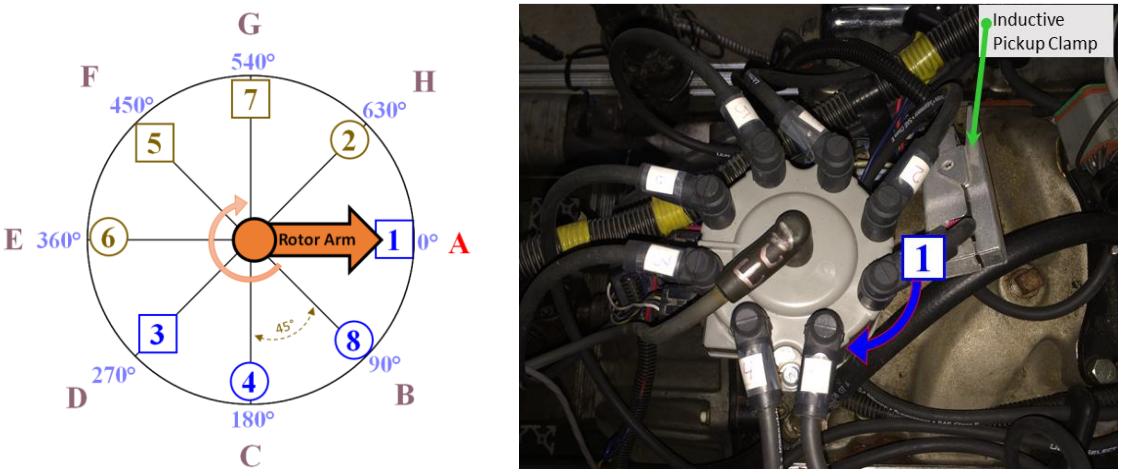

(a) The Rotor Arm Under the Distributor Cap (b) Spark Plug Terminal in the Distributor Cap

Figure 6: The Rotor Arm Position, Relative to the (a) Harmonic Balancer and (b) Distributor Cap

Next, the initial spark timing was recalibrated after establishing the new TDC location. The following process of calibrating this timing was performed with the engine held at a standstill. After establishing the TDC location of the first cylinder, the initial base (static) spark advance is phased with the TDC mark on the harmonic balancer (TDC-1). First, the rotor arm under the distributor cap is aligned with the terminal pole for the first cylinder. A demonstration of the relative position of the rotor arm is shown in Figure 6. Before adjusting distributor cap, the first cylinder must be verified to be at the end of the compression stroke, otherwise the spark timing would be off by 180°. This stroke can be identified by observing the release of compressed air from the cylinder, prompted by the opening of the exhaust valve (EVO). Next, the inductive pickup clamp of the ignition timing stroboscope (Actron CP7527) is attached to the spark plug cable of the first cylinder. With both the ECU and the fuel system disabled, the starter is used to crank engine while the stroboscope is pointed toward the timing tape. This spark timing is then established as the initial spark advance, since in the current setup, all of the dynamic advancing additions are performed solely by the ECU, replacing the mechanical advancement mechanisms (i.e., centrifugal

and vacuum) as detailed in next chapter. In order to calculate the true total spark timing accurately, the initial spark advance (12° BTDC) parameter in the calibration files is employed by the ECU to calculate the dynamic spark advance, offsetting the base timing of the distributor. Overall, the matching of an initial spark advance parameter to the physical base timing of the distributor is essential for a safe and accurate spark timing sweep.

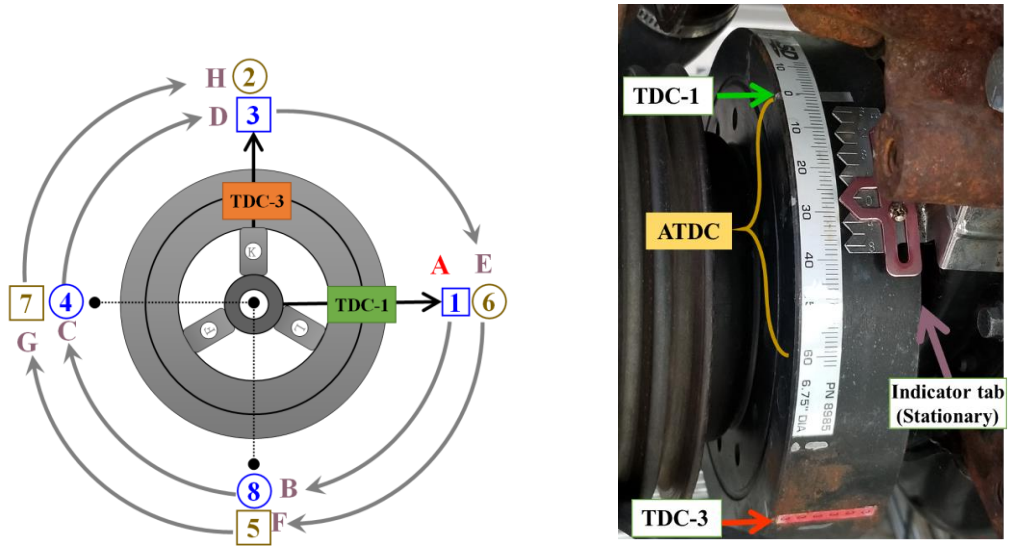

(a) Firing Order Illustration on the Harmonic Balancer (b) The Spark Timing Tape

Figure 7: Plausibility Tests: (a) Firing Order Location in Relation to the Harmonic Balancer and (b) the Spark Timing Tape

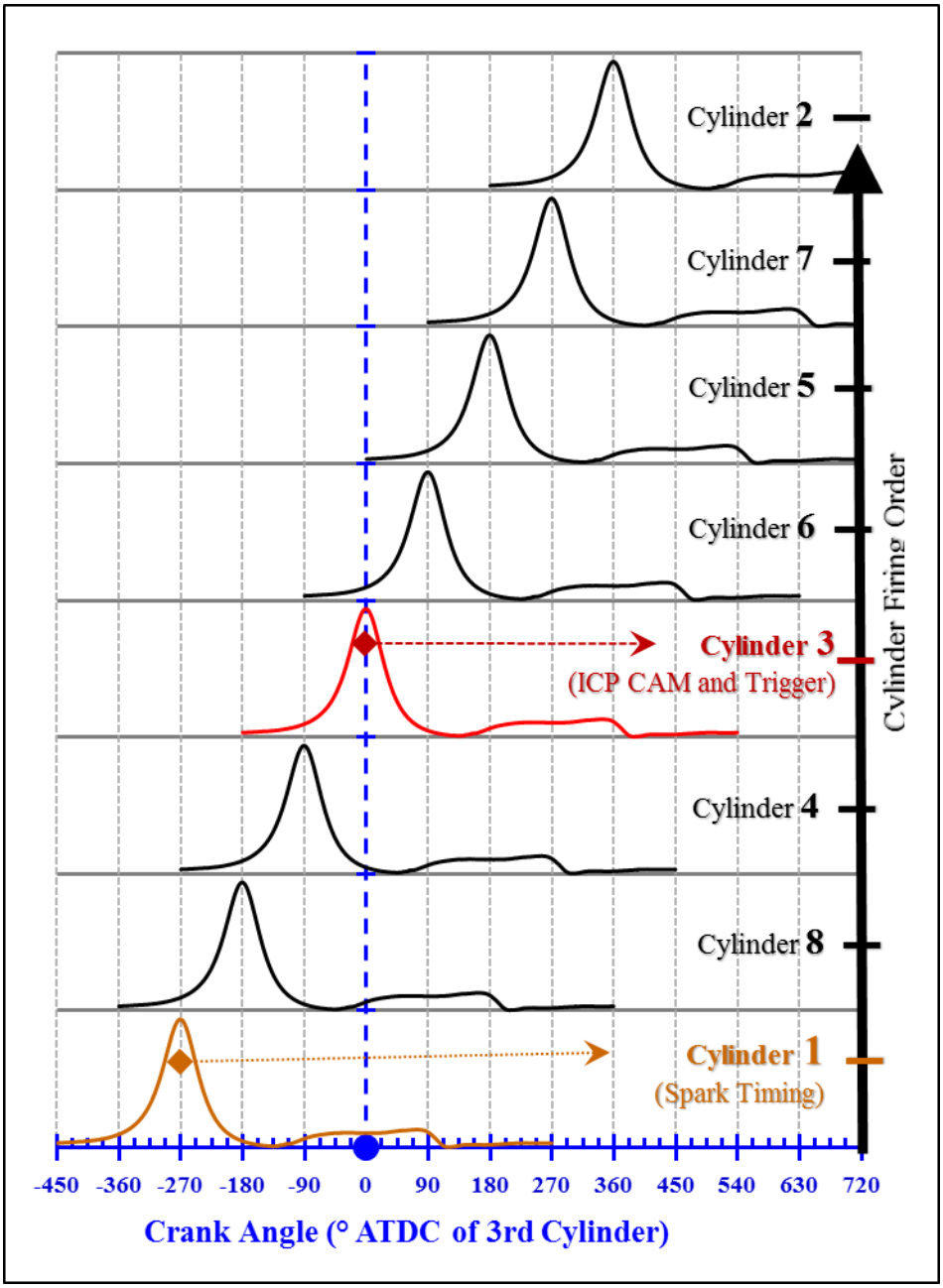

Figure 8: Motoring Signal, Superimposed on All Cylinders, Based on the Firing Order

In the current setup, the two TDC marks are utilized independently. Namely, the TDC of first cylinder (TDC-1) is used as the base for spark timing while the TDC of the third cylinder (TDC-3) is used as the trigger mark for the in-cylinder pressure system. In order to examine spark advance trends via the ICP system, the motoring traces of the first and third cylinders were measured as a validation test for the located marks. The crankshaft of the syngas engine is identified to be of a cross-plane type, an anti-symmetrical, 4-throws, crankshaft with the cylinder banks at 90° (V angle). Moreover, using the firing

order specified for this engine (i.e., 1st-8th-4th-3rd-6th-5th-7th-2nd) [25], the angular displacement from TDC-1 to TDC-3 is estimated to be 270 CA° (CW). Additionally, using the harmonic balancer radius (3.375 inches) specified for the installed harmonic balancer (GM 594-006), the arc length between the two marks is calculated as 5.30 inches. Figure 7 demonstrates the geometrical relationship between the two marks and the installed timing tape (MSD PN 8985) that includes the graduation marks used for the initial spark timing. Finally, the established geometrical relationship between the eight cylinders is demonstrated in Figure 8 by superimposing the motoring trace of the third cylinder for all the cylinders, in accordance with their firing order.

2.3.3 Signal Sink (DAQ)

At the receiving end of the signals, a personal computer (PC) running on Microsoft Windows 7 is equipped with a peripheral component interconnect express (PCIe) expansion slot (NI 7841R). This device includes a multifunction reconfigurable input/output (RIO) chip that contains multiple analog input channels (AI), analog output channels (AO), and digital input/output (DIO) lines that can be programmed using a LabVIEW field-programmable gate array (FPGA) module. Moreover, the NI 7841R includes three direct memory access (DMA) channels that are used for streaming high-speed data to the computer [26].

Practically, an analog input (such as the pressure signal) is sampled by converting the input from a continuous-time signal into a discrete-time signal using an analog-to-digital (A/D) converter integrated in the AI channel [27]. In the case of NI 7841R, the analog input is sampled at a maximum rate of 200,000 samples per seconds (200 kS/s) at a resolution of 16-bits. On the other hand, for a DIO channel, a TTL-compatible signal is represented in binary by zeros and ones when the voltage measured ranges are 0.0-0.8 VDC and 2.0-5.5 VDC, respectively [26]. A major advantage of sampling in the digital domain is the elimination of signal distortion introduced by the A/D conversion. Indeed, practical devices that include A/D converter are prone to time-related degradations, such as signal jitter (error in sampling period), aperture distortion (nonlinear variations in the duration of the sampling aperture), and droop (changes in the voltage held during conversion) [27].

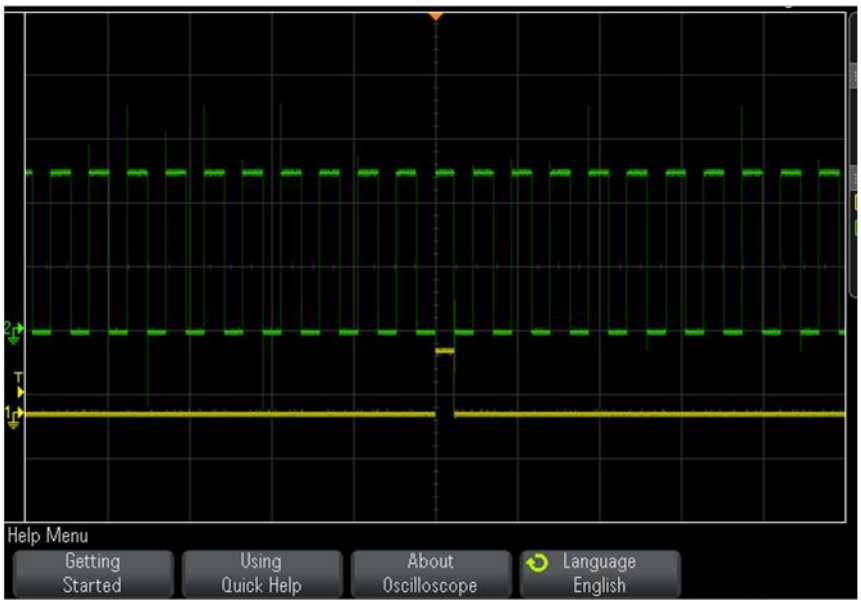

(a) CAM Signal (Green) Waveform, Triggered by TDC Signal (Yellow)

(b) Pressure Signal (Green) Waveform, Triggered by TDC Signal (Yellow)

Figure 9: Screenshots of the Oscilloscope Display Showing (a) CAM Signal Triggered by TDC and (b) Pressure Signal, Triggered by TDC

2.3.4 Troubleshooting Signal (Oscilloscope)

Initial attempts to deploy the ICP program at HERDC were unsuccessful using the previous program that was employed by Pickett [16]. Furthermore, in the case of a successful start of the program, maintaining a continuous session of data acquisition proved to be difficult. Therefore, in order to isolate the source of the problem, a troubleshooting procedure was performed on the Secondary DAQ system

components in a systematic checklist fashion. This covered the hardware and software components of the system by following the paths of the three signals. First, the sources of the signals were examined via a portable oscilloscope (Agilent DSO-x-2012a-200) while the engine operated under steady-state conditions. This oscilloscope includes a Universal Serial Bus (USB) port that can be used for printing the displayed graph, exporting the data to a text file, or streaming the data to a connected PC. The three main signals under analysis as shown in Figure 4 were the pressure (yellow color-coded), top dead center trigger (TRG, red color-coded), and crank angle measurements (CAM, green color-coded). Note that this color-coding was established during troubleshooting of the system in order to aid in distinguishing the connections of the three signals. When testing the CAM signal, the TDC signal was connected to the oscilloscope via an external trigger. The initial display of the three signals exhibits an anticipated waveform with Figure 9 providing a screen image for the examined signals.

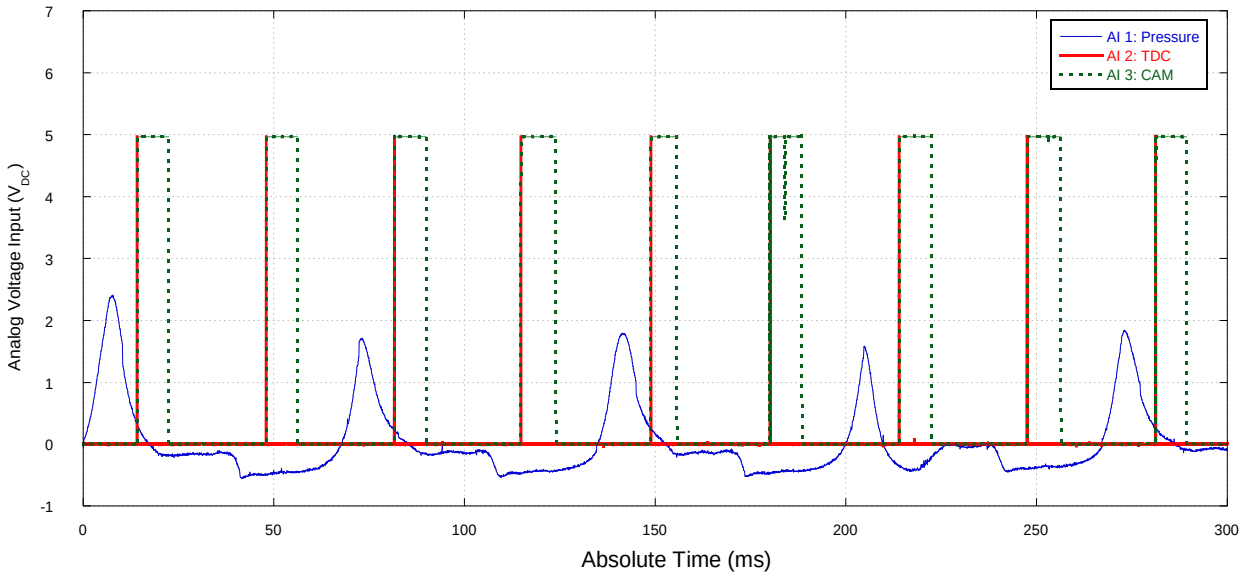

Figure 10: Virtual Oscilloscope Data Using Analog Input Channels in NI 7841 R (Spark Advance Has since Been Changed)

Next, in order to examine the DAQ components (signal sink), a virtual oscilloscope tool was created in LabVIEW to measure the three signals via the AI channels of the NI 7841 card. This simulated the algorithm of the initial ICP program. The results showed that the virtual oscilloscope program was incapable of measuring at the sampling rate required to detect the CAM signal as highlighting by a plot of the raw data as collected by the virtual oscilloscope shown in Figure 10.

While the hardware timing specifications indicate an AI sampling rate capable of detecting the CAM signal (200 kS/s), the sampling of three analog signals reduced the rate at which the system can process inputs (i.e., throughput or bandwidth). According to the Nyquist Sampling Theorem, the sampling rate (defined as the rate at which the ADC changes the analog input waveform to digital data) must be greater than twice the frequency of the measured signal [28]. In the ICP architecture, this specifies that the DAQ system must sample at twice the resolution of the CAM signal. This is because the DAQ architecture has three delays when converting a physical-measurement into a software algorithm. The first delay involves signal conditioning during the A/D conversion. The second delay is a hardware communication delay between the A/D converter and the software host system (i.e., PC). The third delay is a software delay involving data processing and the associated transferring algorithm [29]. In general, two parameters control the processing delay: throughput and latency. The throughput is related to the total number of pressure data recorded and stored on the FPGA card while the latency is defined as the time required to complete an operation. Reducing the processing delays can be accomplished by increasing the throughput and reducing the latency [30].

2.3.5 New ICP LabVIEW Program

The ICP programs, known as virtual instruments (VIs), were written in the LabVIEW programming language based on versions previously developed by Michael Mangus that recorded and displayed the pressure for 20 consecutive cycles [16, 21]. The first VI (FPGA VI) runs on the PCIe chip; whereas, the second VI (Host VI) runs on the main PC. Upon initiation, the FPGA VI is executed on the FPGA card for 122 or 42 engine revolutions when collecting data or during monitoring, respectively. Then, the pressure data are transferred via a DMA channel to the Host VI that runs on the PC. A recent rewriting of the ICP code increased the data throughput to 61 consecutive cycles by changing the code with one cycle consistently used as a trigger buffer. In the updated version, the TDC trigger and CAM signals are now processed as digital inputs instead of analog signals. More importantly, this new version eliminated a timing issue that the system suffered when moving to HERDC. Specifically, a jitter in the CAM signal interrupted the execution of the FPGA VI. While the installed FPGA reconfigurable

input/output (RIO) device includes both analog and digital channels, measuring a signal through an analog channel is more computationally intensive when compared to a digital channel input. In fact, for the FPGA LabVIEW, a digital input is processed as a single bit of storage (a Boolean value) while an analog signal is processed as 16-bits of memory [31]. Therefore, both the CAM and TDC signals are currently connected to the FPGA RIO as digital inputs. As a result, the decrease in the time that the program takes to perform a single iteration (i.e., latency) resolved the jitter issue.

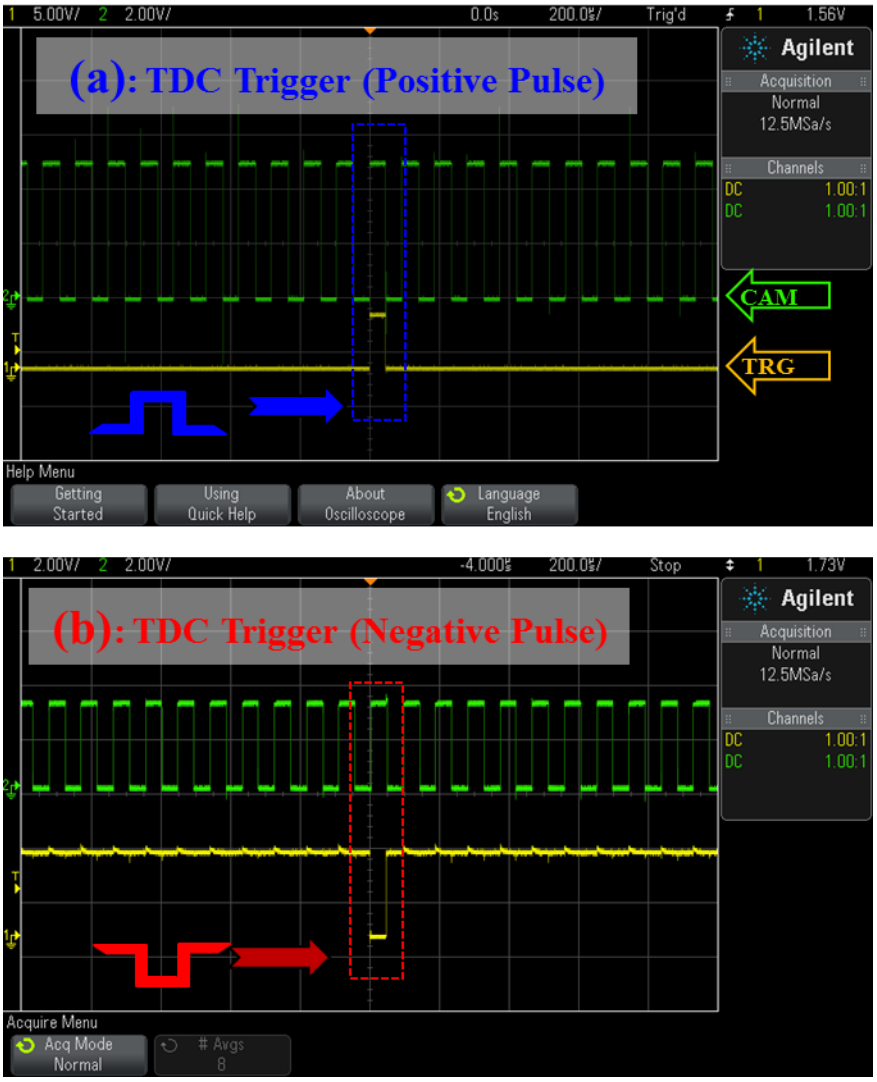

Figure 11: The Change in the TDC Triggering Polarity: (a) Previously and (b) Currently.

Furthermore, the new change has resulted in an increase in the throughput of the system [29]. Hence, a 60 cycle analysis is now used as the standard for data collection instead of 20 cycles in order to reduce statistical anomalies (i.e., to increase the accuracy of the average). Additionally, in the new

program, the polarity of the TDC trigger signal has been inverted such that a low-level pulse triggers the TDC position. By using this triggering convention, a high-level signal is used to verify the integrity of the TDC signal, eliminating the possibility of an improper wire connection or inadequate power supply to the encoder as shown in Figure 11.

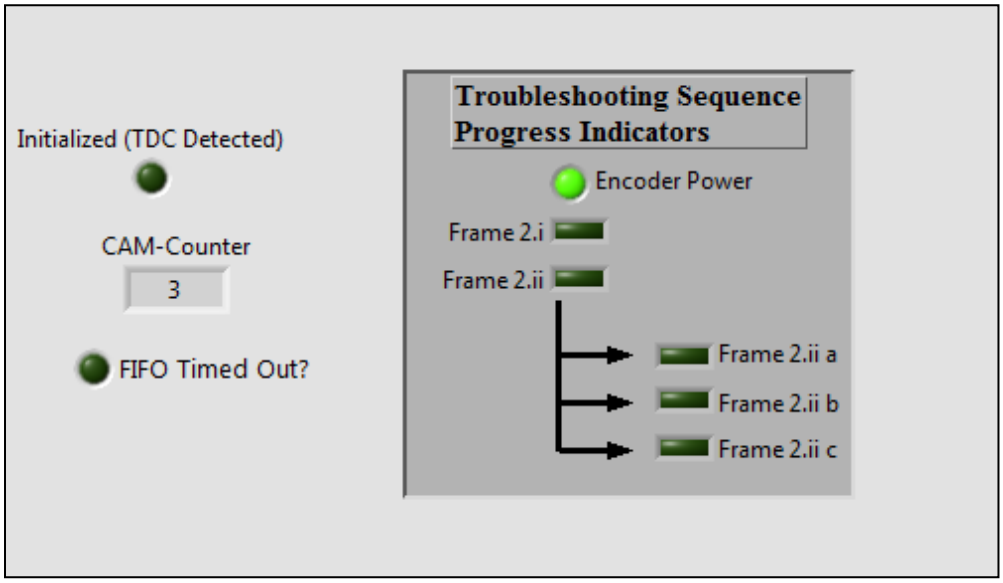

Figure 12: ICP FPGA VI GUI (Front Panel)

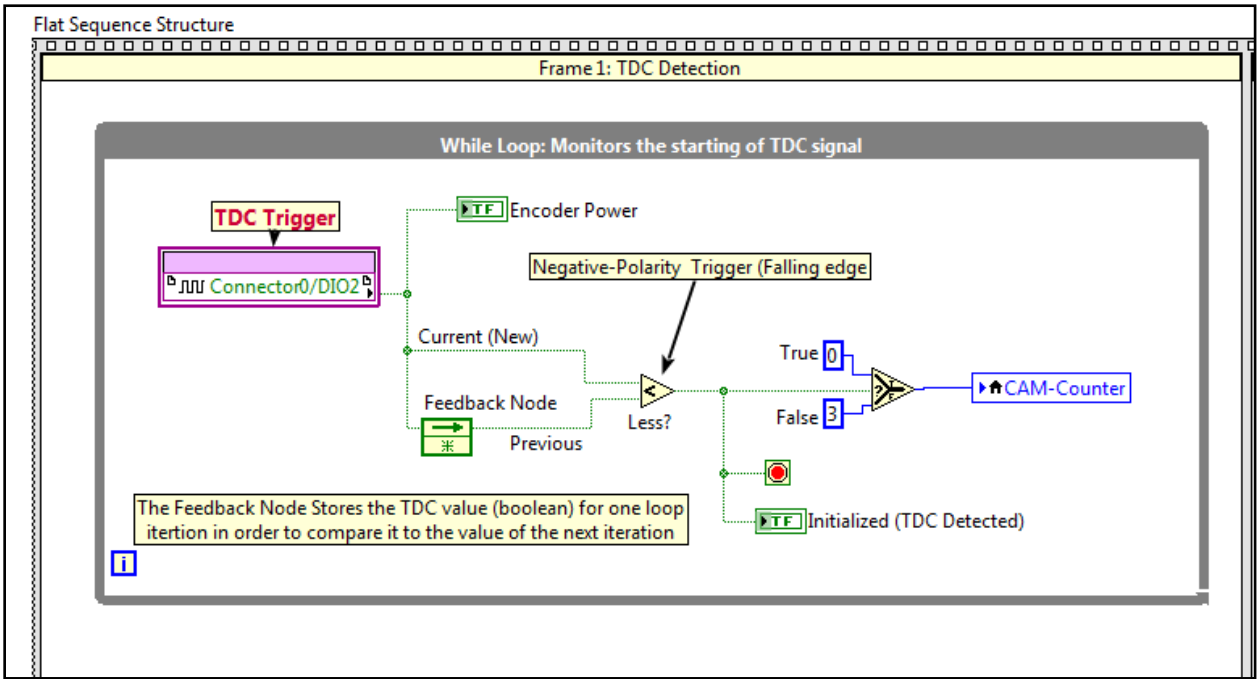

Figure 13: ICP FPGA VI Block Diagram: Frame 1: Initialization and TDC Detection

2.3.5.1 ICP FPGA VI

In order to understand the algorithm used by the ICP LabVIEW program better, this section provides a frame-by-frame description of the FPGA VI code. The FPGA VI (Figure 12) is a single-run code, in other words, no conditional loop that encompasses Frame 1 and Frame 2). The code is first booted when the Host VI calls it using the command "FPGA invoke". This method of booting the FPGA VI is essential for consecutively switching between different FPGA VI versions (i.e., 20-cycle monitoring and 60-cycle data collection) without the need for resetting the FPGA card. Specifically, the 20-cycle FPGA VI is used for monitoring a more rapid response as it executes in 1.4 seconds while the 60-cycle FPGA takes about 4.1 seconds to collect all data. When the FPGA VI is called, a single run of the code is executed sequentially in multiple, multilevel sub-diagrams. This is known as a flat sequence structure with the data flowing in "wires" from left to right in the following order:

1. **Frame 1 (TDC Detection):** This frame includes a while loop that continuously reads digital input 2 (DIO2), the input channel for the TDC trigger signal. A negative polarity signal was selected with DIP switch #1 on the Kistler pulse multiplier. This trigger convention was chosen in order to add an indicator for the encoder power, ensuring proper operation of the TDC signal. Specifically, prior to starting the engine, a 5 VDC signal will turn on the LED indicator "Encoder Power" in Figure 13, unless the third piston is exactly at TDC position. Then, a feedback node is used to store the TDC value (Boolean) for one iteration. Once a falling edge is detected, this comparison function returns a true value (i.e., current value is less than the previous value). In this case, a CAM-pulses-counter is set to zero and the while loop is stopped. Thus, a trigger signal terminates the TDC detection loop, advancing the program to Frame 2.

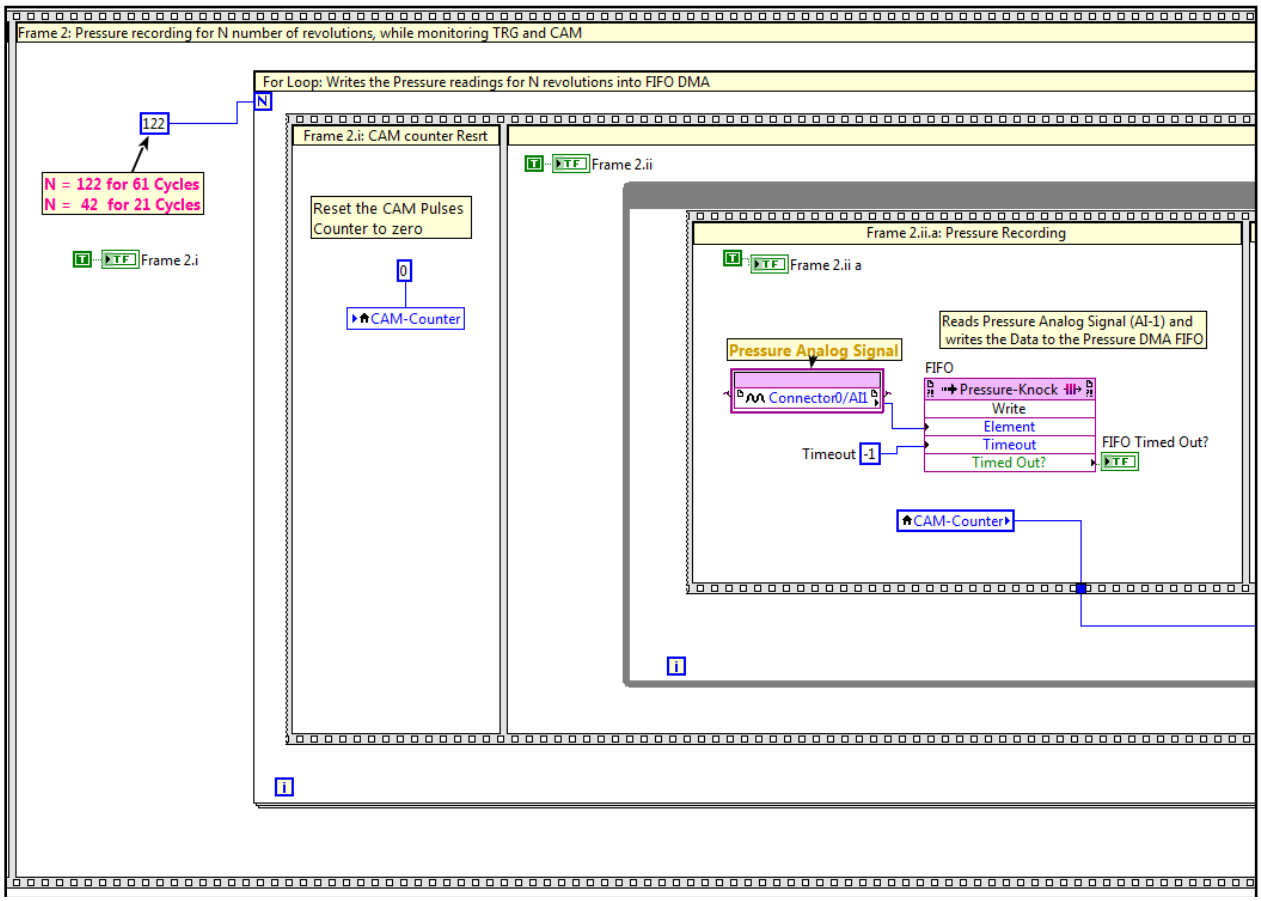

Figure 14: ICP FPGA VI Block Diagram: Frame 2: Pressure Recording for N Number of Revolutions

2. **Frame 2 (Data Recording)**: A for loop is executed where N is the number of times this code is performed; e.g., 122 revolutions when saving data or 42 revolutions for monitoring. Each iteration of this frame is executed over a full engine revolution, during which time the pressure is acquired at every edge of the CAM pulse and saved to a pre-allocated memory structure, known as DMA FIFO (i.e., first-in-first-out direct memory access). Overall, a single loop of Frame 2 entails the sequential execution of the following sub-diagrams (see Figure 14). Overall, a single loop of Frame 2 entails the sequential execution of the following sub-diagrams:

i. **Frame 2.i:** The beginning of a new revolution starts by resetting the CAM-pulse-counter to zero.

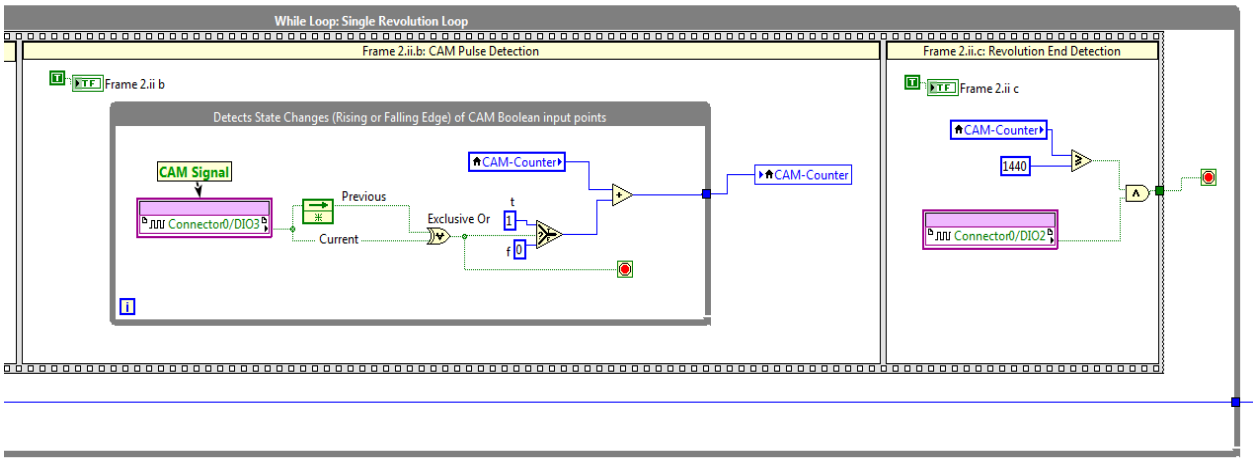

Figure 15: ICP FPGA VI Block Diagram: Frame 2.ii (Single Revolution Loop)

ii. **Frame 2.ii (Single Revolution While Loop):** This frame runs in a while loop that stops at the end of each revolution (i.e., CAM counter reached a predetermined limit). Overall, the while loop is terminated when another TDC signal is detected and the CAM-pulse-counter has reached 720 (see Figure 15). At 0.5° CA resolution, a single revolution includes 720 edges (i.e., 360 symmetric pulses). Until terminated, this while loop repeats the execution of the following frames:

a. **Frame 2.ii.a (Pressure Recording):** The pressure signal is read from Analog Input 1 (AI1) and written to the DMA FIFO memory. This FIFO is specified to run on the FPGA block memory with an allocated buffer value of 87,840 elements for the 60-cycle version. The *DMA Buffer* size is calculated using Equation (1):

$$\text{DMA Buffer Size (elements)} = \left(\frac{N_{FPGA}}{n_R}\right) \times \left(\frac{\text{CA Window}}{\text{CAM resolution}}\right) \quad (1)$$

where N_{FPGA} is the total number of consecutive engine revolutions measured in a single FPGA VI execution (122 revolutions), n_R is the number of crankshaft revolutions in a thermodynamic engine cycle (n_R =2 revolutions per cycle for a four-stroke engine), the *CA windows* is the total range of sampled Crank Angle per engine cycle (720 °CA per cycle), and *CAM resolution* of the encoder that gates the pressure sampling frequency (0.5° per element).

b. **Frame 2.ii.b (CAM Pulse Detection)**: A while loop is used to read the CAM signal that is connected to Digital Input 3 (DIO3). Then, using a feedback node, an "exclusive or" (XOR) gate is implemented between the current value and the previous Boolean value.

   (False): The while loop continuously for a positive edge (Low-to-High Transition) or a negative edge (High-Low Transition)

   (1) If the gate returns a true value (i.e., CAM pulse detected), then the CAM pulse counter is increased by one, the while loop is terminated, and code execution advances to Frame 2.ii.c,

   (2) , otherwise, the while loop continuous detecting for CAM Signal change while the XOR gate outputs a false.

c. **Frame 2.ii.c (The Revolution-End Detection):** The TDC trigger (Digital Input 2) value and the CAM pulses counter comparison are used in an AND gate to end the while loop.

   (1) If a true value is returned (i.e., a new revolution trigger has been detected and the CAM-pulses-counter reached 720), the while loop of a single revolution is terminated (Frame 2.ii). Then, the program starts another "for loop" starting from Frame 2.i.

   (2) If a false value is returned (i.e., a complete engine revolution has not been reached), the pressure signal reading is repeated, starting from Frame 2.ii.a.

At the end of the specified number of revolutions, the "for loop" in Frame 2 ends and the FPGA VI is finished. Moreover, to aid in monitoring the progress of the code during troubleshooting, sequence indicators are added to the frames such that these indicators are lit on the front panel (Figure 12) when the code reaches the corresponding section.

2.3.5.2 ICP Host VI

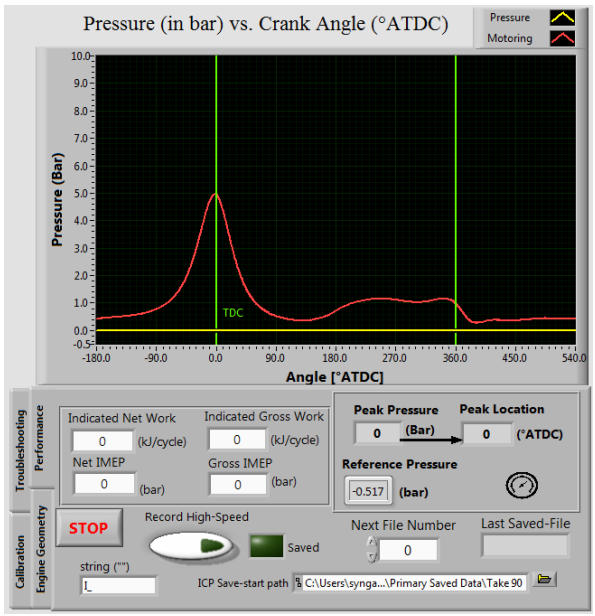

(a) Performance (Indicating) Tab

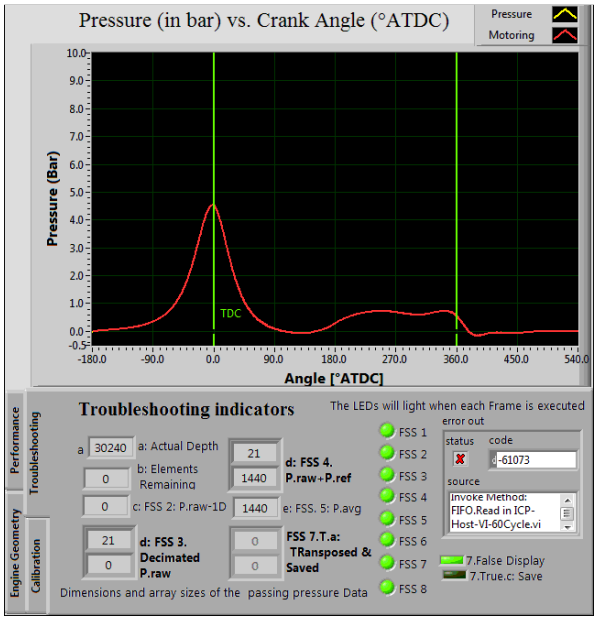

(b) Troubleshooting Indicators Tab

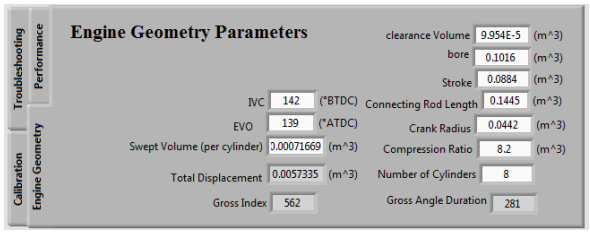

(c) Engine Geometry Parameters Tab

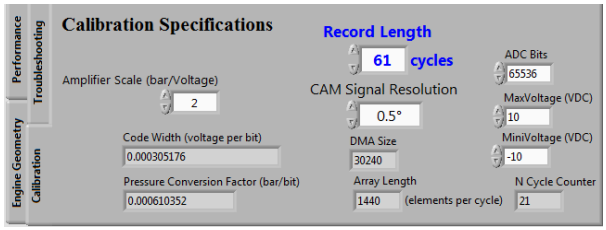

(d) Calibration Specifications Tab

Figure 16: ICP Host VI Front Panel: ICP Trace Graph: The Controls (Inputs) and Indicators (Output) are Split into Four Stacked Pages

The Host VI renders a graphical user interface (GUI) for the operator to display the pressure trace plot. The controls (inputs) and indicators (outputs) of the Host VI are divided among four stacked pages (tab control) based on their function, as shown in Figure 16.

a) Performance (default tab): Displays the indicated performance parameters, peak pressure and peak pressure location, record button, and the incremental file name number and path. For the spark sweep mapping, an auto-save function was added that enables the automatic saving of the text files as incremental numeric names (e.g., I_001.txt, I_002.txt, etc.) in a specified folder. Moreover, during the spark timing sweeps, the saving functions for the primary and secondary DAQ were synchronized using a push button that prompts auto-saving of both files.

b) Troubleshooting Indicators: LED indicators were placed in each flat sequence structure (FSS). By turning ON, the LEDs display the progress of the program. Moreover, the size of the DMA buffer is specified in order to prevent critical errors, such as accumulating stale data in the buffer [32].

c) Engine Geometry Tab: Specifies the combustion chamber dimensions and specifications of the testing engine.

d) Calibration Tab: The values of the hardware and software parameters used, such as the Kistler amplifier, encoder, DMA recording length, NI input range, etc. (as detailed in following section).

In addition to calling and running the FPGA VI, the Host VI is responsible for collecting, processing, sorting, and offsetting the pressure data. Similar to the FPGA VI, the Host VI runs successively in a frame sequence structure as follows:

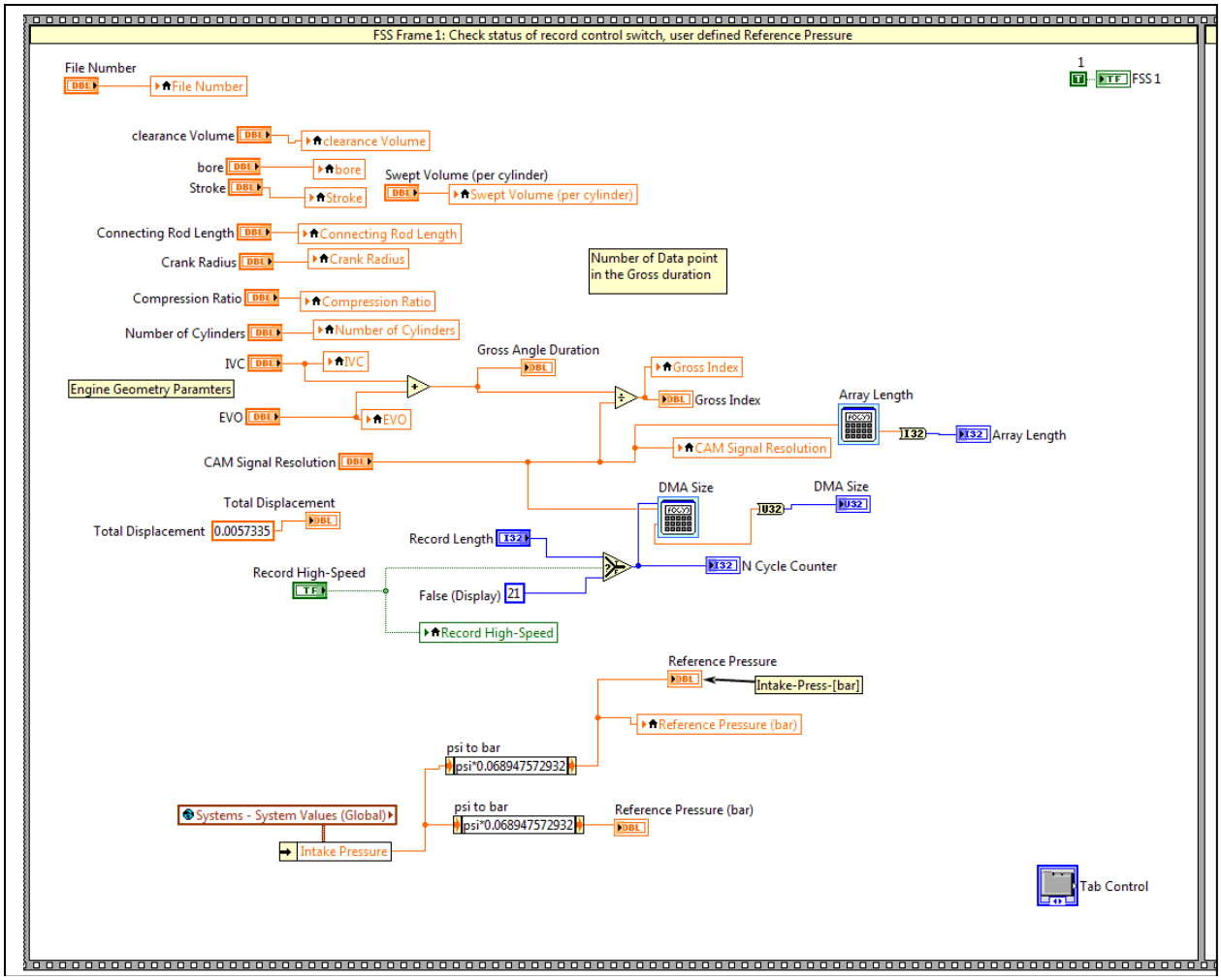

Figure 17: ICP Host VI: Frame 1: Assign Engine Parameters to Local Variables

1. **Frame 1 (Assigning Local Variables)**: The first frame (shown in Figure 17) is tasked with assigning the initial values of the inputs and outputs into local variables that are accessible in the subsequent frames. For instance, the Record Control button on the front panel is used to determine the scheme of subsequent code frames (i.e., display or record). Additionally, various inputs and constants (e.g., engine specification, calibrations parameters, etc.) are assigned to local variables. Moreover, Frame 1 is used to read the intake pressure data from a global variable (written by the Primary DAQ VI) and assign it to a local variable (reference pressure), which is then used for pegging the in-cylinder pressure in the fourth frame [21]. Lastly, in the first frame, indexing parameters that pertain to organizing the data structure are defined as following:

$$\mathrm{N_{Host}} = \begin{cases} 21 \text{ cycles}, & \text{if False (Display)} \\ 61 \text{ cycles}, & \text{if True (Record)} \end{cases} \tag{2}$$

where N_{Host} is the total number of engine cycles collected and processed in the current loop run of the Host VI. Additionally, the *Array Length* (in elements per cycle) is the number of data elements in a single cycle array; calculated N_{Array}:

$$\mathrm{N_{Array}} = \frac{\text{Sampling Window}}{\text{CAM resolution}} \tag{3}$$

where *Sampling Window* (in CA° per cycle) is the crank angle range where pressure is either recorder or displayed and the *CAM resolution* (in CA° per elements) is the smallest step width that is used for discretization of the pressure signal [33]. Also needed is *DMA Acquire Size* that is the total number of raw elements to be obtained from the DMA buffer memory in Frame 2:

$$\text{DMA Acquire} = \mathrm{N_{Host}} \times \mathrm{N_{Array}} \tag{4}$$

Another parameter required, *Gross Combustion Duration*, is the number of pressure elements used to calculate the gross indicated parameters, N_{Gross}:

$$N_{Gross} = \frac{\text{IVC (°BTDC)} + \text{EVO (°ATDC)}}{CAM \text{ Resolution}} \tag{5}$$

where *IVC* is the intake valve closing timing (in °BTDC) and *EVO* is the exhaust valve opening timing (in CA° ATDC). The indicated performance parameters are effectively defined as the number of elements

measured during compression, combustion, and expansion strokes [34]. The *Gross Combustion Duration* (saved locally in the program as Gross Index) value is used in the rectangular rule loop to calculate the indicated gross parameters (Frame 6).

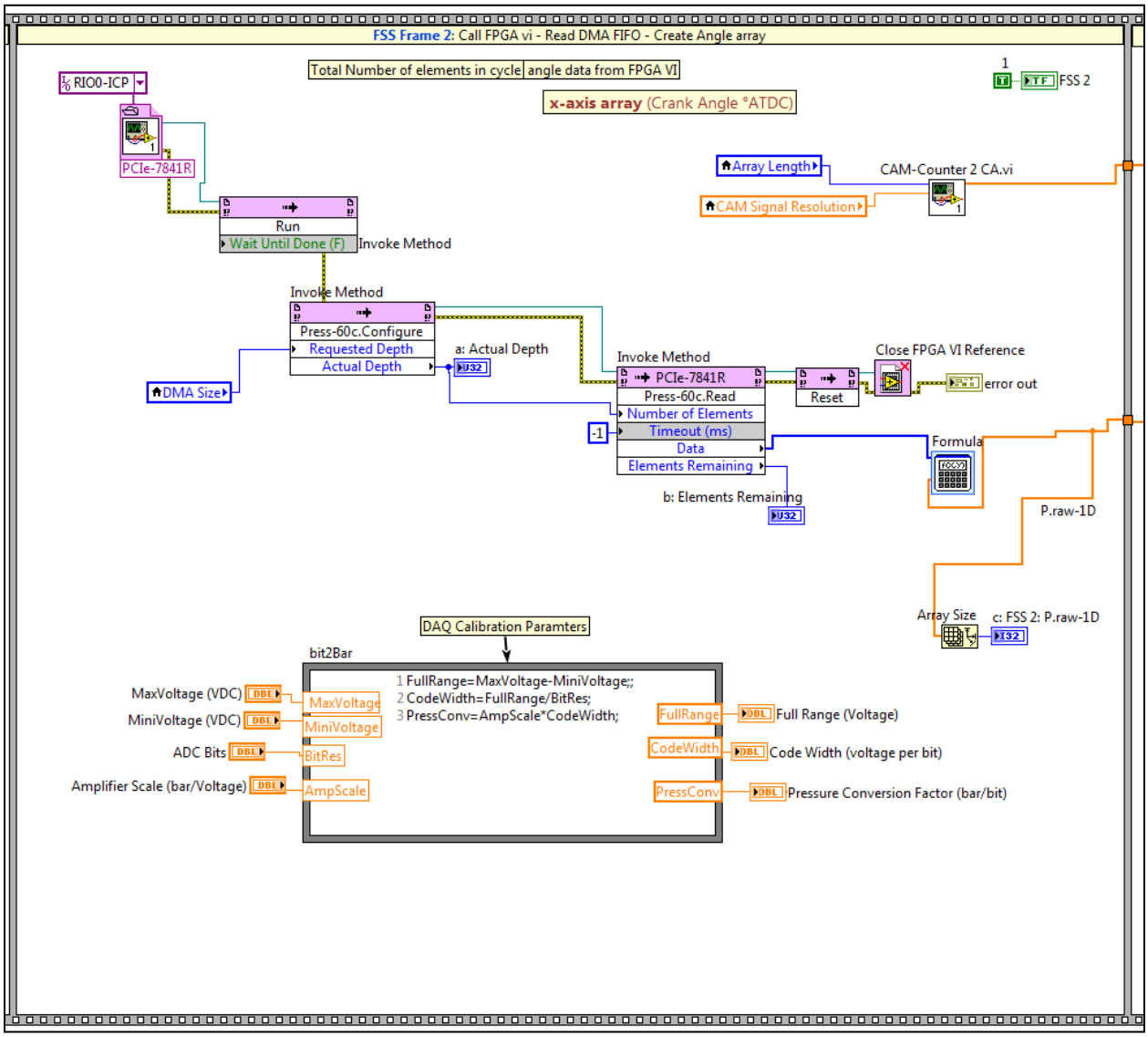

Figure 18: ICP Host VI Block Diagram: Frame 2: Call FPGA VI and Read Pressure DMA

2. **Frame 2 (Invoke FPGA VI and Pressure DMA)**: In this frame (Figure 18), the FPGA VI is invoked and all the elements in the DMA FIFO are read. The number of elements imported from the FIFO is equal to the DMA Size calculated in Frame 1. Moreover, DAQ Calibration Parameter inputs from the front panel are used to convert the raw pressure reading into useful pressure values.

Specifically, raw pressure data as represented in 16-bit resolution integers (word signed integer) are converted to pressure values in units of bar as follows:

$$\text{Pressure Conversion Factor}\left(\frac{\text{bar}}{\text{bit}}\right)=\text{Amplifier Scale}\left(\frac{\text{bar}}{\text{V}_{\text{DC}}}\right)\times\text{Code Width}\left(\frac{\text{V}_{\text{DC}}}{\text{bit}}\right) \quad (6)$$

where the *Pressure Conversion Factor* is a unique cumulative value, the *Amplifier Scale* (in bar per V_{DC}) is a configurable gain value for Kistler hardware (mentioned in Table 1).

$$Code\ Width\left(\frac{V_{DC}}{bit}\right)=\frac{Voltage\ Input\ Range}{2^{ADC\ Resolution}} \quad (7)$$

where the *Code Width* (in V_{DC} per bit) is the smallest analog voltage change (i.e., pressure signal) that the sink device can detect and represent digitally in bits, the *Voltage Input Range* is the configurable peak-to-peak voltage span that sink device can acquire, and *ADC Resolution* is the total number of bits used to represent the analog voltage signal. The input device range is configurable via the PCIe settings while *ADC Resolution* is determined by data type in the DMA FIFO (16-bit). The parameterization of the conversion factors individually for each device in the system is of great importance for troubleshooting the DAQ system. Specifically, by calculating the conversion parameter for each components of the system, the plausibility of three signals can be verified independently using an oscilloscope. Indeed, during the initial troubleshooting process, a malfunction in the charge amplifier was detected by displaying the voltage output on oscilloscope. Hence, the Kistler charge amplifier has since been repaired and recalibrated by the manufacturer.

Additionally, the indices of the pressure signal are converted to degrees of Crank Angle (°CA) using the following arithmetic progression:

$$\text{CA° Array} = \{\theta_0,\theta_1,\ldots,\theta_i,\ldots,\theta_{n-1}\} \quad (8)$$

where *CA° Array* is the dataset that contains x-axis domain, θ_0 is lower limit of the CA Sampling Window, θ_{n-1} is the upper limit of the CA sampling window, *n* is the array length.

$$\theta_i=\theta_0+(i-1)\times CAM\ Resolution \quad (9)$$

where θ_i is the element angle value, calculated using the index number (*i*) and the CAM resolution.

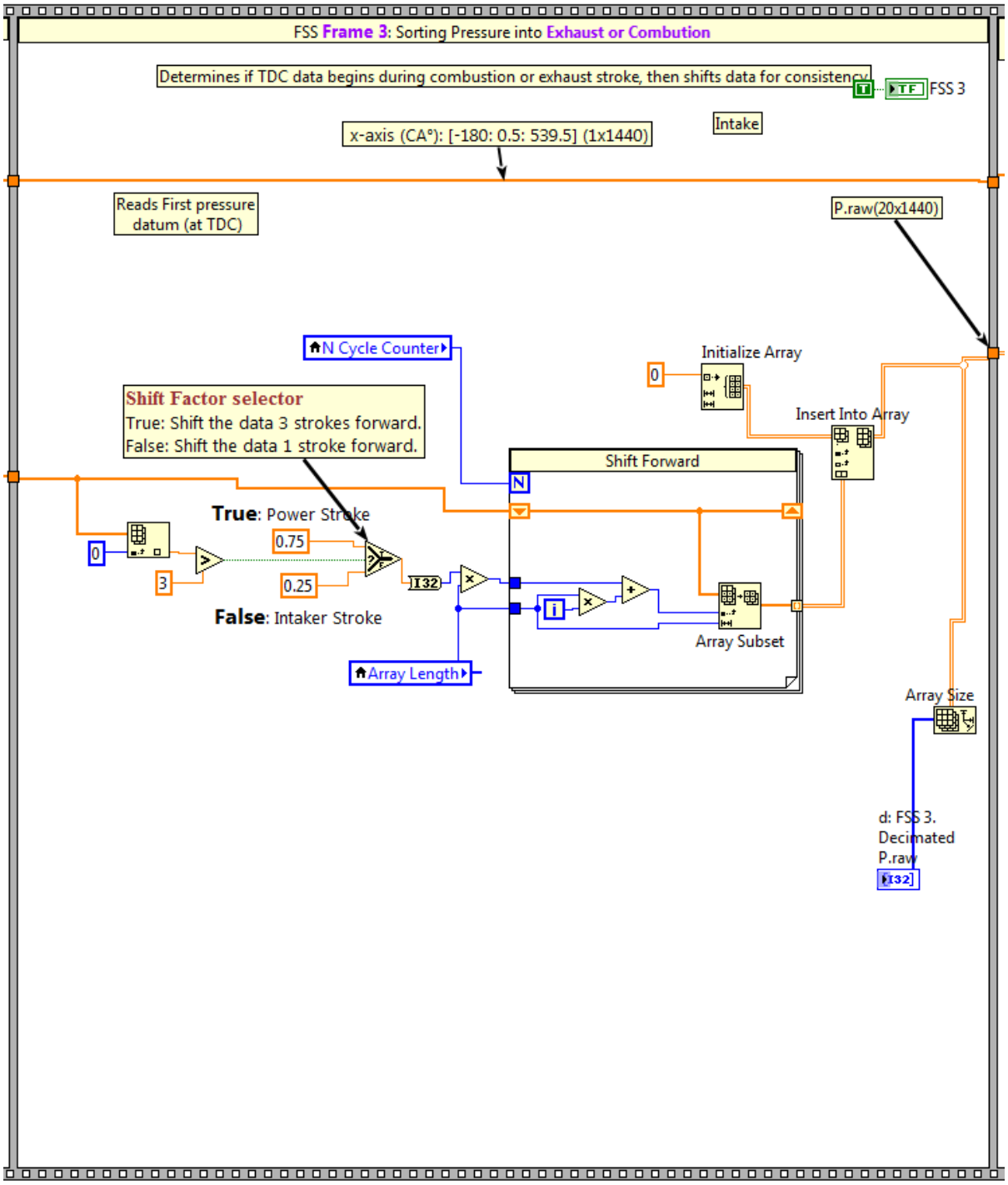

Figure 19: ICP Host VI: Frame 3: Organizing the Raw Data Structure

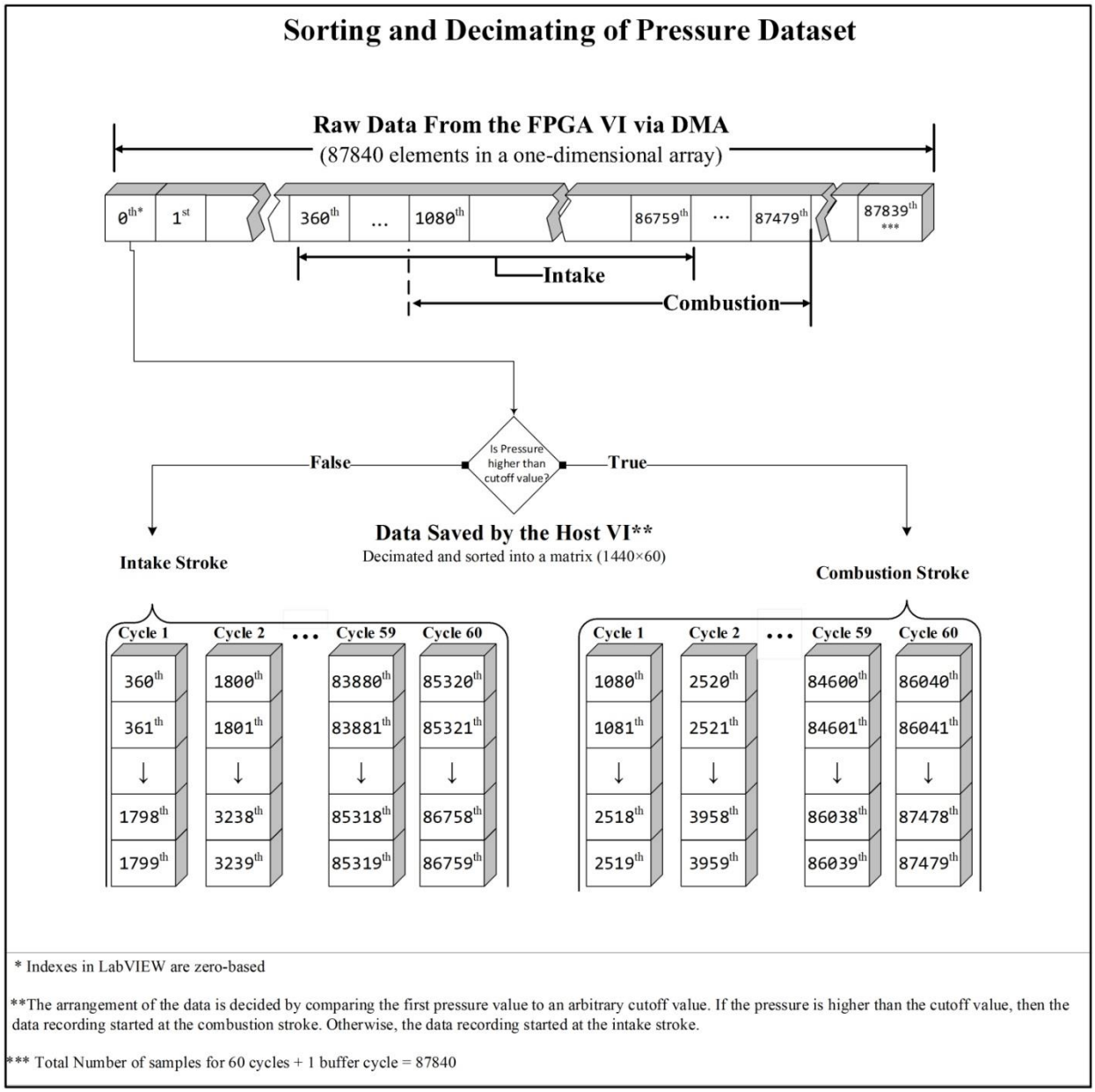

Figure 20: Demonstration of the Data Structure (Sorting and Array) in Frame 3

3. **Frame 3 (Organizing the Data Structure):** This frame (Figure 19) is designated for changing the raw data structure from a one-dimensional array (1D×87840 elements) into a 2-D array of N_{Host} number of columns and N_{Array} number of rows. Specifically, the acquired raw data array is indexed to the crank angle array such that the zero crank angle point is aligned with the TDC location. In order to determine if data sampling has started in the exhaust or combustion stroke, the first element of the data set is read and compared to an approximate cutoff pressure value (i.e., 3 bar). The comparison function is then used to select the *Trimming Factor* such that:

$$Trimming\ Factor = \begin{cases} 0.75, & if\ True\ (Power\ Stroke) \\ 0.25, & if\ False\ (Exhaust\ Stroke) \end{cases} \quad (10)$$

$$Sorting\ Index = Trimming\ Factor \times Array\ Length \quad (11)$$

where *Sorting Index* is the number of elements at which the data sorting begins, and the *Trimming Factor* is the fraction of the raw data (i.e., the buffer cycle) that is trimmed from the first engine cycle. Subsequently, if the measurement is initialized by TDC at the power stroke, the first three strokes (three quarters of a cycle) are discarded. On the other hand, if the measurement is initialized by TDC of the intake stroke, then the first stroke (one quarter of a cycle) is discarded. Subsequently, the pressure data are sorted in the For Loop into a 2-D array of N_{Array} number of columns and 1440-rows. The process of sorting and decimating the saved pressure data is demonstrated in Figure 20.

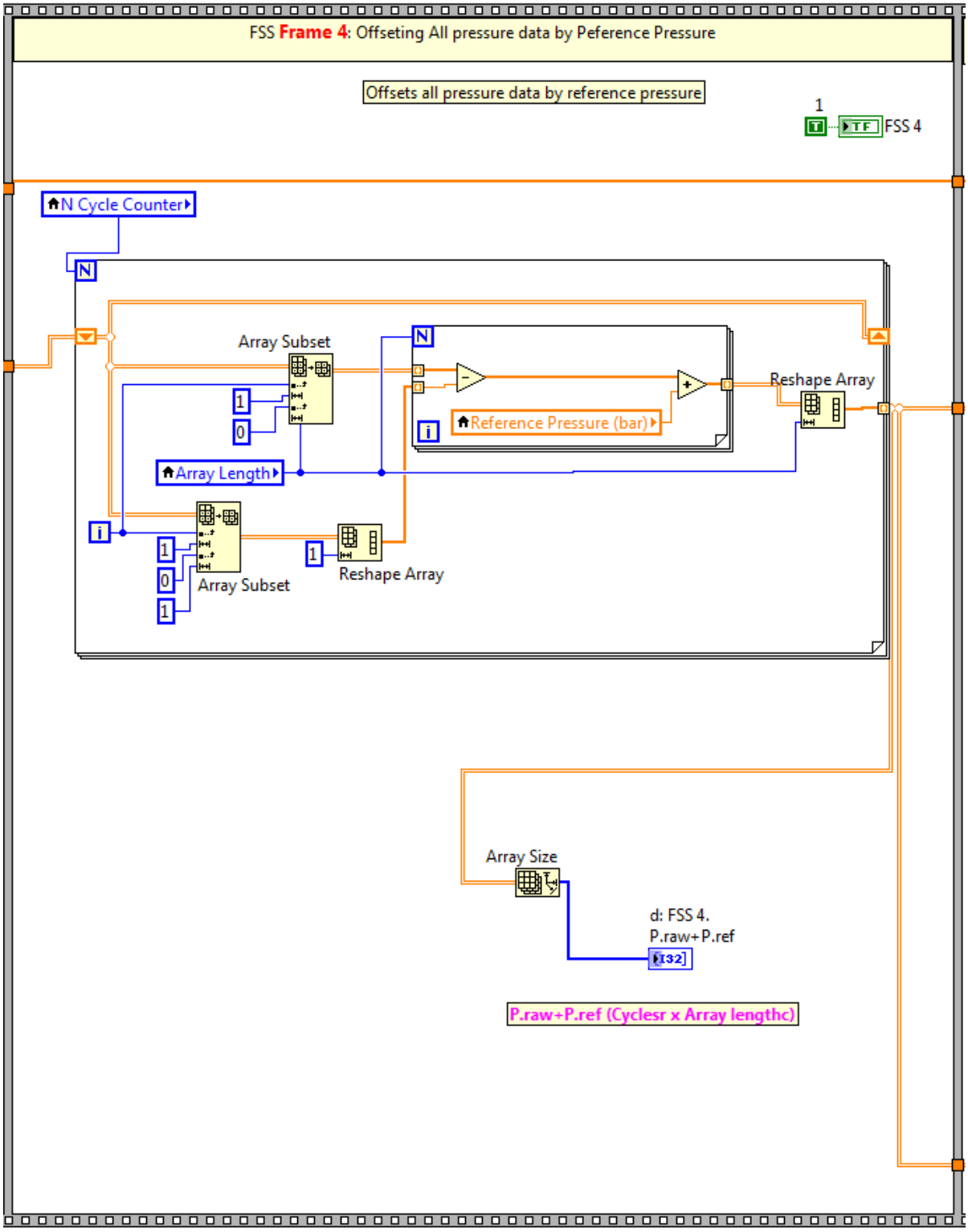

Figure 21: ICP Host VI: Frame 4: Pegging Reference Pressure

4. **Frame 4 (Pressure Pegging):** This frame (Figure 21) is used for pegging the measured pressure signal to a known absolute pressure in order to eliminate a long-term drift, an inherent effect that the piezoelectric transducer exhibits. Specifically, the signaling mechanism of the piezoelectric transducer

(charge output) requires that the measured signal to be referenced to a known voltage at some point in the cycle [35, 36]. Therefore, this process is accomplished by offsetting the pressure data by the reference data with the intake manifold pressure used as the reference pressure.

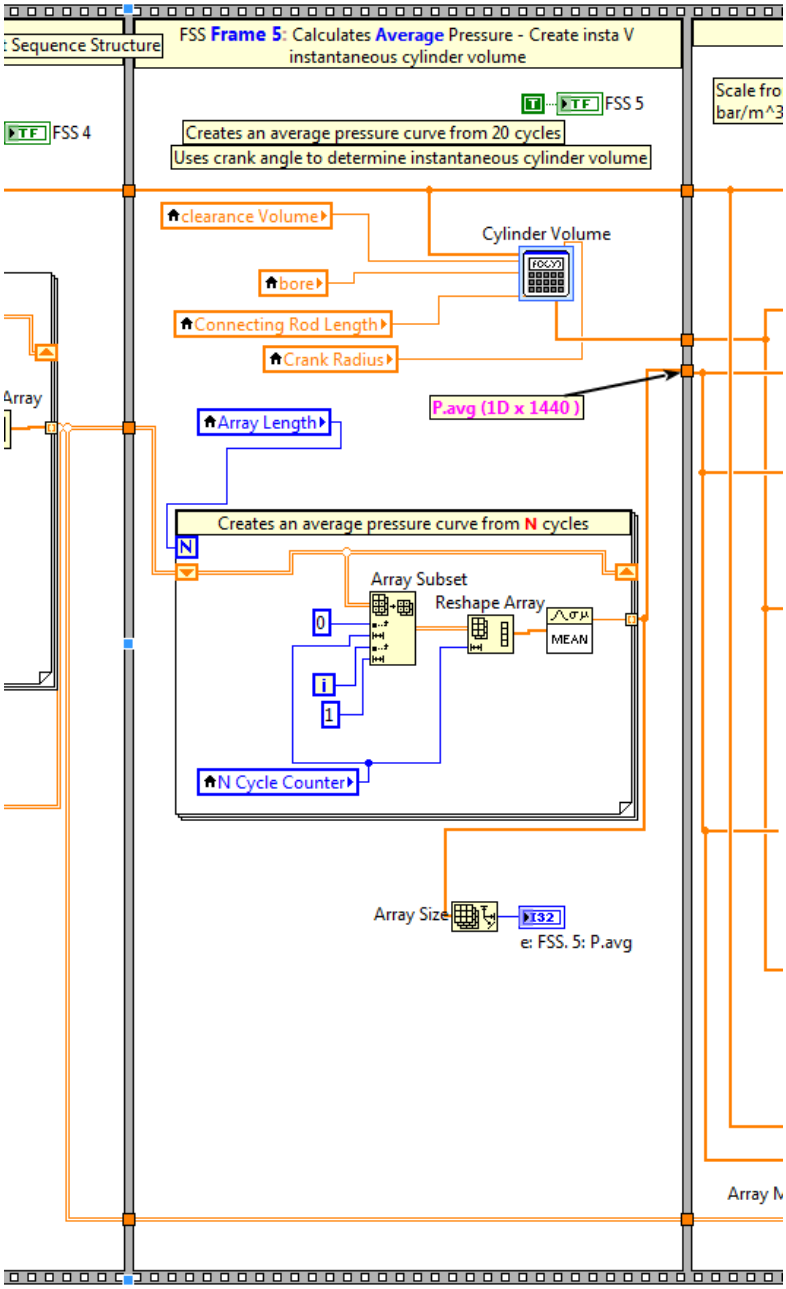

Figure 22: ICP Host VI: Frame 5: Calculating Average Pressure and Instantaneous Cylinder Volume

5. **Frame 5 (Pressure Average)**: Next in Figure 22, the average pressure for the raw data is calculated. Additionally, using the engine geometry parameters inputs, the instantaneous cylinder volume , *V(θ)*, is determined as following:

$$V(\theta) = V_c + \frac{\pi b^2}{4}\left[l + a - x(\theta)\right] \tag{12}$$

where V_c is the clearance volume, b is the cylinder bore, l is the connecting rod length, a is the crank radius, θ is the crank angle, and $x(\theta)$ is the distance between the crank axis and the piston pin axis, which is calculated as:

$$x(\theta) = a\cos(\theta) + \sqrt{l^2 - a^2\sin^2(\theta)} \tag{13}$$

Hence, the instantaneous cylinder volume is calculated as:

$$V(\theta) = V_c + \frac{\pi b^2}{4}\left(l + a - \left\{a\cos(\theta) + \sqrt{l^2 - a^2\sin^2(\theta)}\right\}\right) \tag{14}$$

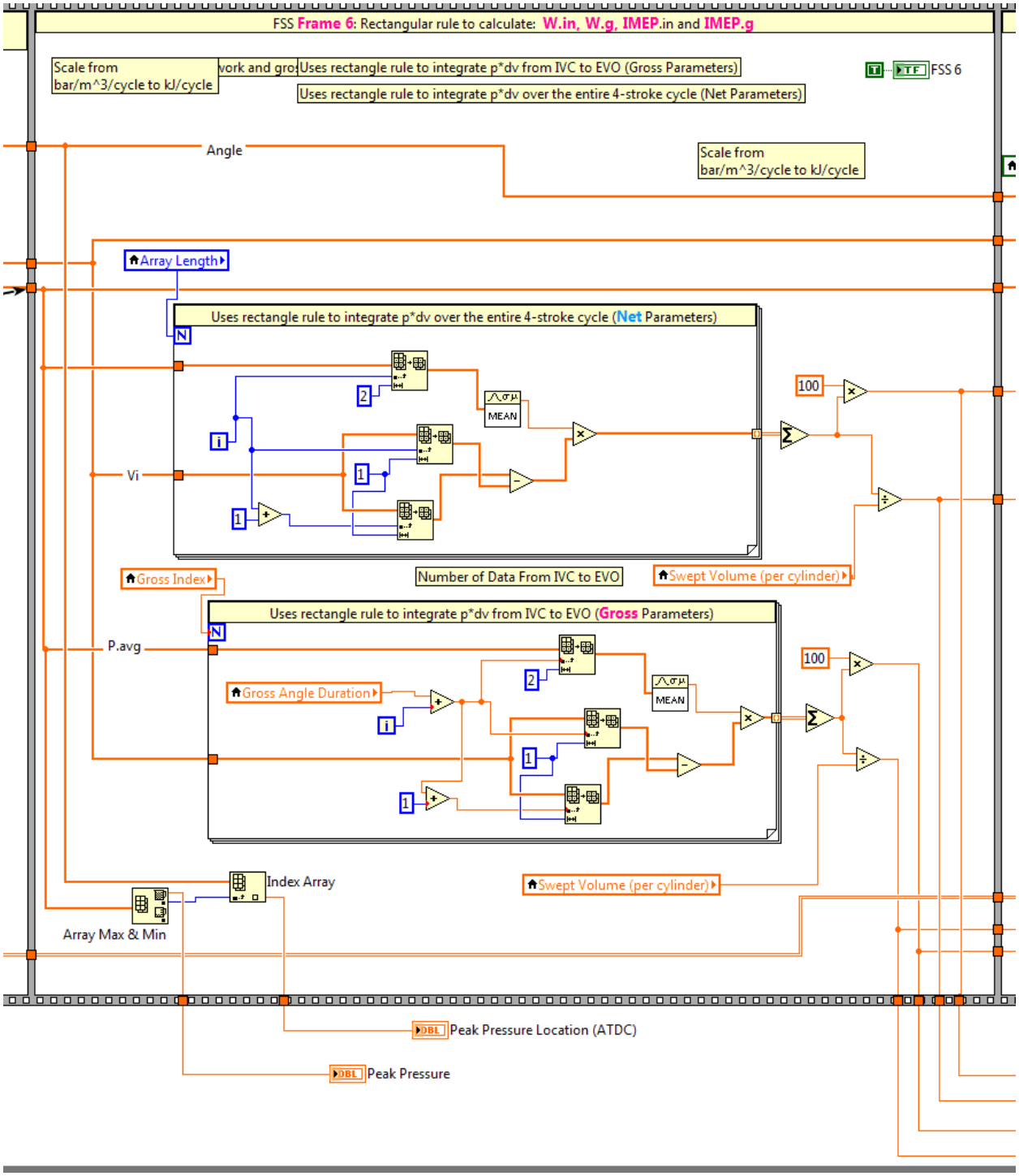

Figure 23: ICP Host VI: Frame 6: Calculating Indicated Performance Parameters

6. **Frame 6 (Performance Parameters)**: In Frame 6 via Figure 23, the rectangular rule is used to calculate the indicated performance parameters for the average pressure: gross indicated work (W_{ig}), net indicated work (W_{in}), gross indicated mean effective pressure ($IMEP_g$), and net indicated mean

effective pressure ($IMEP_n$). Additionally, the peak pressure (bar) and the location of peak pressure (°ATDC) of the average pressure are found.

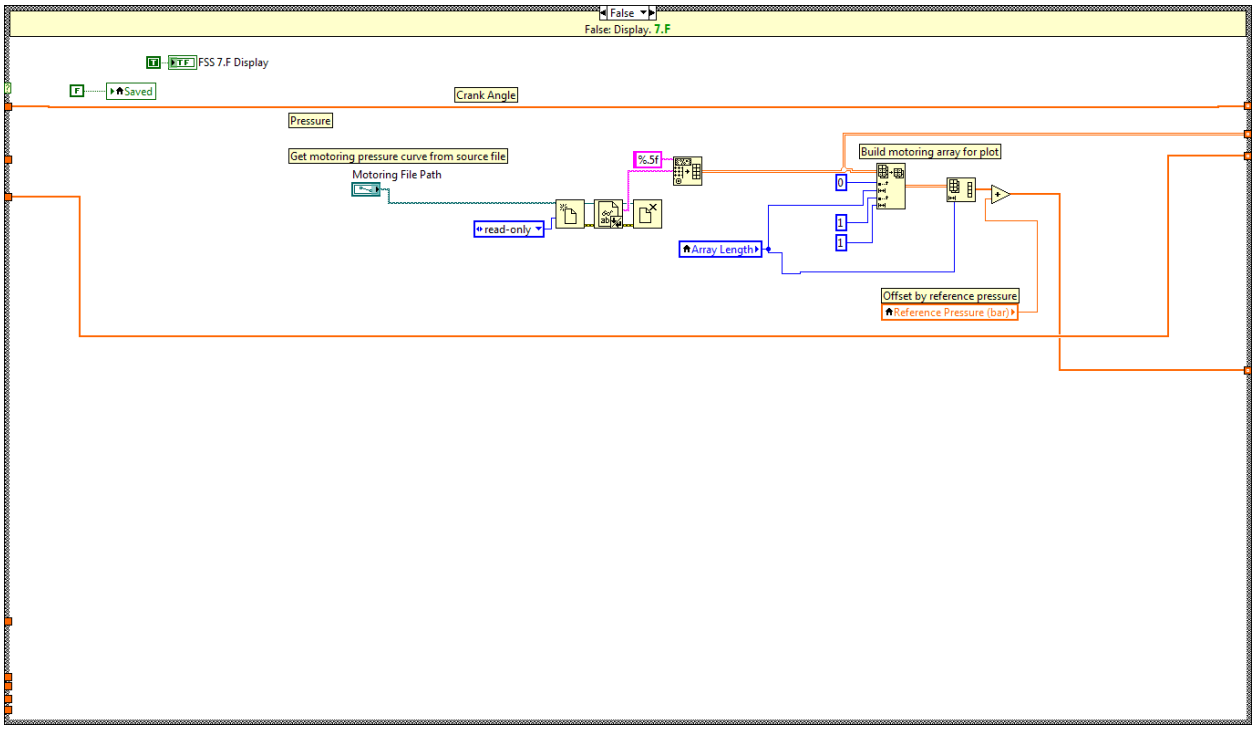

Figure 24: ICP Host VI: Frame 7-False (Display Pressure)

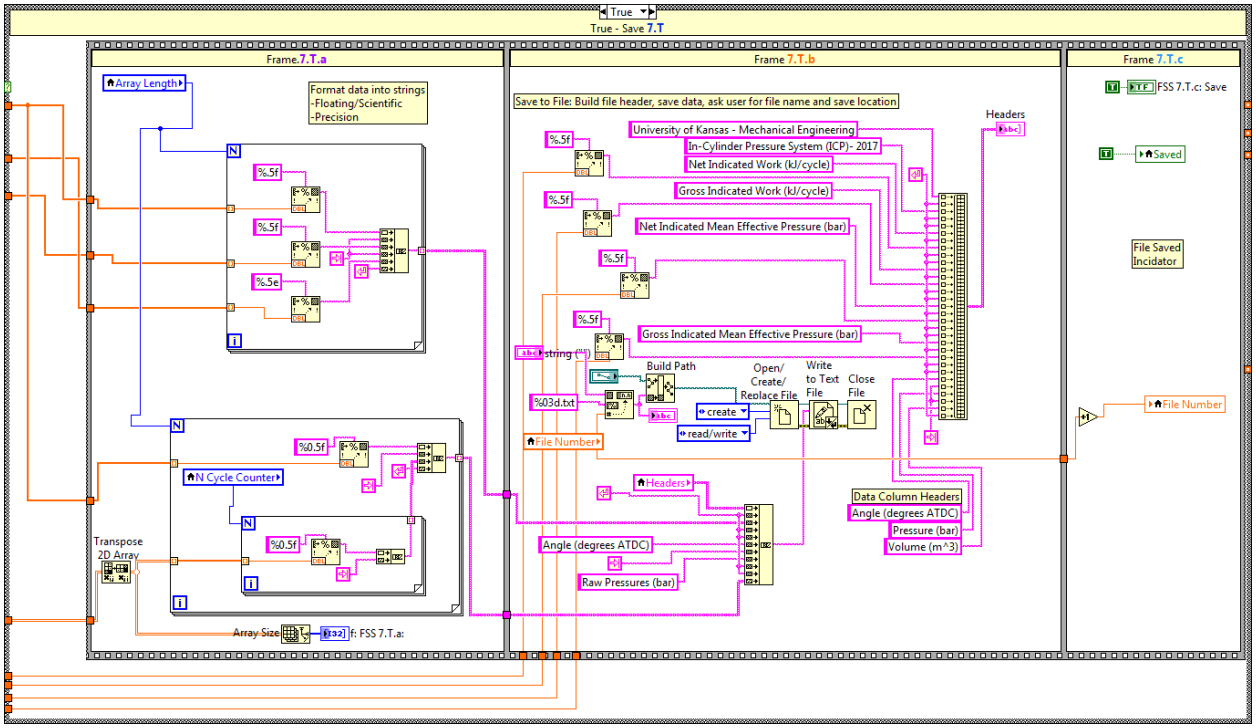

Figure 25: ICP Host VI: Frame 7-True (Record Pressure)

7. **Frame 7 (Plot or Save Pressure):** Next, Frame 7 includes two sub-diagrams for either displaying or recording the in-cylinder pressure. Specifically, the Boolean value of the record control button is used to select between the following case structures:

   a. **Frame 7. False (Display):** In the display mode (Figure 24), the average pressure and the motoring pressure are plotted on the front panel graph. Additionally, the peak pressure (in bar) and the location of peak pressure (LPP, in °ATDC) are displayed on the Front Panel of the Host VI.

   b. **Frame 7. True (Record)**: On the other hand, in the recording mode (Figure 25), the raw pressure, average pressure, and indicated performance parameters are saved to as a text file.

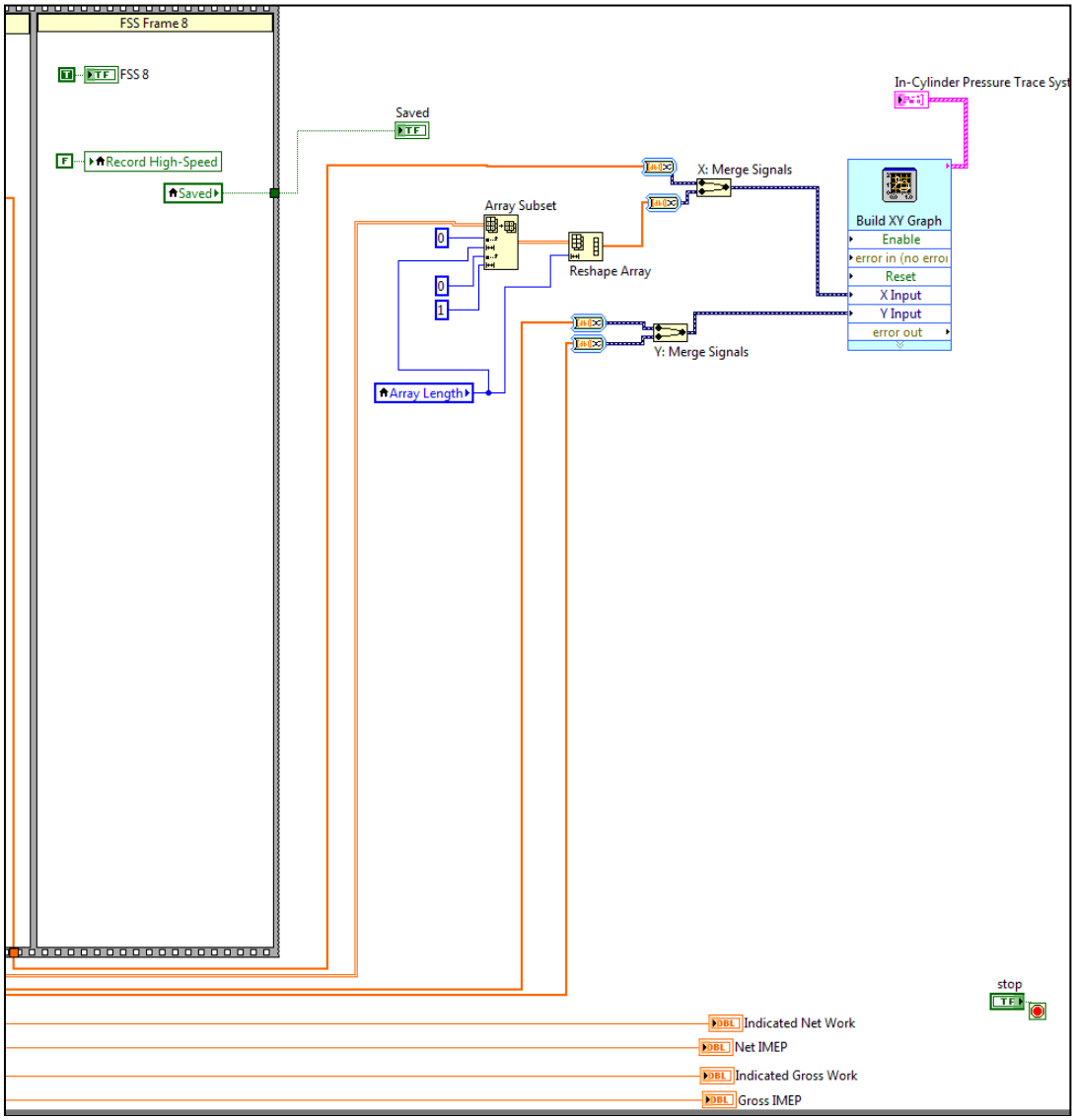

Figure 26: ICP Host VI: Frame 8: Terminate Loop, Export Outputs, Reset Save Command, and

Graph Average Pressure

8. **Frame 8 (Reset Loop)**: In the last frame (Figure 26), the Record control button is reset to its default value (false). Additionally, the numerical file name for the auto save function is incremented. Finally, at the end of Frame 8, the Host VI restarts from Frame 1.

2.4 Standalone Systems Fuel Control Measurement (Lambda)

The fuel control system is accompanied with a relative Air-Fuel Ratio Feedback signal, known as Engine lambda (λ):

$$\lambda = \frac{(A/F)_{actual}}{(A/F)_{stoich.}} \tag{15}$$

where $(A/F)_{actual}$ is the measured Air-Fuel Ratio, and $(A/F)_{\text{stoich}}$ is the stoichiometric Air-Fuel Ratio. The lambda system was installed in the exhaust line of the engine, providing a direct measurement of the oxygen content of the exhaust gas. The system consists of a Wideband lambda sensor (Bosch LSU 4.9) and lambda controller (Tech Edge - WBo2 2C0B) that provides an external voltage source for the lambda sensor. Additionally, the lambda controller utilizes a programmable look-up table based on a specified post-reformer fuel input (i.e., pure propane).

2.5 Conclusions

The setup of the Syngas Rig in the new location introduced several challenges, creating opportunities to improve the safety and operability of the Syngas Rig while resolving these challenges. Additionally, the increased complexity of the control system due to the automation of the fuel system necessitated the implementation of fail-safe measures to protect against potential catastrophic damages in critical components of the system (e.g., engine overheating, fuel leak, etc.). Specifically, the reconfiguring of the manual and digital relays that control the fuel, from a parallel circuit to a series circuit, introduced a redundancy in the new setup in order to resolve the latching effect the fuel system solenoids encounter when a connection to the primary DAQ is lost, hence, eliminating any unintentional activation of the fuel system.

Furthermore, new components were added to the Syngas Rig to assist the automation of fuel control. For instance, after installing the new EFV, the stalling of the engine caused a pressure fluctuation in the intake system, which was resolved by employing a vacuum control solenoid (VCS) to accompany the EFV operation in the fuel system. The VCS is used for gating the fuel flow using the vacuum signal from the engine intake as the fuel flow is primarily driven by engine vacuum as detailed in Chapter 3. Additionally, the installation of an electric water pump resolved an engine overheating issue.

Moreover, as some components of the system were replaced, several calibration procedures were performed. For instance, the installation of a new harmonic balancer required the relocating and marking of the TDC positions on the harmonic balancer. The TDC determination procedures were performed for the first cylinder in order to be used as the base for the initial spark timing. Similarly, the TDC position of the third cylinder was located in order to be used as the trigger signal for the ICP system.

Due to the unsuccessful attempts to deploy the previous ICP program, a new program was developed in order to address the issues encountered in the signal waveform. A comprehensive description of the ICP system is included in this chapter as a troubleshooting guide to help identify any sources of error (e.g., signal waveform, software bug, or hardware malfunction). Due to the uniqueness and complexity of the ICP system, debugging tools were embedded into the new program. For instance, the data flow of the ICP program can by verified using the progress indicators on the front panels of the FPGA VI and the Host VI, validating the sequential execution of subdiagrams.

Additionally, the parameterization of conversion factors for each device increased the modularity of the program while assisting in detecting any malfunctioning device. Subsequently, the system proved successful in acquiring in-cylinder pressure measurements. Hence, the new ICP program resolved a signal jitter issue while increasing the throughput of the data (i.e., total number of measured engine cycles).

The implementation of these upgrades alleviated problems created through the relocation of the Syngas Rig while improving its operation and efficiency. Furthermore, the description of this process and its challenges as described in this chapter can be used as a guide for any further upgrades of the DAQ system as necessary.

Chapter III: Fuel and Spark Control of Propane for a PFI SI Engine

This chapter has been accepted as a technical paper for the 2018 SAE World Congress Experience as: "Fuel Control and Spark Optimization of a Propane Fuel System for an Engine-Generator System," by K. AlZeeby, and C. Depcik, 10-12 April 2018, Detroit, MI (SAE Paper 2018-01-1141)

3.1 Abstract

As climate change drives the exploration into new and alternative fuels, biodiesel has emerged as a promising alternative to traditional diesel fuel. To further increase the viability of biodiesel, a unique system at the University of Kansas utilizes glycerin, the primary byproduct of biodiesel production, for power generation. This system converts glycerin into a hydrogen-rich gas (syngas) that is sent to an engine-generator system in one continuous flow process. The current setup allows for running the engine-generator system on pure propane, reformed propane, or reformed glycerin, with each fuel serving a unique purpose. This chapter discusses upgrades in pure propane operation that serves the intent of preheating the engine prior to syngas operation and establishing the baseline energy requirement for fueling the system. The current upgrade to the fuel system incorporates an electric fuel valve (EFV) as a replacement for a gaseous propane carburetor, providing the ability for air-to-fuel ratio (AFR) adjustment of the engine at different generator loads. The use of EFV in a continuous fuel additive manner provides a solution to the carburetor's inherent disadvantage: maintaining a constant AFR. Hence, this upgrade allows the system to adjust more accurately to different engine operating conditions and other unique fuels to be potentially tested (e.g., natural gas and biogas). Moreover, spark timing optimization accompanies the new fuel control in order to enhance engine performance and maximize fuel economy. Finally, in-cylinder pressure traces and associated performance parameters are reviewed and discussed in order to analyze the operation of the new EFV-based system.

3.2 Introduction

Biodiesel is a feasible alternative to fossil fuels and often enters the research spotlight whenever the crude oil market experiences price fluctuations. Furthermore, the ability to produce biodiesel domestically can reduce the United States dependency on foreign oil. In this area, many manufacturers now allow for their compression ignition (CI) engines to utilize up to 20% biodiesel blends, with no adjustments needed, without incurring a significant performance degradation with the benefit of lowering emissions of particulate matter (PM), hydrocarbons (HC), and carbon monoxide (CO) [1, 2]. Moreover, after normalization of the combustion process, the use of biodiesel blends can potentially lower emissions of nitrogen oxides (NO_x) [37].

With respect to the production of biodiesel, glycerin is an important byproduct (10% weight of biodiesel) that is commonly used in manufacturing consumer products (e.g., food, soap, pharmaceuticals, etc.). As biodiesel production has grown to a volume of 1.556 billion gallons in 2016 [38], the abundant generation of glycerin results in an economic challenge for the biodiesel industry. Moreover, the storing of unused glycerin inflicts a logistical difficulty for biodiesel manufacturing facilities, subsequently turning glycerin into a waste management problem [4, 39, 40]. As a result, a unique reformation and combustion system (aka Syngas Rig) at the University of Kansas (KU) takes advantage of this abundance of glycerin (and its embedded hydrogen) by using it as a fuel. In specific, reformation of glycerin over a nickel catalyst creates a hydrogen-rich synthesis gas (syngas) that flows to an engine-generator setup to create power [12]. The current system utilizes multiple pathways that allow for running the engine on any of the following three fuels: pure propane, reformed propane, or reformed glycerin, with each operational pathway serving a specific purpose [41]. In particular, pure propane (PP) operation provides the baseline energy requirement for the engine at different load points for subsequent matching by the two reformate fuels. Furthermore, another use of PP is to preheat the reformer in order to initiate the exothermic catalytic reactions of propane and glycerin reforming. However, previous efforts utilized a gaseous carburetor for the PP pathway resulting in an inability of the system to employ closed loop feedback.

In regards to upgrading the system for enhanced control, reviewing the literature finds a wide range of methods for utilizing gaseous fuels. For instance, Das et al. evaluated mixture formation methodologies for hydrogen and Compressed Natural Gas (CNG) in SI engines. Their studies included continuous carburetion, continuous manifold injection, timed manifold injection, and low-pressure direct cylinder injection. Specific to this chapter, carburetion and continuous manifold injection were found to increase the intensity and frequency of backfiring, particularly for hydrogen [42, 43]. Furthermore, while gaseous fuels have the potential to increase thermal efficiency while potentially lowering NO_x emissions, inducting into the intake lowers volumetric efficiency by displacing air. Hence, researchers are developing specialized high-pressure gaseous injectors (8 MPa or higher) that enable the usage of specific gaseous fuels for direct injection SI and CI engines (e.g., CNG [44-46]). However, the overall concept of the fueling system for the Syngas Rig is to operate on a variety of gaseous fuels, such as biogas, and even ammonia [47, 48]. As a result, this effort describes the implementation of a new conduit that utilizes an electric fuel valve (EFV). The EFV allows for finer control of the fuel flow rate (either manual or automatic) in comparison to the carburetor when operating the engine at different loads. Therefore, implementation of the EFV will allow the system to utilize other future fuels more efficiently.

Furthermore, since the prior efforts found that running the engine on reformed glycerin through the carburetor resulted in rich equivalence ratios around 1.6 [41], another goal is to maximize combustion efficacy of unknown fuels through operation at lean air-to-fuel ratios (AFRs). By operating lean, optimum conversion of the fuels can take place without other engine operating conditions significantly impacting the outcomes [34]. Moreover, a lean mixture is generally favorable as it minimizes the engine's exhaust emissions of CO and HC while enhancing thermal efficiency. However, operating an SI engine too lean can result in erratic behavior, such as misfire and cyclic variations, accompanied by a loss of power and rapid growth in exhaust HC emissions [49]. In addition, to ensure maximum thermal efficiency, spark timing must also change with the mixture entering the engine. This adjustment should account for the fuel constituency and when running lean because ignition lag grows in this scenario [50]. This adjustment was

not possible in the prior work due to the use of a mechanical spark advance system. Hence, this work additionally describes an upgrade to engine control using an aftermarket system.

As a result, this chapter first describes the revised experimental setup including associated figures in the Appendix. Then, an explanation of the updated electronic spark control is provided to set the stage for the results and a discussion of spark sweep tests running PP at different AFRs in order to achieve maximum brake torque (MBT) timing. Overall, researchers can use the information provided to accomplish similar efforts in the creation of a gaseous fuel flexible testing system.

3.3 Experimental Procedures/Apparatus

The engine is a naturally aspirated small block spark-ignited (SI) Chevy (5.7 liter) that runs at a constant speed of 1800 rpm. Connected to the flywheel of this engine is a power-take-off generator (Mecc Alte ECO32-2L/4 alternator) that is synchronized and controlled by a Woodward Genset Control (GCP-20) that provides two 240 VAC, 50 A power outlets acting as loading points. Engine speed is controlled by a Woodward LC-50 throttle valve (TV) that maintains a constant rotary speed of 1800 rpm corresponding to the rated frequency of the generator (60 Hz) [51]. The TV is self-contained and operates in a closed loop by opening and closing in accordance to a feedback signal from the ignition module that indicates the engine's instantaneous speed. Initially, PP operation of the Syngas Rig utilized an independent gaseous-fuel system consisting of a vacuum fuelock filter (VFF – IMPCOVFF30), a two-stage regulator (IMPCO G-JB-2), and a carburetor, respectively. As a result, fuel-air mixtures were controlled mechanically via a power adjustment screw in the carburetor assembly. However, this tuning is only effective when the engine is operating at full-load or at the rated speed limit [52]. Another disadvantage of this method is the inability to tailor the fuel system for various engine operation and/or when employing different fuels [53]. Moreover, this relatively conventional carburetor does not account for ambient conditions when setting the AFR. For example, a carburetor that is calibrated for summer may not be suitable for winter condition [54]. This is a specific problem for the KU setup since the Syngas Rig operates in an outdoor enclosure.

As a result, another fuel control method was needed to dynamically monitor and control the AFR. Specifically, new components were installed in order to accommodate automatic fuel control and a current listing of the components is as follows with Figure 2 providing an illustration of the existing setup:

1. LPG Vacuum Fuelock Filter (IMPCO Technologies,VFF30): a combination of fuel lockoff and filter. Moreover, a vacuum-control solenoid is used to activate the lockoff. When the engine is running, a vacuum is directed to this unit to allow the propane to flow through the filter.
2. LPG Two-stage Regulator (IMPCO Technologies, G-JB-2): a fuel regulator that includes a heat exchanger. Water from the engine coolant system is circulated through the heat exchanger in order to assist in vaporization of the propane. The regulator is activated by the vacuum signal from the TV when the engine is running or cranking (i.e., turning over).
3. Shuttle Valve (OMEGA, SV251): a three-way valve with two inlets and one outlet. The valve acts via an "or" logic to allow flow to the outlet from either of the two inlets. In other words, this valve switches between PP and syngas.
4. Electric Fuel Valve (EFV- Assured Automation, EV1S1V1): a bi-directional valve, actuated electrically by the on-board relays as explained later. This valve enables dynamic fuel metering to the Syngas Rig.
5. LPG Carburetor (PNG Technologies, CA55 [52]): a mixer with an air horn is utilized to maintain a constant pressure drop to draw fuel while sending a vacuum signal to the vacuum fuel filter. The carburetor is no longer used for metering the fuel, but rather for simply mixing air and fuel.
6. Throttle Valve (Woodward, LC-50 [51]): an electronic throttle valve that is programmed to operate in a closed-loop in order to maintain engine speed.
7. Vacuum Control Solenoid (VCS – IMPCO, TSB-196): a valve used to direct the vacuum signal to the VFF30 when the propane fuel needs to be activated. The VCS is activated via the Primary Data Acquisition (DAQ) system highlighted in Figure 4.

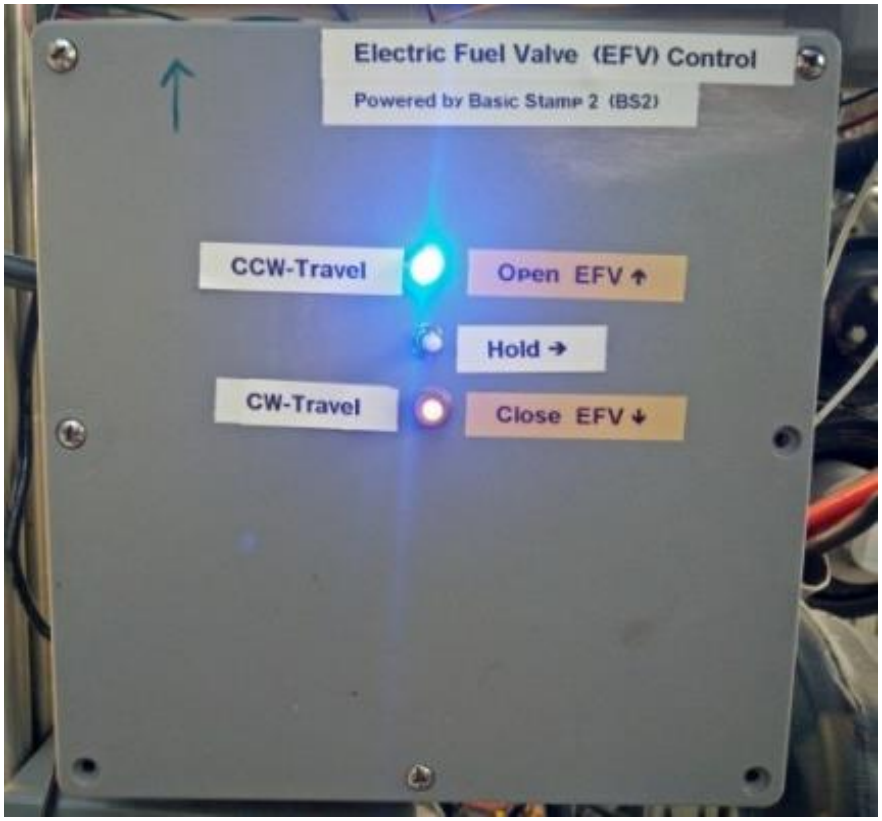

Figure 27: EFV Manual Control Components from the Top: Blue LED Light Used as an Indicator for the Counterclockwise (CCW) Closing Travel; Middle: Three-Position Toggle Switch (Up to Open, Middle to Hold, and Bottom to Close); Bottom: Yellow LED, Used as an Indicator for the Closing Clockwise (CW) Movement.

In the new configuration, the EFV was installed in the fuel line and upstream of the carburetor. This EFV is powered by an internal actuator that open and closes the fuel valve, based on signals received by two internal single-pole, double-throw (SPDT) switches [55]. Following the installation of the new valve, trial-and-error testing concluded that operating the EFV using a discrete signal induced a rapid fuel pressure change, which caused erratic engine behavior (i.e., hunting and surging). Therefore, in order to allow for gradual fuel metering, a dedicated microcontroller (Propeller Board of Education) is used to send a pulse-width modulation (PWM) signal to the EFV's actuator. This microcontroller employs Basic Stamp 2 (BS2) as the programming language with the control schematic provided in Figure 40. The low-level programming of BS2 allows for full control of the microcontroller, helping better optimize the controller and the EFV. In particular, the frequency at which the EFV opens and closes is coordinated directly using the command line: "PULSEOUT PIN, DURATION" where PULSEOUT is the function to

generate a pulse on the PIN specified for the DURATION desired. With respect to BS2 operation, the unit of duration is 2 microseconds (μs).

The command to open or close the EFV is sent to the microcontroller using two methods. The first option is the manual method that uses the three-position SPDT switch shown in Figure 27. This switch can be toggled between opening the EFV (upper position), holding still (middle position), or closing the EFV (lower position). The second method is done programmatically via LabVIEW. In particular, two digital channels from the primary DAQ (Module 7: DIO9 and DIO10 in Figure 40) are connected to the microcontroller, conveying LabVIEW program commands. Moreover, the duty cycle (in the form of an analog signal) at which the EFV rotates can be changed to allow for more rapid closing or opening of the EFV. Hence, this duty cycle can be controlled manually or programmatically via the BS2 microcontroller. During initial testing, a rotary potentiometer was used and it was determined that a pulse width of 14 milliseconds (7000 units) at 20% duty cycle was sufficient to ensure stable EFV control and a steady change of AFR without engine stall or operational instability. A higher duty cycle (i.e., a faster rotation of the EFV) tends to cause an idle surge (fluctuation of engine speed) due to a pressure vacuum wave that interferes with the closed-loop throttle valve operation. The code used by the microcontroller is included in Appendix B.

Additionally, in order to assist in operating the EFV, two 5 mm LED lights (blue and yellow) were installed in the controlling box to act as indicators regarding the status of the EFV (also seen in Figure 27). During normal operation (i.e., EFV is held still), both LED lights are switched on indicating that the microcontroller is working properly and ready for command. However, while opening the EFV, the blue LED flashes while the yellow LED is turned off. Inversely, when the EFV is closing, the yellow LED flashes while the blue LED is turned off. Lastly, if the microcontroller receives conflicting signals simultaneously (e.g., an open signal from LabVIEW and a close signal from the manual switch), the EFV will hold steady and the two LEDs will flash to alert the operator to the conflict error.

In order to monitor the pressure difference created by the EFV, two gauge pressure transducers (OMEGA PXM309) were installed upstream and downstream of the EFV. During automatic control

mode, the measured pressure difference is used as a disturbance indicator. Specifically, when the EFV is closing, the differential pressure across the fuel valve oscillates while the TV is responding to this change in order to maintain the 1800-rpm setpoint. This oscillation is a visual indicator of the stability of the system. Therefore, when these oscillations are deemed minimal (shown later) by reviewing information provided by an exhaust lambda sensor (Bosch LSU 4.9) along with the fuel flow rate, experimental data are taken.

3.4 Data Acquisition and Electronic Spark Control

The DAQ system of the Syngas Rig is divided into two subsystems in Figure 4: Primary and Secondary. For the Primary DAQ, various low frequency sensors are monitored (e.g., thermocouples, pressure transducers, and lambda sensor) and controlled (e.g., flowmeters). The Secondary DAQ oversees a high frequency in-cylinder pressure transducer system that provides the indicated performance parameters of the engine. This system utilizes a Kistler Encoder (Kistler 2614) and a measuring spark plug (Kistler 6118) that provides the pressure signal of the third cylinder at a resolution of 0.5 crank angle (CA) degrees [21]. Using the pressure and CA readings, the average indicated performance parameters are computed (after conversion of CA to volume) using a recorded dataset of 60 cycles.

The in-cylinder pressure trace is used to calculate the net indicated work (W_{in}):

$$W_{in} = W_{ig} + W_p \tag{16}$$

where W_p is the pumping work,

$$W_p = \int_{V_{EVO}}^{V_{IVC}} p \cdot dV \,, \tag{17}$$

and W_{ig} is the indicated gross work per cycle

$$W_{ig} = \int_{V_{IVC}}^{V_{EVO}} p \cdot dV \tag{18}$$

Additionally, the net indicated mean effective pressure ($imep_n$) is calculated using:

$$imep_n = \frac{W_{in}}{V_d} \tag{19}$$

where V_d is the displacement volume of the engine. Next, the net indicated thermal efficiency ($\eta_{t,in}$) is calculated using:

$$\eta_{t,in} = \frac{W_{in} N}{\dot{m}_f Q_{LHV} n_R} \tag{20}$$

where N is the engine rotational speed, $\dot{m}_f$ is the fuel flow rate, Q_{LHV} is the lower heat value of propane (46.4 MJ/kg), and n_R is the number of revolutions in a thermodynamic cycle (n_R = 2 for a four-stroke engine).

3.5 Electronic Spark Timing Control

Previously, spark timing was set mechanically using the standard high energy ignition (HEI), single-point, stock GM ignition system. Besides a mechanical advancement mechanism (i.e., centrifugal and vacuum: $SA_{Mechanical}$), the ignition system had no control over spark timing. Specifically, the engine speed and load were the only operation conditions that determined the spark timing [56]. Hence, the only way to modify timing was to physically rotate the distributor cap, subsequently changing the base (and static) spark timing ($SA_{Initial}$) [16]. Therefore, total spark advance (SA_{Total}) was determined as follows:

$$SA_{Total} = SA_{Initial} + SA_{Mechanical} \tag{21}$$

where

$$SA_{Mechanical} = SA_{Centrifugal} + SA_{Vacuum} \tag{22}$$

Hence, as a result:

$$SA_{Total} = SA_{Initial} + SA_{Centrifugal} + SA_{Vacuum} \tag{23}$$

However, a previous effort involved installing a computer-controlled, single point ignition-system on a similar engine [57]. This was duplicated for the Syngas Rig by replacing the stock engine control module (ECM) with an Embedded Lockers (EBL) system, a reprogrammable ECM developed by DynamicEFI. The EBL system consists of flash memory installed into a stock ECM, enabling it to be fully programmable. Moreover, this component includes eight reprogrammable memory banks, each with its own calibration file, allowing for dynamic change of spark timing without the need to stop the engine.

The calibration file is a binary file that includes all engine parameters used by the ECM, defined as either flags (i.e., on-off switches), scalars (e.g., coolant temperature threshold), or look-up tables (e.g., ignition map, volumetric efficiency map, etc.) [58, 59]. To minimize complexity, only the parameters that pertain to the calculation of spark timing have been enabled. For instance, this module utilizes a magnetic pick-up and manifold absolute pressure (MAP) sensor to provide the engine speed and load, respectively. Hence, the centrifugal and vacuum advance mechanisms were disabled as their functions are currently performed electronically. Appendix D provides a screenshot of the user interface software used for the EBL system.

Table 2: Technical Specification of the Small Block Chevy Engine [57, 60]

Engine Model	Small Block Chevy (LT-9 5.7L V8)
Displacement Volume [cc]	350
Compression ratio	8.2:1
Ignition System	Computer-Controlled, Single Point Distribution system
Crankshaft Arrangement	Cross-Plane (4-throws, 90 ° Ignition Interval)
Firing Order	1-8-4-3-6-5-7-2
Stroke [mm]	88.4
Bore [mm]	101.6
Connecting Rod Length [mm]	144.5
Crank Radius [mm]	44.2
Valves per Cylinder	2
Camshaft Total Lift	0.454”
Intake Duration (at 0.050”)	213°
Exhaust Duration (at 0.050”)	219°
Lobe Separation	112°
Inlet Valve Close (IVC)	142 BTDC
Exhaust Valve Open (EVO)	139° ATDC
Exhaust Valve Close	6° BTDC @ 0.15 mm lift
Inlet Valve Open	2° BTDC @ 0.15 mm lift

Therefore, spark advance (*SA*) can be performed by selecting between the virtual flash memory banks in the EBL system. The new dynamic total spark advance (SA_{Total}) timing is calculated as following:

$$SA_{Total} = SA_{Lookup} - (SA_{ECM} - SA_{Distributor}) \tag{24}$$

where SA_{Lookup} is the spark timing calculated by the ECM using lookup tables as a function engine conditions. The $SA_{Distributor}$ is the physical base initial *SA* set by physically rotating the distributor and is

equal to $SA_{Initial}$ in Eqn. (21). The SA_{ECM} is the spark advance bias used by the ECM to counterbalance the physical *SA*. Therefore, by setting the initial ECM *SA* equal to the physical initial *SA* (i.e., $SA_{Distributor}$), the ECM gains full control of the spark timing. Hence, for the current ECM setup:

$$SA_{Lookup} = SA_{Main} + SA_{ECT} + SA_{IAT} \tag{25}$$

where the SA_{Main} is the main *SA* based on the engine speed (rpm) and load (MAP), and SA_{ECT} and SA_{IAT} are the adjustments based on engine coolant temperature and intake air temperature, respectively. For the experiments that follow, spark timing is controlled by changing the value of SA_{Main} in the calibration file for each sweep

3.6 Knock Detection and Control

Because the system and engine (specifications provided in Table 2) are being designed for the usage of unknown gas mixtures, it is critical to add closed-loop feedback control to remain clear of autoignition (aka knock) combustion regimes. This is accomplished via an electronic spark control (ESC) module that filters the signal picked by a knock sensor mounted to the engine block. Specifically, the ESC module sends a knock count signal to the ECM while other noise signals (e.g., bearing noises, lifters, etc.) are filtered out. A low voltage for this signal is indicative of knock count while normal operation (i.e., absence of knock) is characterized by a high voltage signal (8-12 VDC). Furthermore, when the engine first starts, the ECM tests the validity of the ESC operation by advancing the spark until the first knock count is detected by the ESC module [61].

Knock control is accomplished via one of two modes. For the first model (aka Safe Mode), the *SA* is decreased gradually until the knock signal disappears and can be enabled either permanently or conditionally based on specified threshold parameters (e.g., coolant temperature). The other knock control scheme is the Aggressive Mode at which spark advance is kept at a threshold of knock counts, after which spark timing is delayed until the disappearance of knock. For the experiments described in the next section, the Aggressive Mode was employed in order to allow knock to occur and obtain a full spark sweep.

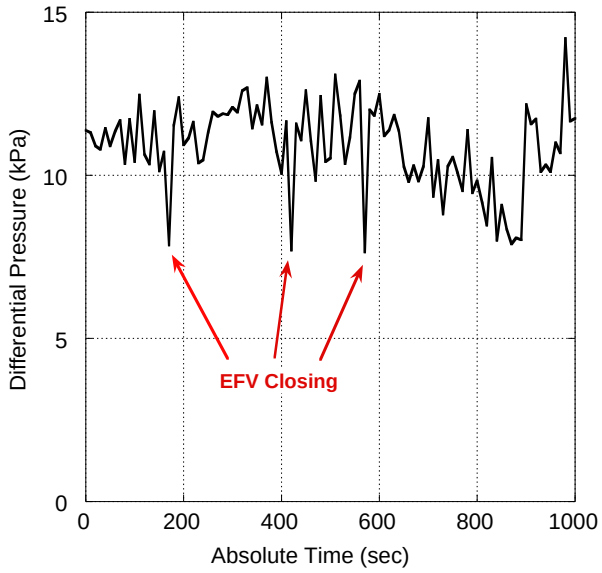

Figure 28: Continuous Recording of the Pressure Difference across the EFV (No Load, 20° BTDC SA)

3.7 Engine Mapping Results and Discussion

In order to analyze the updated setup, the EFV was closed gradually in 10% decrements (~9° EFV rotation) while maintaining constant engine speed and load under steady state flow conditions. This EFV closing was accomplished in order to modulate the operational AFR at three different engine loads using two external heaters (Dayton, 3VU34A) while performing a *SA* sweep in order to find the optimal spark timing. Specifically, the three load points as measured from the generator control unit are 0 kW (no load), ~3.2 kW (one load), and ~6.4 kW (two loads). Steady state was determined by observing the differential pressure across the EFV at each position while the TV adapts to the new change in a closed-loop operation. For example, Figure 28 provides a continuous recording of the EFV position adjustment along with how the differential pressure across this valve changes with operation. At each EFV adjustment, an immediate spike in the differential pressure is seen. While the fluctuations never go away, the second-to-second variation (ideally) becomes relatively consistent. When these variations are deemed small based on experience, data are taken for two minutes and then averaged.

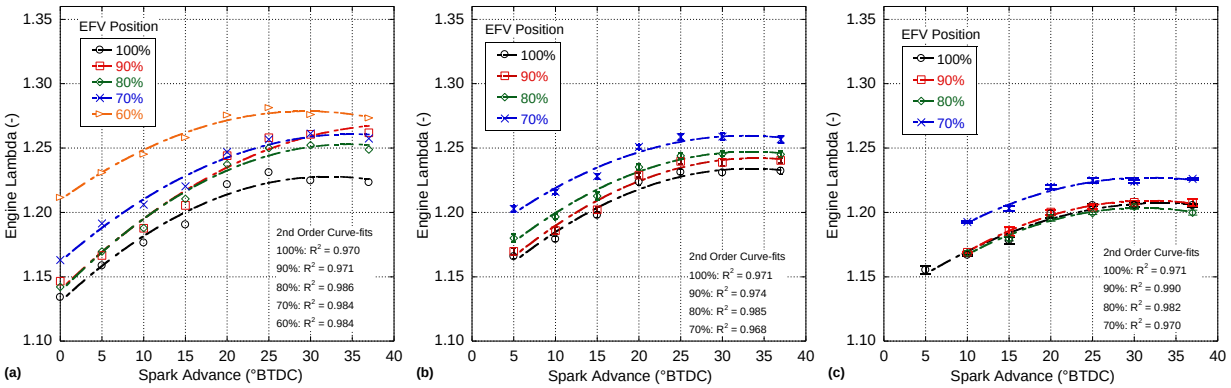

Figure 29: The Lambda Variation for the SA Sweeps Performed while Decreasing the EFV Position at (a) No Load Added, (b) One Load (3.2 kW), and (c) Two Loads (6.4 kW)

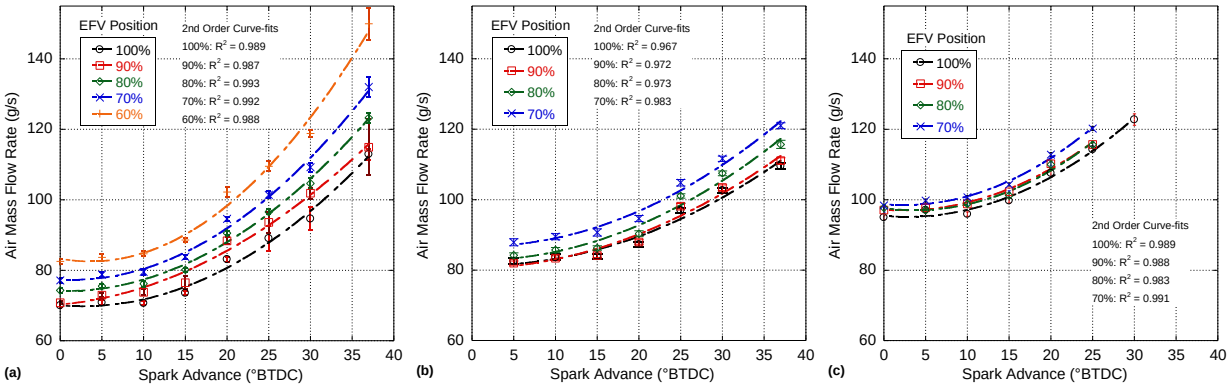

Figure 30: Air Mass Flow Rate for the SA Sweeps Performed While Decreasing the EFV Position at (a) No Load Added, (b) One Load (3.2 kW), and Two Loads (6.4 kW)

For every engine parameter (i.e., load, mixture composition, speed, etc.), there exists a spark timing that yields the maximum engine torque, known as the maximum brake torque (MBT), that is associated the maximum brake power and minimum brake specific fuel consumption [34]. Since this setup will run multiple different gaseous fuels throughout its lifetime, this MBT experimental procedure will become the standard methodology to maximize the potential of each separate gaseous mixture. Of importance, gaseous-fueled engines are typically operated with more aggressive timing curves due to the slower combustion of their fuels [52, 62]. However, increasing the SA grows the intensity of combustion and potential for spark knock [34]. After consultation of the manufacturer's manual [51, 63], a spark timing of 38° BTDC was determined to be the upper limit for SA at which the safe operation of the engine can be maintained.

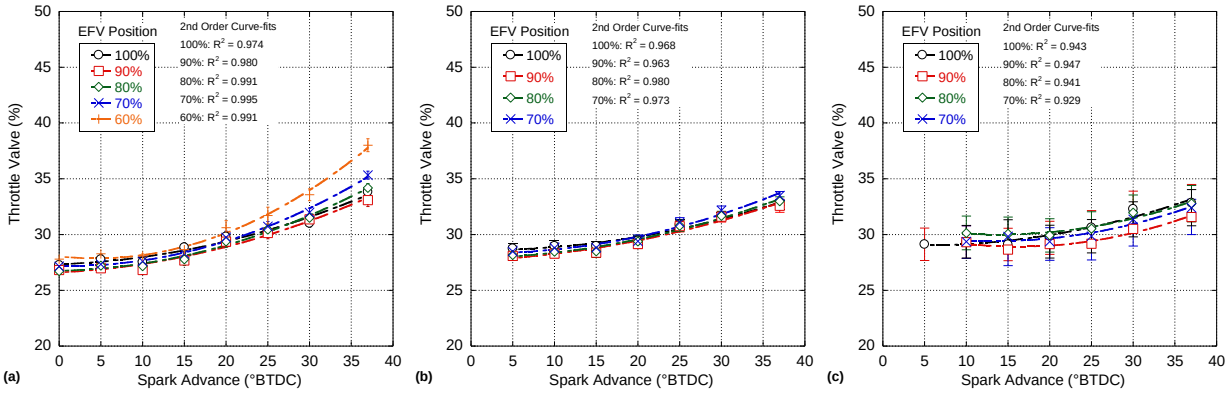

Figure 31: Throttle Valve (TV) Position during SA Sweeps at (a) No Load Added, (b) One Load (3.2 kW), and (c) Two Loads (6.4 kW)

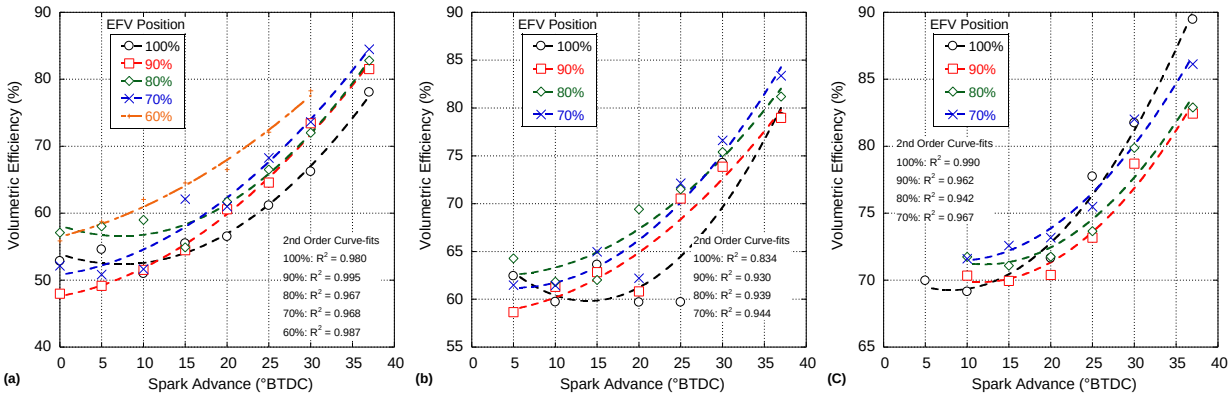

Figure 32: Volumetric Efficiency for SA Sweeps at (a) No Load Added, (b) One Load (3.2 kW), and (c) Two Loads (6.4 kW)

As mentioned prior, the airflow rate is not controlled directly since the TV is programmed to operate in a closed-loop at a set point of 1800 rpm. Therefore, the lambda sensor was used to monitor and record the AFR of the mixture at the different loading points as illustrated in Figure 29. The results demonstrate that the EFV appears to operate as intended; i.e., closing the EFV restricts the gaseous fuel flow to the engine at each *SA* and lambda increases. However, as load grows, the change in lambda between EFV positions decreases. This is a function of increasing stability of the system as the load on the engine increases. Under idle conditions, a minimum amount of fuel is needed to maintain engine speed. However, as the power requirement increases, combustion becomes more stable and consistent. This effect is found to be in tandem with previously established trends of growing cyclic variation for throttled gaseous engines operating at a lean mixture, due to the incomplete mixing of fuel and air [64].

Furthermore, as the spark is advanced, the engine operates leaner. In order to understand why, the airflow rates through the engine along with the in-cylinder pressure traces require examination.

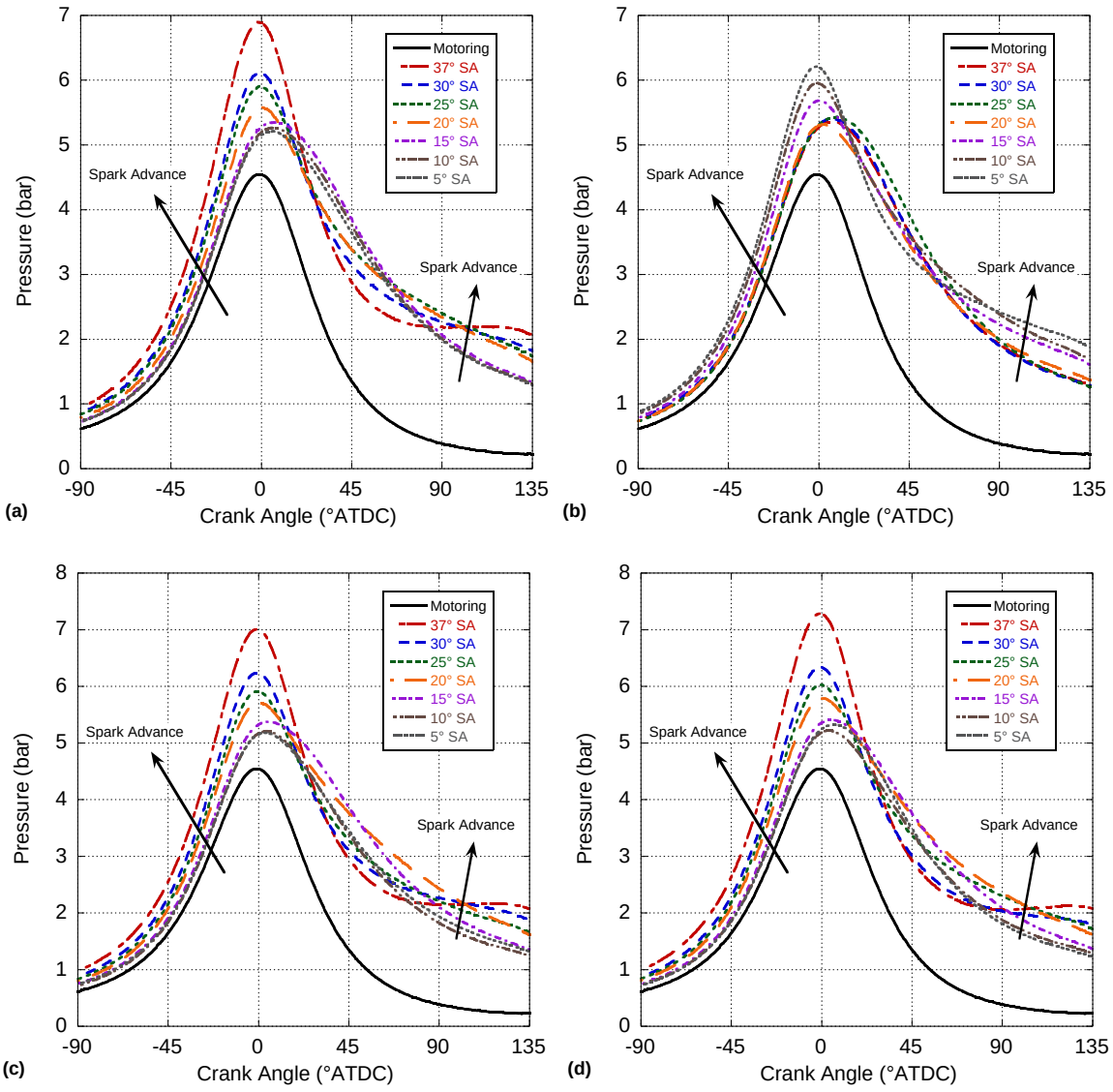

Figure 33: In-Cylinder Pressure at No Load for (a) 100%, (b) 90%, (c) 80%, and (d) 70% EFV Positions

Interestingly, the engine initially runs lean when the EFV is fully open. Since the ambient airflow rate is, effectively, set by the carburetor (Appendix A), changing the beginning lambda set point requires adjustment of the power screw on the carburetor. However, this will subsequently require a re-configuring of the EFV settings. This screw has to remain fixed during the EFV travel event in order for stable operation of the system. The reason this effort is successful in controlling the fuel flow while maintaining the TV in a closed loop is that the cross-section of fuel flow through the carburetor is kept constant.

Investigating the airflow rate in Figure 30 finds that as the EFV closes, the amount of air entering the engine increases at all loads. Furthermore, Figure 31 elucidates that the TV mostly opens as the EFV closes at the no load and one load conditions. Here, the volumetric efficiency of the engine (Figure 32) is increasing as less gaseous fuel is taking up intake space. This acts to increase lambda and lean out the engine further. Moreover, in order to maintain the engine load at the set speed, the TV opens so that it can bring in a greater amount of mixture; i.e., maintain the same energy addition rate. In addition, as load increases the airflow rate becomes more consistent due to an enhancement of combustion stability. However, at the largest load on the engine, volumetric efficiency does not have definite trend. Furthermore, no prescribed trend in the TV can be distinctly identified at this load level. In addition, as the engine runs leaner, there is potentially lower amounts of residual exhaust gas in the cylinder (i.e., residual fraction) provided combustion is complete.

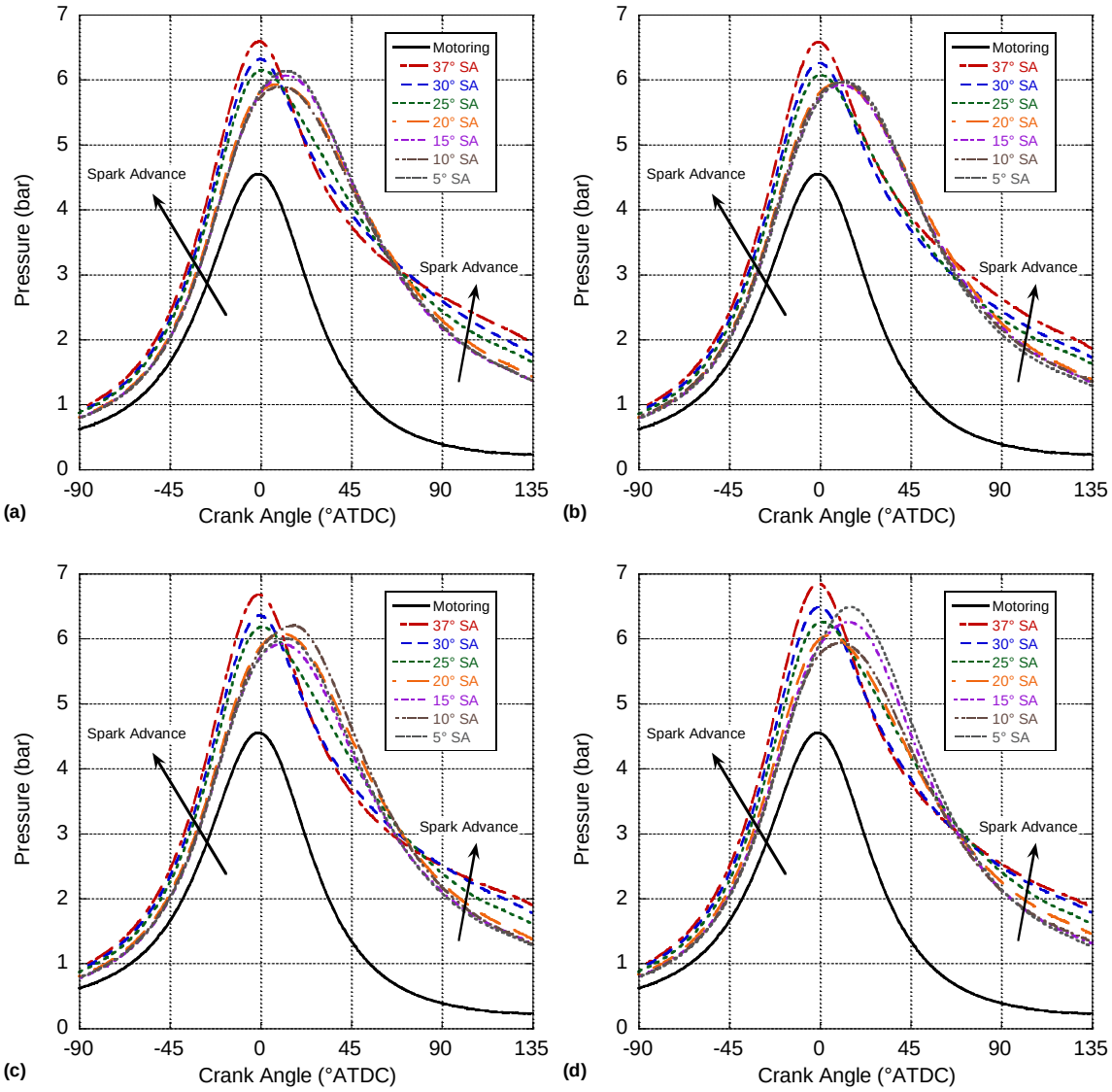

Figure 34: In-Cylinder Pressure at One Load for (a) 100%, (b) 90%, (c) 80%, and (d) 70% EFV Positions

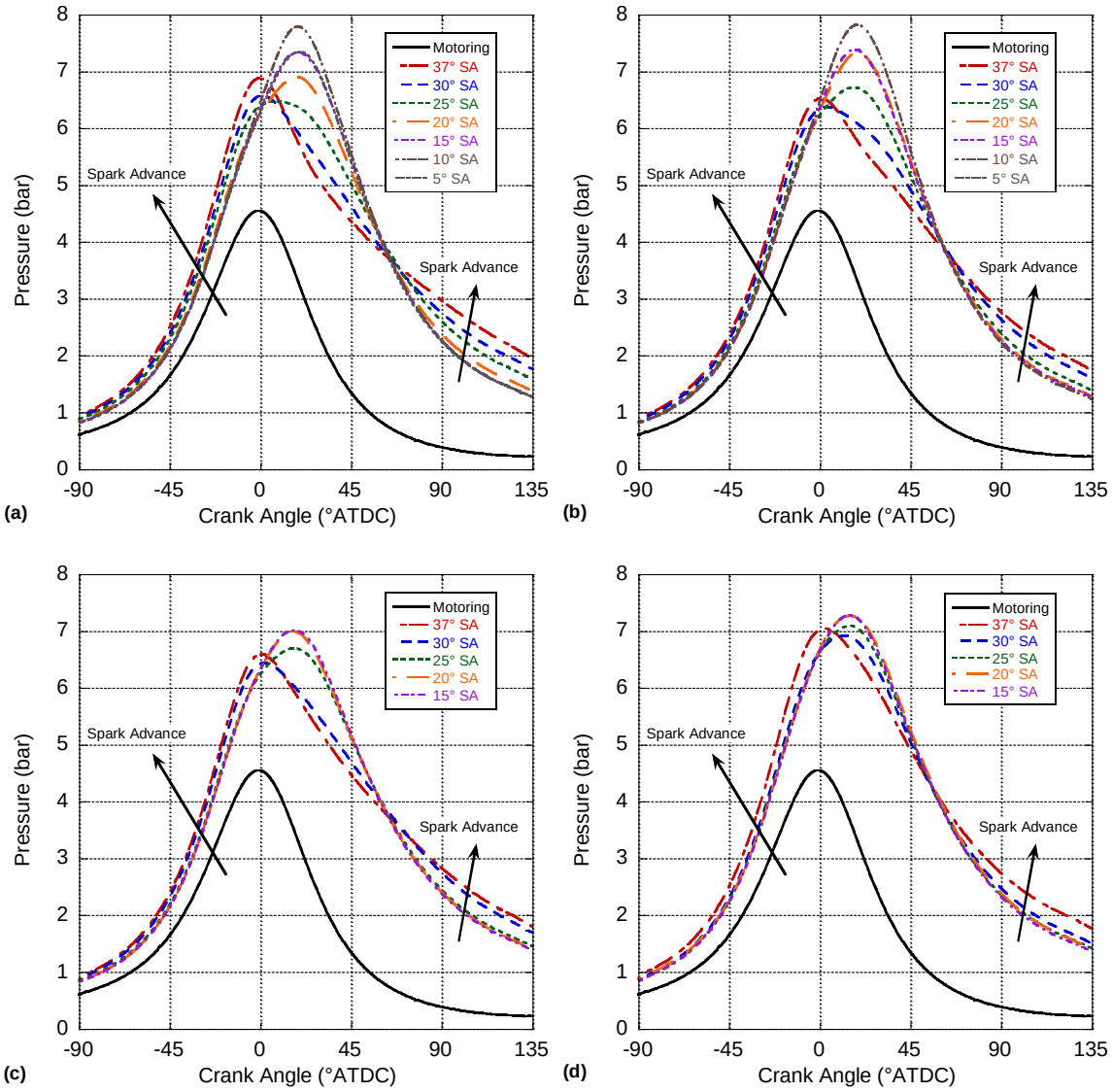

Figure 35: In-Cylinder Pressure at Two Loads for (a) 100%, (b) 90%, (c) 80%, and (d) 70% EFV Position

For additional insight, investigating the in-cylinder pressure data in (Figure 33, Figure 34, and Figure 35) reveals that at all loads the maximum pressure at each load does not change dramatically as the EFV closes. For example, under two loads at 20° *SA* the maximum pressure remains around 7 bar and at approximately 20° ATDC under all EFV positions. This should be the case since load on the engine is being held constant as EFV position changes; hence, indicated work must be relatively consistent. As a result, since the engine is running leaner and the airflow rate is increasing with a reduced EFV, a greater fuel flow rate must also occur to compensate for the needed release of energy. Combining this with a change in residual fraction along with a possible variation in intake and exhaust wave dynamics results in

a varying volumetric efficiency under the two load condition. At no load and one load, the airflow rate changes more dramatically in Figure 30; hence, its influence overrides the other parameters resulting in an increase in volumetric efficiency in Figure 32 as the EFV closes.

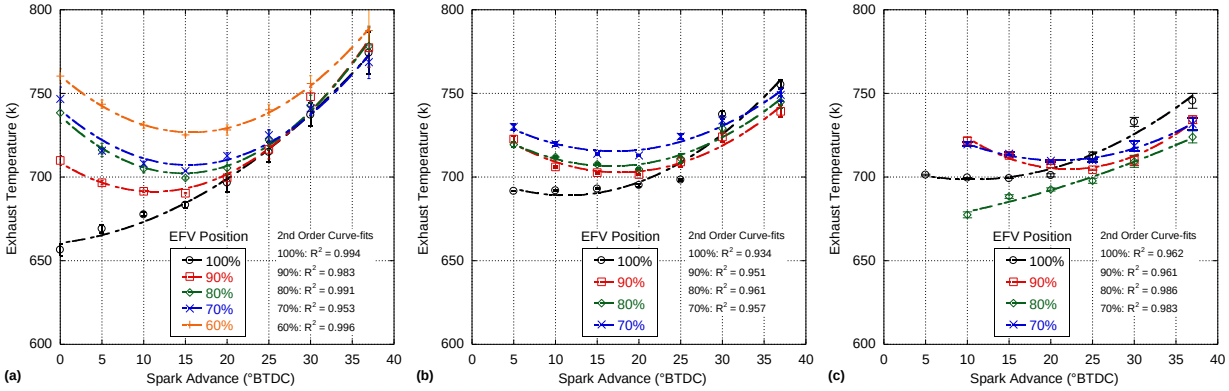

Figure 36: Exhaust Temperatures during SA Sweeps for (a) No Load Added, (b) One Load (3.2 kW), and (c) Two Loads (6.4 kW)

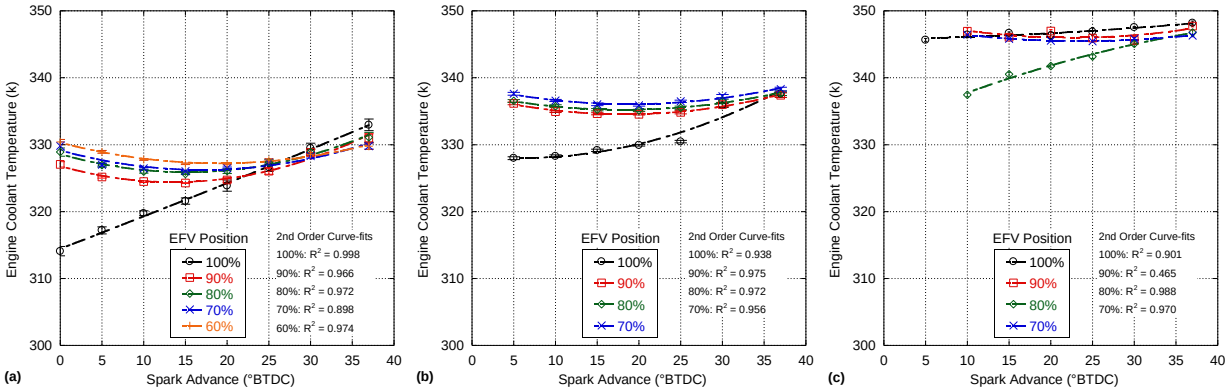

Figure 37: Engine Coolant Temperature during SA Sweeps for (a) No Load Added, (b) One Load (3.2 kW), and (c) Two Loads (6.4 kW)

With respect to spark timing, looking at the in-cylinder pressure data finds that combustion progresses into the compression stroke as the spark is advanced. As a result, the dual compression of the working fluid due to the piston and combustion generally causes higher in-cylinder pressures (except at two loads). Therefore, the pressures at the end of the expansion process at all loads are growing and contributing to a more effective thermodynamic blowdown process via a larger pressure drop across the exhaust valve. This will result in a lower amount of residual gas in the engine, subsequently allowing more air to enter (Figure 30). Analogous findings by Jang et al. illustrate that throttling the exhaust and

increasing the backpressure (i.e., lowering the pressure drop across the exhaust valve) will result in a growth of residual gas fraction [65]. Here, less residual and more air means that lambda also grows (Figure 29) with spark advance while the TV opens to provide more fuel energy (Figure 31). Overall, this results in an enhancement of volumetric efficiency (Figure 32) with *SA*.

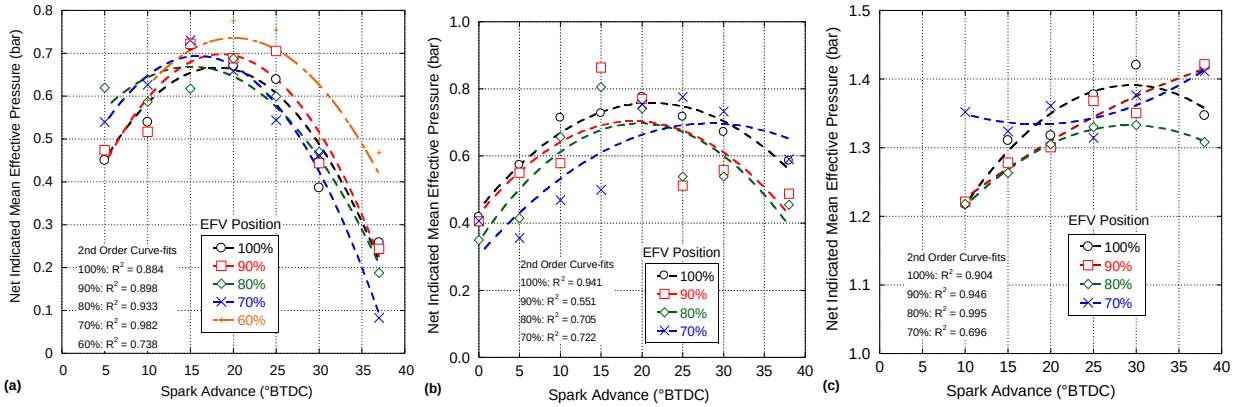

Figure 38: Net Indicated Mean Effective Pressure during SA sweeps for (a) No Load Added, (b) One Load (3.2 kW), and (c) Two Loads (6.4 kW)

In regards to exhaust temperatures, a parabolic trend is seen with a minimum around halfway through the spark sweep. Therefore, while larger exhaust temperatures occur with a significantly delayed spark as to be expected (i.e., late combustion as the exhaust valve opens), the highest exhaust temperatures actually happen when the spark is the most advanced. Reviewing the engine coolant findings in Figure 37 illustrate that the coolant temperature profile also grows with SA. Specifically, spark advance leads to higher in-cylinder temperatures and a greater time for heat transfer to the coolant. Hence, an increase in coolant temperature will correspondingly generate higher exhaust temperatures as the walls are hotter and less heat escapes during the later stages of combustion. Future work should endeavor to maintain a consistent coolant temperature as changes to its level significantly influence exhaust temperatures; e.g., Figure 36 almost mirrors Figure 37. This variance in exhaust and coolant temperatures also helps to explain the fluctuating volumetric efficiency findings of Figure 32. Since the residual in the engine is changing temperature and the inlet air is seeing hotter and/or cooler wall temperatures, the initial air and residual mixing process will vary and change how the engine breathes.

Mostly, exhaust temperatures grow as the mixture leans and less fuel energy is ideally available; hence, an opposite trend of expected. Reviewing Figure 30 demonstrates that the airflow rate dramatically

grows under no load and one load; therefore, the fuel flow rate must increase correspondingly (discussed prior). Combining this with a greater potential for incomplete combustion helps to explain the exhaust temperature in Figure 36; i.e., the amount of fuel added to the engine actually increases when running lean. When air flow rates become more steady at two loads, the exhaust temperature trend begins to reverse course and lower temperatures are generally seen when the mixture leans and less fuel burns (although skewed by the coolant temperature).

Reviewing the in-cylinder pressure data and the net IMEP calculated from these data in Figure 38 finds that MBT varies as a function of AFR and load, as to be anticipated. Investigating a single EFV position, optimum spark timing involves a trade-off between compression and expansion work. Too advanced of a spark timing can be damaging to the engine as double (negative) compression due to the piston and combustion can occur. On other hand, delaying the spark timing results in a loss of expansion work and higher exhaust gas temperatures [25, 34, 66]. With respect to the change in MBT as a function of AFR ratio, ideally as the mixture leans and the laminar flame speed decreases growing the ignition lag, the spark should be advanced. However, the second order curve-fits illustrate that no defined trend can be found. Again, the variance in coolant temperatures may be skewing the ideal trend anticipated.

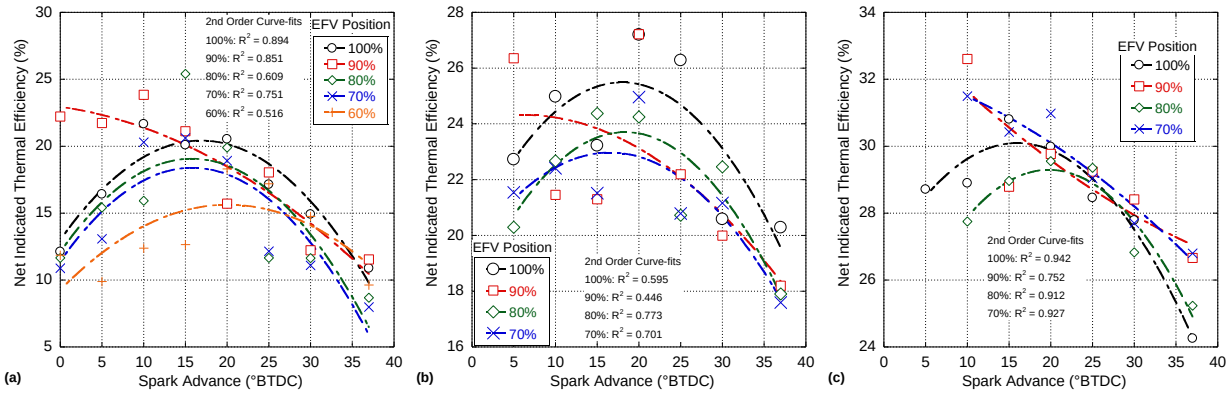

Figure 39: Net Indicated Thermal Efficiency during SA Sweeps for (a) No Load Added, (b) One Load (3.2 kW), and (c) Two Loads (6.4 kW)

In general, the automotive industry is moving towards lean burn engines since this takes advantage of a greater ratio of specific heats, subsequently enhancing expansion work and the thermal efficiency of the engine. However, reviewing Figure 39 finds that thermal efficiency of this engine actually (mostly) decreases as the mixture leans. This is assumed here to be a function of the relative

amount of combustion instability at low loads resulting in the need to bring in a significantly greater amount of fuel (and air) that burns less completely. This trend should switch as the loading on the engine increases that subsequently enhances stability (note: the generator has a 50 kW potential) while also allowing for greater combustion efficiencies. Finally, as the spark is advanced the thermal efficiency of the engine will decrease as more work is performed at non- optimum timings (e.g., greater levels of compression work). This should result in an increase in fuel consumption, subsequently reflected in an increase in the openness of the TV that grows more dramatically at very advanced timings. This downward trend in thermal efficiency also occurs at significantly delayed timings as combustion is happening late in the expansion phase when power cannot be effectively generated.

The error analysis for the presented measurement was completed using by calculating the relative standard deviation. As a result, the coefficients of variation for the engine lambda in Figure 29 are about 0.30%, 0.18%, and 0.14% for no-load, one-load, and two-load, respectively. Similarly, the coefficients of variation for the air mass flow rates in Figure 30 are about 1.4%, 0.8%, and 0.6% for no-load, one-load, and two-load, respectively. Additionally, the coefficients of variation for the exhaust temperatures in Figure 36 are about 0.60%, 0.22%, and 0.22% for no-load, one-load, and two-load, respectively. Moreover, the coefficients of variation for the engine coolant in Figure 37 are about 0.12%, 0.06%, and 0.07% for no-load, one-load, and two-load, respectively.

3.8 Conclusion

The Syngas Rig is a unique system at the University of Kansas that takes advantage of the abundance of glycerin generated as a by-product of biodiesel. Using a nickel catalyst reformer, glycerin is converted into a synthesis gas that fuels a coupled engine-generator system to create power. The engine can be powered by any of three gaseous fuels (PP, RP, and RG) with each fuel option serving a specific task. Previously, the Syngas Rig employed a gaseous carburetor in order to accommodate the different fueling requirements imposed by changes to fuel chemistry. This effort demonstrates the operation of a newly installed EFV that facilities dynamic control of the engine's AFR. Operation of this fuel control occurs in parallel with a closed-loop TV that maintains the engine at a rotary speed of 1800 rpm. This

EFV employs a PWM signal in order to minimize the effect of pressure waves during transient operation. Additionally, fuel control is accompanied by a computer-control ignition system that permits a dynamic change of the spark timing based on the different operation parameters such as load, coolant temperature, atmospheric conditions, and AFR.

Experiments using PP as the fuel while including a spark advance sweep along with changing the EFV position highlighted a successful implementation of the new closed-loop control system. Closing the EFV resulted in an increase in airflow rate to the engine while the operational lambda grew. However, no prescribed trend in volumetric efficiency was determined under the highest load. This may be due to a variance in wave dynamics through the intake and exhaust along with the need to increase the amount of fuel in order to maintain a set load condition. Furthermore, the impact of inconsistent coolant temperatures potentially changed the engine breathing event by varying the temperature of the cylinder walls and residual gas. Generally, the in-cylinder pressure followed a known trend by increasing with spark advance; whereas, thermal efficiency resulted in an opposite outcome since it decreased with larger lambdas. Future efforts should endeavor to maintain a consistent coolant temperature to help reduce non-linearity in the findings. Finally, others may use the information provided to aid in their efforts to generate a flex-fuel gaseous SI engine.

Chapter IV: Conclusions and Future Work

A greater interest in alternative fuel sources has been driven by the growing challenges posed by the usage of fossil fuels as the main source of energy in the world. Hence, recent research and development in the transportation sector has focused on biodiesel as a viable alternative energy source, and the production of biodiesel has been growing due to its attractive features such as the adaptability to existing conventional engines. This increase has led to the accumulation of glycerin, an inevitable by-product of the biodiesel transesterification process. Thus, recent efforts have focused on making use of this excess glycerin in order to increase the economic feasibility of biodiesel production.

The Syngas Rig is a unique system at the University of Kansas that takes advantage of the abundance of glycerin generated as a by-product of biodiesel. Using a nickel catalyst reformer, glycerin is converted into a synthesis gas that fuels a coupled engine-generator system to create power. The engine can be powered by any of three gaseous fuels (PP, RP, and RG) with each fuel option serving a specific task. Recent changes in the Syngas Rig included the renovation and replacement of various components in order to enhance the efficiency of the system and resolve encountered issues. For instance, a recently installed water pump in the cooling system replaced the stock mechanical pump to eliminate an engine overheating issue. For a stationary engine in a confined space, this new pump has proven to be sufficient in providing enough cooling for the engine to run within acceptable operating limits in the summer. Moreover, during engine operation, the computer program employed regulates the water pump such that it activates automatically when the temperature of the engine coolant exceeds a threshold of 165°F.

Furthermore, additional upgrades and modifications to the Syngas Rig have been accomplished in order to enhance the efficiency of the system while resolving encountered issues. Additionally, the Syngas Rig has been reconfigured such that the operation of the entire system can be controlled using mechanical switches inside the rig, in conjunction with electric switches using digital and analog signals from the data acquisition (DAQ) system. Moreover, safety measures were implemented in the fueling system in order to prevent any unintentional activation of fuel flow. For instance, as a safety precaution, the master propane solenoid activation now requires both the mechanical switches on the control panel

and an electric relay controlled digitally by the DAQ system to be ON. Similarly, all the operation paths require the activation of both mechanical and electric switches by wiring in series instead of through parallel circuits.

Overall, these components along with the Secondary DAQ must work in synchronicity in order to acquire a valid set of high-speed in-cylinder pressure data. With this in mind, multiple troubleshooting tools were implemented in the Secondary DAQ system during the re-installation of this system at HERDC in order to aid in pinpointing problems. More importantly, a complete understanding of this system is undoubtedly critical during diagnostics or when modifying the system. Therefore, the working mechanism of the Secondary DAQ system is reviewed here. The components of this system can be categorized or sorted as a function of hardware device, program algorithm, or signal waveform. Afterward, the troubleshooting process of the previous version and/or adaptation is overviewed.

Previously, the Syngas Rig employed a gaseous carburetor in order to accommodate the different fueling requirements imposed by changes to fuel chemistry. This effort demonstrates the operation of a newly installed EFV that facilities dynamic control of the engine's AFR. Operation of this fuel control occurs in parallel with a closed-loop TV that maintains the engine at a rotary speed of 1800 rpm. This EFV employs a PWM signal in order to minimize the effect of pressure waves during transient operation. Additionally, fuel control is accompanied by a computer-control ignition system that permits a dynamic change of the spark timing based on the different operation parameters, such as load, coolant temperature, atmospheric conditions, and AFR.

Experiments using PP as the fuel while including a spark advance sweep along with changing the EFV position highlighted a successful implementation of the new closed-loop control system. Closing the EFV resulted in an increase in airflow rate to the engine while the operational lambda grew. However, no prescribed trend in volumetric efficiency was determined under the highest load. This may be due to a variance in wave dynamics through the intake and exhaust along with the need to increase the amount of fuel in order to maintain a set load condition. Furthermore, the impact of inconsistent coolant temperatures potentially changed the engine-breathing event by varying the temperature of the cylinder

walls and residual gas. Generally, the in-cylinder pressure followed a known trend by increasing with spark advance; whereas, thermal efficiency resulted in an opposite outcome since it decreased with larger lambdas. Future efforts should endeavor to maintain a consistent coolant temperature to help reduce non-linearity in the findings. Finally, others may use the information provided to aid in their efforts to generate a flex-fuel gaseous SI engine.

Moving forward, forthcoming efforts may include the replication of AFR and spark timing sweeping process for the reformed fuels (i.e., reformed propane and reformed glycerin). Furthermore, the Syngas Rig may be expanded to include an exhaust analysis system; hence, catering for all engine optimization criteria including fuel economy, performance, and exhaust emissions. Finally, the Syngas Rig may be additionally enhanced by introducing an external EGR structure to facilitate a reduction in NO_x emissions when necessary.

References

1. "Biodiesel Technical Highlights", 2010, Office of Transportation and Air Quality,: National Service Center for Environmental PublicationsAvailable from: http://nepis.epa.gov/Exe/ZyPDF.cgi?Dockey=P1006V0I.pdf.
2. McCormick, R. and Tyson, K., "Biodiesel Handling and Use Guide", 2009, National Renewable Energy Laboratory, NREL Report.
3. "U.S. Biodiesel Production, Exports, and Consumption", 2015, U.S. Energy Information Administration: EIA Monthly Energy Review, Table 10.4. Available from: http://www.afdc.energy.gov/data/10325.
4. Johnson, D. T. and Taconi, K. A., "The glycerin glut: Options for the value- added conversion of crude glycerol resulting from biodiesel production". *Environmental Progress*, 2007. 26(4): p. 338-348
5. Ayoub, M. and Abdullah, A. Z., "Critical review on the current scenario and significance of crude glycerol resulting from biodiesel industry towards more sustainable renewable energy industry". *Renewable and Sustainable Energy Reviews*, 2012. 16(5): p. 2671-2686. http://dx.doi.org/10.1016/j.rser.2012.01.054
6. Clomburg, J. M. and Gonzalez, R., "Anaerobic fermentation of glycerol: a platform for renewable fuels and chemicals". *Trends in Biotechnology*, 2013. 31(1): p. 20-28. http://dx.doi.org/10.1016/j.tibtech.2012.10.006
7. Fan, X., Burton, R., and Zhou, Y., "Glycerol (byproduct of biodiesel production) as a source for fuels and chemicals–mini review". *Open Fuels Energy Sci J*, 2010. 3: p. 17-22
8. Haas, M. J., McAloon, A. J., Yee, W. C., and Foglia, T. A., "A process model to estimate biodiesel production costs". *Bioresource Technology*, 2006. 97(4): p. 671-678. http://dx.doi.org/10.1016/j.biortech.2005.03.039
9. Werpy, T. and Petersen, G., "Top Value Added Chemicals from Biomass: Volume I -- Results of Screening for Potential Candidates from Sugars and Synthesis Gas", in *Other Information: PBD: 1 Aug 2004*2004. p. Medium: ED; Size: 76 pp. pagesAvailable from: http://www.osti.gov/scitech//servlets/purl/15008859-s6ri0N/native/.
10. Klein, M., "Impact of biodiesel production on the glycerol market", 2006, Whitford: Miller Klein Associates. Retrieved from http://archive. hgca. com/publications/documents/Impact_of_Biodiesel_Production_on_the_Glycerol_Market. pdf. Available from: http://cereals-2.ahdb.org.uk/publications/documents/Impact_of_Biodiesel_Production_on_the_Glycerol_Market.pdf.
11. "Glycerine and the Market". Crude Glycerin; Available from: http://biofuelstechnologyllc.com/Crude_Glycerine.html.
12. Cecrle, E. D., "Controls and measurements of KU engine test cells for biodiesel, SynGas, and assisted biodiesel combustion", 2011, University of Kansas.
13. Kinoshita, E., Hamasaki, K., Jaqin, C., and Takasaki, K., "Combustion Characteristics for Diesel Engines with Emulsified Biodiesel Without Adding Emulsifier", 2004, SAE International. Available from: http://dx.doi.org/10.4271/2004-01-1860.
14. Junior, F. S. C., Cavalcante, F., Alves, J., and de Lima, L., "Parameters analysis of the assisted combustion of residual biodiesel glycerol". *International Transaction Journal of Engineering, Management, & Applied Sciences & Technologies*, 2012. 3(4): p. 10
15. Pickett, D. and Depcik, C., "Use of the Glycerine By-product from Biodiesel Production for Power Generation", 2014, University of Kansas.
16. Pickett, D., "Design and Operation of the Synthesis Gas Generator System for Reformed Propane and Glycerin Combustion", 2013, University of Kansas.
17. "Fuel Reformer, Engine, and Generator System". Available from: http://depcik.faculty.ku.edu/syngas.

18. Roth, K. J., Sobiesiak, A., Robertson, L., and Yates, S., "In-cylinder pressure measurements with optical fiber and piezoelectric pressure transducers", 2002, SAE Technical Paper.
19. Amann, C. A., "Cylinder-Pressure measurement and Its Use in Engine Research", 1985, SAE International. Available from: http://dx.doi.org/10.4271/852067.
20. Zhao, H. and Ladommatos, N., "Engine Combustion Instrumentation and Diagnostics"2001: Society of Automotive Engineers. Available from: https://books.google.com/books?id=w5dTAAAAMAAJ.
21. Mangus, M. D., "Design, construction, and validation of an in-cylinder pressure recording system for internal combustion engine analysis", 2012, University of Kansas.
22. "Engine Combustion Analysis Engine Pressure Measurement for Research and Development", Kistler Instrument. Available from: https://www.kistler.com/us/en/.
23. Rogers, D. R., "Engine Combustion: Pressure Measurement and Analysis"2010: SAE International.
24. "Instrument Fundamentals Complete Guide", 2017: Austin, TXAvailable from: http://www.ni.com/white-paper/3214/en/.
25. Taylor, C. F., "The Internal-combustion Engine in Theory and Practice: Combustion, fuels, materials, design". Vol. 2. 1985: MIT press.
26. "NI R Series Multifunction RIO Specifications -PCIe-7841R ", 2009, National Instruments: Austin, TX.
27. Proakis, J. G., "Digital Signal Processing Principles Algorithms And Applications"1996: Phi. Available from: https://books.google.com/books?id=-uUWuAAACAAJ.
28. Meyer-Baese, U., "Digital Signal Processing with Field Programmable Gate Arrays"2007: Springer Berlin Heidelberg. Available from: https://books.google.com/books?id=wzYuOF6HFX0C.
29. Heim, A. "Make it Faster: More Throughput or Less Latency?". National instruments White Papers 2015; Available from: http://www.ni.com/white-paper/14990/en/.
30. "NI LabVIEW High-Performance FPGA Developer's Guide", in *Recommended Practices for Optimizing LabVIEW RIO Applications*2014, National Instruments.
31. "NI R Series Multifunction RIO User Manual (NI 781xR, NI 783xR, NI 784xR, and NI 785xR Devices)", National instruments: Austin, TX.
32. "Avoiding Buffer Errors in DMA Applications (FPGA Module)". LabVIEW 2016 FPGA Module Help, 2016.
33. Pischinger, R., "Engine Indicating User Handbook"2002, Austria: AVL List GmbH, Graz, Austria.
34. Heywood, J. B., "Internal combustion engine fundamentals". Vol. 930. 1988: Mcgraw-hill New York.
35. Randolph, A. L., "Methods of processing cylinder-pressure transducer signals to maximize data accuracy", 1990, SAE Technical paper.
36. Davis, R. S. and Patterson, G. J., "Cylinder Pressure Data Quality Checks and Procedures to Maximize Data Accuracy", 2006, SAE International. Available from: http://dx.doi.org/10.4271/2006-01-1346.
37. Churkunti, P., Mattson, J. M., and Depcik, C., "Influence of Fuel Injection Pressure and Biodiesel upon NO x Emissions", 2016, SAE Technical Paper. Available from: https://doi.org/10.4271/2016-01-0877.
38. "U.S. Biodiesel Production, Exports, and Consumption", U.S. Energy Information Administration: EIA Monthly Energy Review, Table 10.4. Available from: https://www.afdc.energy.gov/data/10325.
39. Makkar, H. P., Guariguata, M., Sinclair, B., K Khadar, I., et al., "Biofuel co-products as livestock feed: opportunities and challenges"2012: FAO, Roma (Italia).
40. Kumar, P., Mehariya, S., Ray, S., Mishra, A., et al., "Biodiesel industry waste: a potential source of bioenergy and biopolymers". *Indian Journal of Microbiology*, 2015. 55(1): p. 1-7

41. Pickett, D. K. and Depcik, C. D. "Combustion of Reformed Propane as Segue to Glycerin Reforming". presented at ASME 2013 International Mechanical Engineering Congress and Exposition. 2013. American Society of Mechanical Engineers.
42. Das, L., Gulati, R., and Gupta, P., "Performance evaluation of a hydrogen-fuelled spark ignition engine using electronically controlled solenoid-actuated injection system". *International Journal of Hydrogen Energy*, 2000. 25(6): p. 569-579
43. Das, L., Gulati, R., and Gupta, P. K., "A comparative evaluation of the performance characteristics of a spark ignition engine using hydrogen and compressed natural gas as alternative fuels". *International Journal of Hydrogen Energy*, 2000. 25(8): p. 783-793
44. Korakianitis, T., Namasivayam, A., and Crookes, R., "Natural-gas fueled spark-ignition (SI) and compression-ignition (CI) engine performance and emissions". *Progress in Energy and Combustion Science*, 2011. 37(1): p. 89-112
45. Cho, H. M. and He, B.-Q., "Spark ignition natural gas engines—A review". *Energy Conversion and Management*, 2007. 48(2): p. 608-618. https://doi.org/10.1016/j.enconman.2006.05.023
46. Zeng, K., Huang, Z., Liu, B., Liu, L., et al., "Combustion characteristics of a direct-injection natural gas engine under various fuel injection timings". *Applied Thermal Engineering*, 2006. 26(8): p. 806-813. https://doi.org/10.1016/j.applthermaleng.2005.10.011
47. Jeong, C., Kim, T., Lee, K., Song, S., et al., "Generating efficiency and emissions of a spark-ignition gas engine generator fuelled with biogas–hydrogen blends". *International Journal of Hydrogen Energy*, 2009. 34(23): p. 9620-9627. https://doi.org/10.1016/j.ijhydene.2009.09.099
48. Van Blarigan, P., "Advanced internal combustion electrical generator". *Proceedings of the 2002 DOE Hydrogen Program Review, National Renewable Energy Laboratory, Golden, CO, May*, 2002: p. 6-10
49. Quader, A. A., "Lean combustion and the misfire limit in spark ignition engines", 1974, SAE Technical Paper.
50. Karim, G. and Wierzba, I., "Experimental and analytical studies of the lean operational limits in methane fuelled spark ignition and compression ignition engines", 1989, SAE Technical Paper.
51. "Woodward L-Series Integrated Speed Control: Installation and Operation Manual", Woodward, Inc.Available from: http://woodward.com/searchpublications.aspx.
52. "Carburetion Theory and Operation", 2016, IMPCO Technologies Inc: 3030 South Susan St. Santa Ana, CA 92704. Available from: http://www.impcotechnologies.com/.
53. Jensen, B., Oprea, R., Westerdale, T., and Hussain, S., "The Design and Development of a Dedicated Propane Fuel System for the General Motors Medium Duty Truck", 1998, SAE International. Available from: http://dx.doi.org/10.4271/981921.
54. Sundar, D., VenuMadhav, S., Srinivasan, B., Govindarajan, S., et al., "Electronic Control of Air/Fuel Ratios in a carburettor for 2-Wheeler Application", 2008, The Automotive Research Association of India. Available from: http://dx.doi.org/10.4271/2008-28-0057.
55. "Assured Automation V4 Series Electric Valve Actuators", Assured Automation (AA EV1S1V1). Available from: https://assuredautomation.com/index.php.
56. Reader's Digest, A., "Reader's Digest Complete car care manual"1981, Pleasantville, N.Y.: Reader's Digest Association (Canada) in conjunction with the Canadian Automobile Association.
57. Wanklyn, N., "ME 899 Final Report", 2011, Mechanical Engineering: University of Kansas.
58. "DynamicEFI EBL Flash System".
59. Mansur, M. "The Basics of creating an ECU file (or any definition file) from a hack".
60. "Light Duty Trucks Service Manual", in *Consumer Information Truck-Camper Loading*1990, GENERAL MOTORS CORPORATION: Warren, Michigan.
61. Denton, T., "Automobile electrical and electronic systems"2004: Routledge.
62. "Material Handling & Industrial Engine Gaseous Fuel Training Manual", 1998, IMPCO Technologies Inc: 16804 Gridley Place, Cerritos, CA 90703-1741.
63. "Streamline Fuel Systems for LPG and Natural Gas Engines.", Woodward Governor Company. Available from: http://www.ngvina.com/streamline/.

64. Gupta, H. N., "Fundamentals of Internal Combustion Engines"2006: Prentice-Hall Of India Pvt. Limited. Available from: https://books.google.com/books?id=MFx4VRErHNoC.
65. Jang, J., Yeom, K., and Bae, C., "Effects of Exhaust Throttling on Engine Performance and Residual Gas in an SI Engine", 2004, SAE International. Available from: https://doi.org/10.4271/2004-01-2974.
66. "Bosch Automotive Handbook". 8th ed2011, Plochingen, Germany: Robert Bosch GmbH.
67. Wilson, J., "Custom GM EFI Systems Manuals", 2003: CustomEFIAvailable from: http://www.gmcmi.com/wp-content/uploads/2014/05/How-to-Build-a-GM-EFI-System.pdf.
68. Engineering, O., "OMEGA Barometric Pressure Transmitte (Model EWS-BP-A)": http://www.omegamanual.info.
69. Edge, T., "Wideband Labda Controller (WBo2 2C0B)". Available from: http://wbo2.com/2c0/default.htm.
70. Motorsport, B., "Lambda Sensor LSU 4.9", in *Bosch Engineering GmbH 2017* 2017. Available from: http://www.bosch-motorsport.com/media/catalog_resources/Lambda_Sensor_LSU_49_Datasheet_51_en_2779147659pdf.pdf.

Appendix A: Primary DAQ Modules: Sensors and Controllers

Table 3: Primary DAQ - Mod 1: Analog Voltage Input (AVI) NI 9205

BRK#	Mod 1 Ch.	Variable(s) name in LabVIEW	Sensor
1	AI 0	Barometric Environmental Pressure	OMEGA EWS-BP-A
2	AI 1	Environmental Temperature	OMEGA EWS-RH
3	AI 2	Relative Humidity	OMEGA EWS-RH
4	AI 3	Differential Pressure across LFE	Omega PX277-30D5V
5	AI 4	Engine Temperature	Coolant Temperature Sensor (CTS)
6	AI 5	Engine Oil Pressure	Oil Pressure Switch
7	AI 6	Throttle Valve Position	Woodward Throttle
8	AI 7	Open channel	-
9	DO0	Digital Output	NA
10	COM	Common Reference to isolated ground	NA
11	AI 16	Propane Flow Signal (0-5 VDC)	Omega FMA 5444 gas flow controller
12	AI 17	Open channel	-
13	AI 18	Open channel	-
14	AI 19	Open channel	-
15	AI 20	Open channel	-
16	AI 21	Open channel	-
17	AI 22	Open channel	-
18	AI 23	Open channel	-
19	AISENSE	Non-Referenced Single Ended	NA
20	AI 8	Open Channel	-
21	AI 9	Battery Voltage (0-10 VDC)	-
22	AI 10	Post #1 Battery Voltage (0-10 VDC)	-
23	AI 11	Post #2 Battery Voltage (0-11 VDC)	-
24	AI 12	Open Channel	-
25	AI 13	Engine Lambda (Lambda Voltage Value)	Wideband Lambda Controller (WBo2-2C0B)
26	AI 14	Reformer Lambda	Wideband Lambda Controller (WBo2-2C0B)
27	AI 15	Open Channel	-
28	PFI0	Programmable function interface	NA
29	COM	Common Reference to isolated ground	NA
30	AI 24	System Propane Mass Flow	Omega FMA 5444 gas flow controller
31	AI 25	Reformer Air Mass Flow Rate	Omega FMA 1744 air flowmeter
32	AI 26	Open Channel	-
33	AI 27	Open Channel	-
34	AI 28	EFV Position	EFV Potentiometer (reported from BS2)
35	AI 29	Open Channel	-
36	AI 30	Open Channel	-
37	AI 31	Open Channel	-

Table 4: Primary DAQ - Mod 2: Analog Voltage Output (AVO): NI 9264 (NRSE)

BRK#	Mod 2 Ch.	Variable(s) name in LabVIEW	Sensors	Corresponding Ground (COM) Terminal
1	AO0	Glycerin Controller Output	Leeson DC Motor Controller (Model# 174291)	20
2	AO1	Reformer Air Flow Controller	Omega FMA 1744 Controller	21
3	AO2	Propane Controller Output	Omega FMA 5444 controller	22
4	AO3	Open channel	-	23
5	AO4	Open Channel	-	24
6	AO5	Open Channel	-	25
7	AO6	Reference signal for Lambda Controller	Tech Edge (WBo2 2C0B)	26
8	AO7	Open Channel	-	27
9	NC	No Connection	NA	28
10	NC	No Connection	NA	29
11	AO 8	Open channel	-	30
12	AO 9	Open Channel	-	31
13	AO 10	Open Channel	-	32
14	AO 11	Open channel	-	33
15	AO 12	Open Channel	-	34
16	AO 13	Open Channel	-	35
17	AO 14	Open Channel	-	36
18	AO 15	Open Channel	-	37
19	COM	Common Reference to isolated ground	NA	-

Table 5: Primary DAQ - Mod 3: Analog Current Input (ACI)

Mod 3/ ACI	Variable Name in LabVIEW	Sensor
ACI 0	LFE Pressure	Omega PX277-30D5V
ACI 1	Open Channel	-
ACI 2	Glycerin Pump Pressure	Omega PX319-030AI
ACI 3	Glycerin Inlet Pressure Transducer	Omega PX319-030AI
ACI 4	Density of the Reformer Air Supply	Omega FPD1001-R
ACI 5	**Back-Pressure Valve (BPV) Pressure**	**Omega PX319-030AI**
ACI 6	Engine Intake Pressure	Omega PX319-030AI
ACI 7	Open Channel	-
NC	No Connection	NA
COM	Common Reference to isolated ground	NA

Table 6: Primary DAQ - Mod 4: Analog Current Input (ACI)

Mod 4/ ACI	Variable Name in LabVIEW	Sensor
ACI 0	Engine Speed (RPM)	Woodward GCP 20 Controller
ACI 1	Generator Power	Woodward GCP 20 Controller
ACI 2	Open Channel	-
ACI 3	Post Reformer Pressure	Omega PX319-030AI
ACI 4	Open Channel	-
ACI 5	Open Channel	-
ACI 6	Engine Vacuum Pressure	Omega PX319-020AI
ACI 7	Glycerin Flowmeter	Omega FPD 1001-R high viscosity flowmeter
NC	No Connection	NA
COM	Common Reference to isolated ground	NA

Table 7: Primary DAQ - Mod 5: AVI (NI 9201)

Mod 5/ AVI	Variable Name in LabVIEW	Sensor
AI 0	Pressure (gage) After EFV	Omega PXM309-010G10
AI 1	Pressure (gage) Before EFV	Omega PXM309-010G10
AI 2	Open Channel	-
AI 3	Open Channel	-
AI 4	Open Channel	-
AI 5	Open Channel	-
AI 6	Open Channel	-
AI 7	Open Channel	-
NC	No Connection	NA
COM	Common Reference to isolated ground	NA

Table 8: Primary DAQ - Mod 6: Thermocouple (TC) - NI 9213

Mod 6/ TC	Variable Name in LabVIEW	Sensor
0	Reformer Surface Thermocouple 1	Omega Self-Adhesive Surface TC
1	Reformer Surface Thermocouple 2	Omega Self-Adhesive Surface TC
2	Reformer Surface Thermocouple 3	Omega Self-Adhesive Surface TC
3	Reformer Surface Thermocouple 4	Omega Self-Adhesive Surface TC
4	Reformer Surface Thermocouple 5	Omega Self-Adhesive Surface TC
5	Water Temperature Thermocouple	Omega k-type Probes (KQSS-18E-6)
6	Coolant Temperature Thermocouple	Omega k-type Probes (KQSS-18E-6)
7	Exhaust Temperature Thermocouple	Omega k-type Probes (KQSS-18E-6)
8	Before Heat Exchanger Thermocouple	Omega k-type Probes (KQSS-18E-6)
9	After Heat Exchanger Thermocouple	Omega k-type Probes (KQSS-18E-6)

Table 9: Primary DAQ - Mod 7: (NI 9403) Digital Input/Output (DIO)

Pin	Channel	Variable Name in LabVIEW	Direction	Notes
1	DIO 0	Master Propane (Solenoid 1)	output	in series with the manual switch
2	DIO 1	Engine Propane (Solenoid 2)	output	in series with the manual switch
3	DIO 2	Syngas Enable (Solenoid 4)	output	Switches Syngas Direction
4	DIO 3	Reformer Propane (Solenoid 3)	output	Digital Signal
5	DIO 4	Pump On (Enable Glycerin Flow)	output	Digital signal
6	DIO 5	Igniter (Enable Reformer relay)	output	Digital Signal
7	DIO 6	Back-Pressure Close (PWM)	output	PWM Signal
8	DIO 7	Back-Pressure Open	output	PWM Signal
9	COM	Common Reference to isolated ground	NA	All DIO channels are internally referenced the adjacent COM
10	COM	Common Reference to isolated ground	NA	
11	DIO 8	Starter Button	output	Engages the Engine Starter (momentary)
12	DIO 9	A/F + [Fuel Open]	output	Open EFV Signal to the BS2
13	DIO 10	A/F - [Fuel Close]	output	Close EFV Signal to the BS2
14	DIO 11	ECU Kill/Stop	output	Controls the ECU power
15	DIO 12	Air Supply	output	Controls the Air pump power
16	DIO 13	Water PUMP ON	output	Controls the Engine Water pump
17	DIO 14	Air increase	output	Increases Air Supply to the Reformer
18	DIO 15	Air Decrease	output	Decreases air supply to the reformer
19	RSVD	Reserved	NA	-
20	DIO 16	VCS	output	Vacuum Signal to VFF30
21	DIO 17	EFV Potentiometer Reference Signal	output	Feedback signal for the EFV Position
Channels DIO 18-DIO21 are currently open				
26	DIO 22	Open EFV	Output	Direct PWM Signal to open EFV
27	DIO 23	Close EFV	Output	Direct PWM Signal to Close EFV
28	COM	Common Reference to isolated ground	NA	-
29	COM	Common Reference to isolated ground	NA	-
30	DIO 24	Water pump relay status	Input	Reports the status of pump relay
Channels DIO 25-31 are currently open				

Table 10: Primary DAQ - Mod 8: Thermocouple (TC) - NI 9213

Mod 8/ TC	Variable Name in LabVIEW	Sensor
0	Engine Air - Laminar Flow Element	Omega k-type Probes (KQSS-18E-6)
1	Glycerin Supply Temperature - Pre Heat Exchanger	Omega k-type Probes (KQSS-18E-6)
2	Glycerin - Post Glycerin Heat Exchanger	Omega k-type Probes (KQSS-18E-6)
3	Syngas Heat Exchanger Inlet	Omega k-type Probes (KQSS-18E-6)
4	Glycerin - Glycerin Intake	Omega k-type Probes (KQSS-18E-6)
5	Reformer Air - Air Temperature	Omega k-type Probes (KQSS-18E-6)
6	Reactor Mixture - Upper Reformer	Omega k-type Probes (KQSS-18E-6)
7	Reactor - Catalyst Material	Omega k-type Probes (KQSS-18E-6)
8	Reformate - Post Reactor	Omega k-type Probes (KQSS-18E-6)
9	Propane - Reformer Supply	Omega k-type Probes (KQSS-18E-6)
10	Propane Tank Supply	Omega k-type Probes (KQSS-18E-6)
11	Syngas Cyclone (#1)	Omega k-type Probes (KQSS-18E-6)
12	Reformate - Post Cyclone #2	Omega k-type Probes (KQSS-18E-6)
13	Reformate - Pre Intercooler	Omega k-type Probes (KQSS-18E-6)
14	Reformate - Post Intercooler	Omega k-type Probes (KQSS-18E-6)
15	Reformate - Intake Temperature	Omega k-type Probes (KQSS-18E-6)

Table 11: Accuracy of measurement devices (according to manufacturer specifications) [67-70]

Device	Manufacturer (Model)	Output/Input	Accuracy
Barometric Pressure Transmitter	OMEGA (EWS-BP-A)	AVI (Mod 1)	±1% of Full scale
Relative Humidity / Temperature Transmitter	OMEGA (EWS-RH)	AVI (Mode 1)	Relative Humidity: From 5-20%, ± 4% RH From 20-80%, ± 3% RH From 80-95%, ± 4% RH Temperature: In Still Air: ± 1.2°F (0.7°C) @ 25°C ± 2.5°F (1.4°C) across full range In Moving Air: ± 2.5°F (1.4°C) @ 25°C ± 3°F (1.7°C) across full range
Differential Pressure Transducer	OMEGA (PX277-30D5V)	AVI (Mod 1)	±1.0% FS
Throttle Valve Position	Woodward (LC-50)	AVI (Mod 1)	±15.0% of rated speed
Gas-Mass Flow Controller	OMEGA (FMA-5444)	AVI	±1.5% of Full Scale
Air-Mass Flowmeter	OMEGA (FMA-1744)	AVI	±1.0% of Full Scale
Absolute Pressure Transducer	OMEGA (PX319-030AI)	0 - 30 psi (absolute)	±0.25% of Full Scale
Gage Pressure Transducer	OMEGA (PXM309-010G10)	0 -10 bar (gage)	±0.25% of Full Scale
Positive Displacement Flowmeters	OMEGA (FPD1001-R)		±1.0% of Full Scale
Temperature Thermocouple	OMEGA (KQSS-18E-6)	-454-2501°F	>32 to 2282°F (4.0°F or 0.75%) -328 to 32°F (4.0°F or 2.0%)
Wideband Lambda Controller	Tech Edge (WBo2-2C0B)		±0.1 of AFR (±0.005 Lambda)
Lambda Sensor	Bosch (LSU 4.9)	Current Pump (I_p)	Accuracy at Lambda (λ): λ= 0.8 ± 0.01 λ=1 ± 0.007 λ=1.7 ± 0.05

Appendix B: The Basic Stamp Code for Electric Fuel Valve (EFV) Control Unit

```
SAE Copy -- EFV 054 - EFV Only Stable.bs2                                Page 1/3
  1 ' {$STAMP BS2}
  2 ' {$PBASIC 2.5}
  3 ' University of Kansas
  4 ' Syngas-Rig
  5 ' Electronic Valve Control (EFV) Control unit
  6 ' Khalaf AlZeeby
  7 ' CLose  => Even pins
  8 ' Open   => Odd pins
  9 ' Closing EFV => CLOSE
 10 ' Opening EFV => OPEN
 11 ' For inputs from DAQ: use "INPUT" instead of "LOW"; to avoid the 3.5VDC
    and 1.5VDC error
 12
 13
 14
 15 DO
 16 Main:
 17 ' -----[ I/O Definitions ]---------------------------------------------
    ---
 18 BLUE            PIN    15     ' Output: BlUE LED; indicating the status of:
         pin 5: Toggle Switch is at open position    OR   pin 3: DAQ Red wire:
    Mod-1:DIO 9:(BRK#12): OPEN
 19 YELLOW          PIN    14     ' Output: YELLOW LED; indicating the status of:
         pin 2: Toggle Switch is at Close position   OR   pin 0: BLACK wire:
    Mod-1:DIO 10:(BRK#13): CLOSE
 20 CLOSE           PIN    7      ' Output: Travels CW; from 90 to 0; closing EFV
 21 OPEN_SWITCH     PIN    5      ' Input: Manual TOGGLE switch is in the Open
    position (up)
 22 OPEN            PIN    4      ' Output: Output: Travels CCW; from  0 to 90;
    opening EFV
 23 LV_OPEN         PIN    3      ' Input: Red wire from DAQ: Mod7-DIO 9 (BRK#12)
    : OPEN CCW
 24 CLOSE_SWITCH    PIN    2      ' Input: Manual Toggle switch is in the Close
    position (Down)
 25 LV_CLOSE        PIN    0      ' Input: Black wire from DAQ: Mod7-DIO 10 (
    BRK#13): Close
 26
 27 HIGH BLUE
 28 HIGH YELLOW
 29
 30 LOW CLOSE
 31 LOW OPEN
 32
 33 LOW CLOSE_SWITCH     ' Input: Toggle Switch is at open position
 34 LOW OPEN_SWITCH     ' Input: Toggle Switch is at Close position
 35
 36 INPUT LV_CLOSE
 37 INPUT LV_OPEN
 38
 39
 40 Main2:
 41
 42 ' ----- Error Check -----------------------------------------------------
 43 ' ERROR CHECK (Conflict between LabView and Toggle Switch)
 44 IF (LV_CLOSE = 1) AND (OPEN_SWITCH = 1) OR ((CLOSE_SWITCH = 1) AND (LV_OPEN
    = 1)) THEN
 45 TOGGLE YELLOW
```

```
 46 TOGGLE BLUE
 47 LOW CLOSE
 48 LOW OPEN
 49 PAUSE 100
 50
 51 ' ERROR CHECK
 52 ELSEIF (CLOSE_SWITCH = 1) AND (LV_OPEN = 1) THEN
 53 TOGGLE YELLOW
 54 TOGGLE BLUE
 55 LOW CLOSE
 56 LOW OPEN
 57 PAUSE 100
 58
 59 ' ERROR CHECK (Conflict between LabView Switches (If both Labview switches
    are turned ON accidentally))
 60 ELSEIF (LV_CLOSE = 1) AND (LV_OPEN = 1) THEN
 61 TOGGLE YELLOW
 62 TOGGLE BLUE
 63 LOW CLOSE
 64 LOW OPEN
 65 PAUSE 100
 66
 67 ' ----- ------------------------------------------------------------------
    -----
 68 'When everything is OFF
 69 ' ----- All switches are OFF ----------------------------------------------
    ------
 70 ELSEIF (LV_CLOSE = 0) AND (CLOSE_SWITCH = 0) AND (LV_OPEN = 0) AND (OPEN_
    SWITCH = 0) THEN
 71 HIGH YELLOW
 72 HIGH BLUE
 73 LOW CLOSE
 74 LOW OPEN
 75 PAUSE 100
 76
 77 ' ----- Traveling OPEN ----------------------------------------------------
 78 ' OPEN:
 79 ELSEIF (LV_CLOSE = 1) THEN
 80 LOW BLUE
 81 HIGH YELLOW
 82 LOW OPEN
 83 PULSOUT CLOSE, 7000
 84 PAUSE 100
 85
 86 ELSEIF (CLOSE_SWITCH = 1) THEN
 87 LOW BLUE
 88 HIGH YELLOW
 89 LOW OPEN
 90 PULSOUT CLOSE, 7000
 91 PAUSE 100
 92
 93 ' ----- Traveling CLOSE ---------------------------------------------------
    -
 94 ' CLOSE:
 95 ELSEIF (LV_OPEN = 1) THEN
 96 HIGH BLUE 'Turns the blue LED off
 97 LOW YELLOW 'Turns the yellow LED on
```



```
 98 PULSOUT OPEN, 7000
 99 LOW CLOSE
100 PAUSE 100
101
102 ELSEIF (OPEN_SWITCH = 1) THEN
103 HIGH BLUE 'Turns the blue LED off
104 LOW YELLOW 'Turns the yellow LED on
105 PULSOUT OPEN, 7000
106 LOW CLOSE
107 PAUSE 100
108
109 ENDIF
110 GOTO Main2
111
112 LOOP
```

Appendix C: Electric Fuel Valve (EFV) Control System

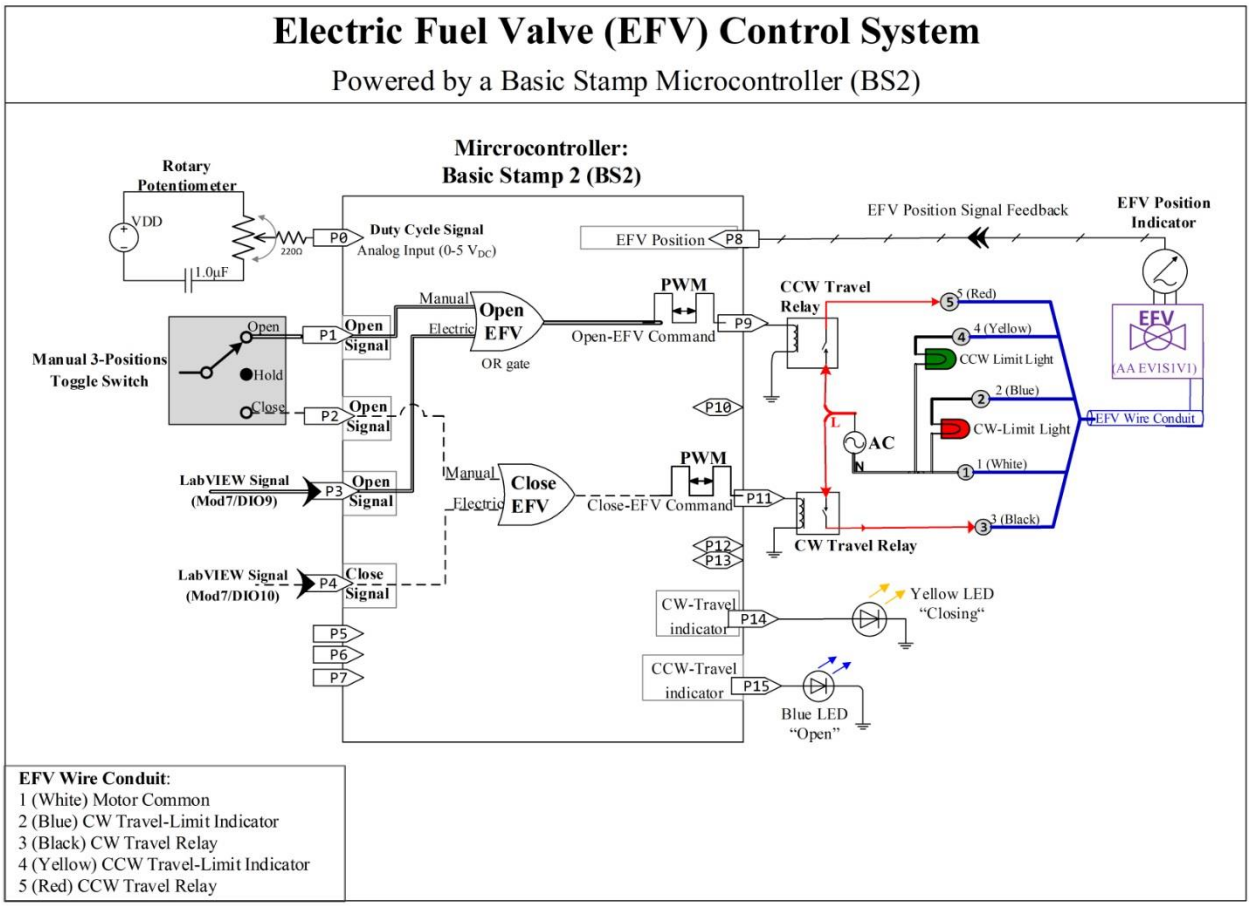

Figure 40: Schematic of the Electric Fuel Valve (EFV) Control System Used in the Syngas Rig

Appendix D: The Graphical User Interface Program Used for the EBL Flash

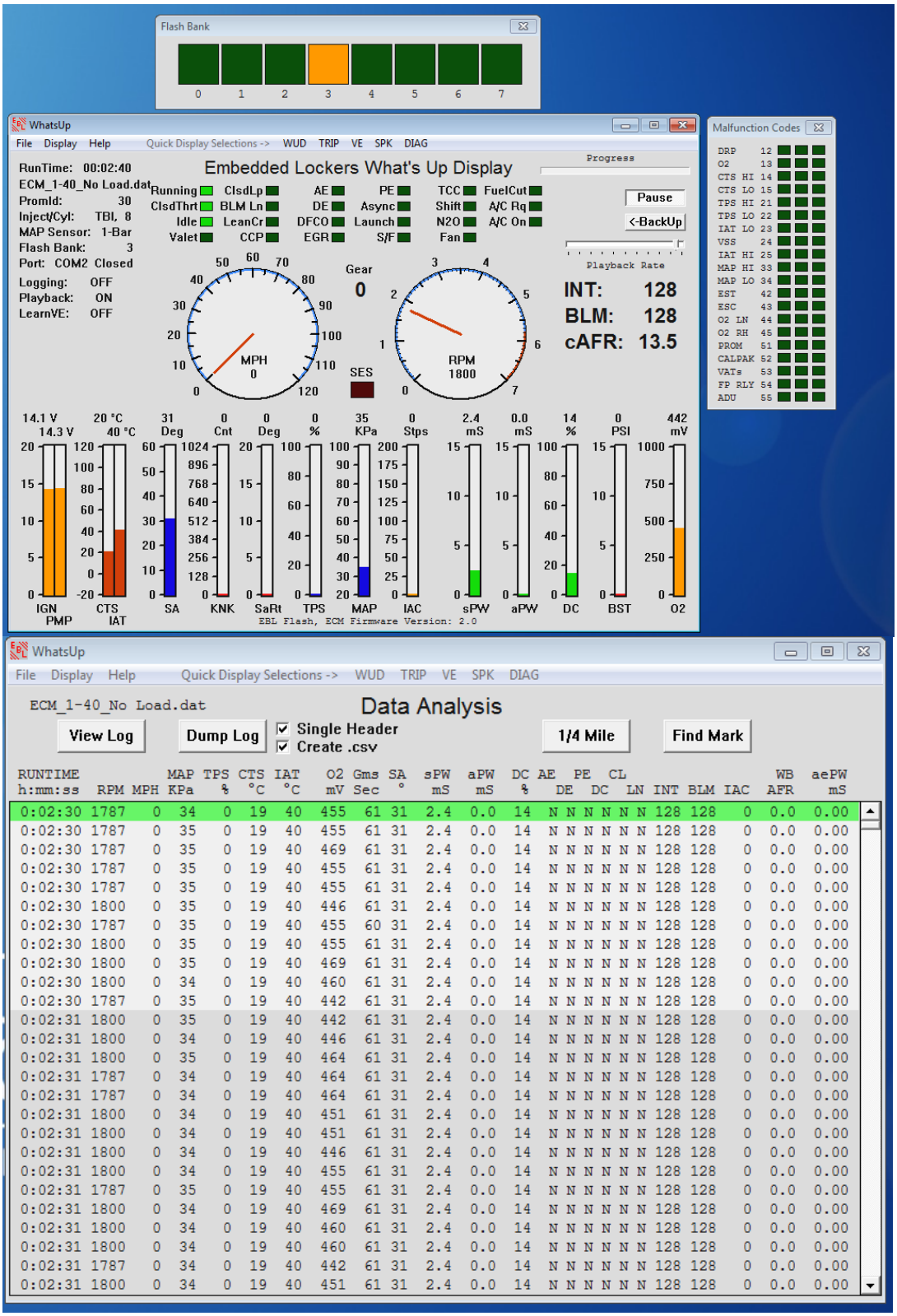

RUNTIME h:mm:ss	RPM	MPH	MAP KPa	TPS %	CTS °C	IAT °C	O2 mV	Gms Sec	SA °	sPW mS	aPW mS	DC %	AE DE	PE DC	CL LN	INT	BLM	IAC	WB AFR	aePW mS
0:02:30	1787	0	34	0	19	40	455	61	31	2.4	0.0	14	N	N	N	128	128	0	0.0	0.00
0:02:30	1787	0	35	0	19	40	455	61	31	2.4	0.0	14	N	N	N	128	128	0	0.0	0.00
0:02:30	1787	0	35	0	19	40	469	61	31	2.4	0.0	14	N	N	N	128	128	0	0.0	0.00
0:02:30	1787	0	35	0	19	40	455	61	31	2.4	0.0	14	N	N	N	128	128	0	0.0	0.00
0:02:30	1787	0	35	0	19	40	455	61	31	2.4	0.0	14	N	N	N	128	128	0	0.0	0.00
0:02:30	1800	0	35	0	19	40	446	61	31	2.4	0.0	14	N	N	N	128	128	0	0.0	0.00
0:02:30	1787	0	35	0	19	40	455	60	31	2.4	0.0	14	N	N	N	128	128	0	0.0	0.00
0:02:30	1800	0	35	0	19	40	455	61	31	2.4	0.0	14	N	N	N	128	128	0	0.0	0.00
0:02:30	1800	0	35	0	19	40	469	61	31	2.4	0.0	14	N	N	N	128	128	0	0.0	0.00
0:02:30	1800	0	34	0	19	40	460	61	31	2.4	0.0	14	N	N	N	128	128	0	0.0	0.00
0:02:30	1787	0	35	0	19	40	442	61	31	2.4	0.0	14	N	N	N	128	128	0	0.0	0.00
0:02:31	1800	0	35	0	19	40	442	61	31	2.4	0.0	14	N	N	N	128	128	0	0.0	0.00
0:02:31	1800	0	34	0	19	40	446	61	31	2.4	0.0	14	N	N	N	128	128	0	0.0	0.00
0:02:31	1800	0	35	0	19	40	464	61	31	2.4	0.0	14	N	N	N	128	128	0	0.0	0.00
0:02:31	1787	0	34	0	19	40	464	61	31	2.4	0.0	14	N	N	N	128	128	0	0.0	0.00
0:02:31	1787	0	34	0	19	40	464	61	31	2.4	0.0	14	N	N	N	128	128	0	0.0	0.00
0:02:31	1800	0	34	0	19	40	451	61	31	2.4	0.0	14	N	N	N	128	128	0	0.0	0.00
0:02:31	1800	0	34	0	19	40	451	61	31	2.4	0.0	14	N	N	N	128	128	0	0.0	0.00
0:02:31	1800	0	34	0	19	40	446	61	31	2.4	0.0	14	N	N	N	128	128	0	0.0	0.00
0:02:31	1800	0	34	0	19	40	455	61	31	2.4	0.0	14	N	N	N	128	128	0	0.0	0.00
0:02:31	1787	0	35	0	19	40	455	61	31	2.4	0.0	14	N	N	N	128	128	0	0.0	0.00
0:02:31	1800	0	34	0	19	40	469	61	31	2.4	0.0	14	N	N	N	128	128	0	0.0	0.00
0:02:31	1800	0	34	0	19	40	460	61	31	2.4	0.0	14	N	N	N	128	128	0	0.0	0.00
0:02:31	1800	0	34	0	19	40	460	61	31	2.4	0.0	14	N	N	N	128	128	0	0.0	0.00
0:02:31	1787	0	34	0	19	40	442	61	31	2.4	0.0	14	N	N	N	128	128	0	0.0	0.00
0:02:31	1800	0	34	0	19	40	451	61	31	2.4	0.0	14	N	N	N	128	128	0	0.0	0.00